OPTICAL DIAGNOSIS AND AUTO-FLUORESCENCE QUENCHING QUANTIFICATION OF BIOLOGICAL TISSUES

By

Aziz ul Rehman

A Thesis submitted to Macquarie University

for the degree of Doctor of Philosophy

Department of Physics and Astronomy

July 2018

MACQUARIE
University
SYDNEY · AUSTRALIA

Typeset in $\LaTeX\,2_{\varepsilon}$.

Statement of Originality

This work has not previously been submitted for a degree or diploma in any university. To the best of my knowledge and belief, the thesis contains no material previously published or written by another person except where due reference is made in the thesis itself.

Aziz ul Rehman

Dedication

Dedicated

To

My Beloved Father, Mother, and Wife

Acknowledgement

I humbly thanks to Almighty Allah, The Most Merciful, The Most Beneficent, whose bountiful blessings made this PhD project easy for me and taught me the knowledge that I do not know before my project. I offer my humblest thanks to the Holy Prophet Muhammad (Peace Be Upon Him) who is forever a model of guidance and knowledge for mankind.

I am much grateful to several people and organisations for their help and support during my PhD. I am thankful to Macquarie University for awarding me an International Macquarie Research Excellence Scholarships. I would like to express thanks to the National Institute of Lasers and Optronics (NILOP) Islamabad 45650 Pakistan for relieving me from the duty to avail this excellent opportunity.

I gratefully acknowledge to my supervisor Professor Ewa M. Goldys for her advice, supervision, and crucial contribution, and her guidance to complete my project on time. Her involvement with his originality has triggered and nourished my intellectual maturity that will benefit me even after this PhD. I am also thankful to my Co-supervisor, Associate Professor Andrei Zvyagin for his guidance to complete this project on time. I am thankful to The Department of Physics and Astronomy to provide me every support for PhD study. I would like to appreciate Walther Adendorff, the Manager at Macquarie Engineering and Technical Services (METS) and Greg Yates, Assistant Manager (Electronics) and Ken Yuen for helping me for the development of digital control box and power supply for Integrating sphere light source.

I would like to express my gratitude to the CNBP researchers, Dr. Guozhen, Liu, Dr Ayad, G. Anwer, and Dr Martin, E. Gosnell, from Quantitative Pty. Ltd, for their advice and encouragement throughout this journey. Special thanks to Dr Ayad, G.

Anwer for sharing his knowledge of cell-related work. I would like to pay sincere regards to team from National Institute of Lasers and Optronics (NILOP) Pakistan, Dr Muhammad Nawaz, Dr. Shamaraz Firdous, Mr Shahzad Anwer to provide me every technical, scientific and moral support.

I would like to appreciate Dr. Muhammad Iftikhar Ahmad for contributing and proof reading of articles included in the thesis. I am also very grateful to Australian Research Council (ARC) and Center for Nano Scale Bio-Photonics (CNBP) for supporting me financially throughout my research work and provided opportunity to attend several talks, speeches, conferences and retreats and technical support and time to time discussions.

I am very thankful to Dr. Muhammad Tausif Afzal Rana in pushing me for thesis writing in LATEX and his continuous support for improving its format. I am extremely thankful to Dr Keith Imrie an Honorary Associate from School of Engineering, Macquarie University and Mr. Zawar Hussain from Department of Computing, Macquarie University, for proof reading of this thesis. I also never forgot to my Room Mate (Herring Road Apartments) Mr Sham-Bin in giving me a wonderful community for study and enjoyment. To the students at Macquarie University, both past and present. Thank you for being such wonderful group of people. I would specifically like to thank Dr Biju, Cletus, Dr Sandhya Clement, Dr Saabah, B. Mahbub, Rashid Javaid, Kashif Islam, Zahra Khabeer, Abbas, Wan, Lixin, Dr Anna, Wenjie, Elizabeth, Manoj Kale, for contributed directly or indirectly in this work.

I would like to thank the Physics and Astronomy administrative team especially Lisa and Liz and for assisting me with all paperwork during the study Special thanks to Higher Degree Research especially Jane Yang for her friendly approach.

I would like to express my feelings to my wife and my cute kids Alisha Aziz, Alia Aziz, Abdul Mannan and lucky son Abdul Hannan for their support, selfless sacrifice and endless patience throughout our family journey. I must say interminable thanks to my wife for encouraging me through every difficult time.

I would like to express my deeply heart feeling to my parents (Father and Mother) and siblings for their constant prayers and support in fulfilling my dream. I sincerely, thank each one who has kept me in their prayers. Finally, I dedicate this entire work to my Father, who inspired me throughout my career with the utmost sincerity, and constant love and hard work which I cannot define in words.

List of Publications

Publications Included in This PhD Thesis

1. Aziz ul Rehman, I Ahmad, K Rehman, S Anwar, S Firdous and M Nawaz, Optical properties measurement of highly diffusive tissue phantoms for biomedical applications, Laser Physics 25, 025605 (2014) (Chapter 3, Section 3.4)

2. Aziz ul Rehman, K Rehman , S Anwar, S Firdous,and M Nawaz, Optical parameter measurement of highly diffusive tissue body phantoms with specially designed sample holder for photo diagnostic and PDT applications, Proc. of SPIE 9668, 966842-966841(2015) (Chapter 3, Section 3.6)

3. Shahzad Anwar, Shamaraz Firdous, Aziz ul Rehman and Muhammed Nawaz, Optical diagnostic of breast cancer using Raman, polarimetric and fluorescence spectroscopy, Laser Physics Letters 12, 045601 (2015) (Chapter 4, Section 4.4) (2015)

4. Aziz ul Rehman, A.G. Anwer, E.M. Goldys, Programmable LED-Based Integrating Sphere Light Source for Wide-Field Fluorescence Microscopy, Photo-diagnosis and Photodynamic Therapy 20, 201-206 (2017) (Chapter 5, Section 5.5)

5. Aziz ul Rehman, Ayad G. Anwer, and Ewa M. Goldys, Auto-Fluorescence Quenching Quantification of Free and Bound NADH In He-La Cell Line Model (Ready for submission) (Chapter 7, Section 7.4)

6. Aziz ul Rehman, Ayad G. Anwer, Martin E. Gosnell, Saabah B. Mahbub, Guozhen Liu, and Ewa M. Goldys, Fluorescence quenching of free and bound NADH in

He-La cells determined by hyperspectral imaging and unmixing of cell autofluorescence, Biomedical Optics Express 8,1488-1498 (2017) (Chapter 8, Section 8.4)

Manuscripts Ready and Submitted

1. Aziz ul Rehman and Ewa M. Goldys, Hyperspectral Fluorescence Imaging, Unmixing techniques, Biological Application: A literature Review (Ready for submission)

2. Aziz ul Rehman, Ayad G. Anwer, and Ewa M. Goldys, Auto-Fluorescence Quenching Quantification of NADH In He-La Cell Line Model (Ready for submission)

3. Aziz ul Rehman and Ewa M. Goldys, Biomedical Applications of Integrating Sphere: A literature Review (Submitted and under revision in Journal of Photodiagnosis and Photodynamic Therapy)

4. Ayad G. Anwer, Martin E. Gosnell, Aziz ul Rehman, Saabah B. Mahbub, Guozhen Liu, Kashif Islam, and Ewa M. Goldys, Impact of fixation, mounting media and cells adhesives on cells metabolic fluorophores monitored by hyperspectral imaging(Ready for Submission)

Conferences, Posters, and Presentations

1. Aziz ul Rehman, Ayad G. Anwer, Martin E. Gosnell, Saabah B. Mahbub, Guozhen Liu, Krystyna Drozdowicz-Tomsia, and Ewa M. Goldys, In-vitro fluorescence quenching of NADH by FCCP, SPIE Micro + Nano-materials, Devices and Applications 2015 conference, Sydney, Australia.

2. Aziz ul Rehmana, K Rehman , S Anwar, S Firdous,and M Nawaz , Optical parameter measurement of highly diffusive tissue body phantoms with specially designed sample holder for photo diagnostic and PDT applications, SPIE Micro + Nano-materials, Devices and Applications 2015 conference, Sydney, Australia.

3. Aziz ul Rehman, Ayad G. Anwer, Martin E. Gosnell, Saabah B. Mahbub, Guozhen Liu, and Ewa M. Goldys, Chemical quenching of NADH in He-La cells revealed

through hyperspectral imaging and unmixing of cell auto fluorescence, SPIE Bio-photonics 2016 conference, Adelaide Convention Centre, Australia.

4. Ayad G. Anwer, Martin E. Gosnell, Aziz ul Rehman,Saabah B. Mahbub, Guozhen Liu, Kashif Islam, and Ewa M. Goldys, Impact of fixation, mounting media and cells adhesives on cells metabolic fluorophores monitored by hyperspectral imaging, SPIE Bio-photonics 2016 conference, Adelaide Convention Centre, Australia.

Abstract

This thesis contributes to the development of non-invasive optical techniques based on light absorption, scattering, and fluorescence for photo-diagnostic and Photo-dynamic Therapy (PDT) of biological tissues. The first part of the thesis is devoted to the development of highly diffusive tissue body phantoms for optical parameter measurements aiming differentiation of healthy and diseased tissues. The key results are theoretical and experimental investigations of photon transport in biological tissues. The diffuse reflectance R_d and diffuse transmittance T_d of tissue body phantoms were measured using Double Integrating Sphere system. The optical parameters, absorption coefficient μ_a and reduce scattering coefficient $\acute{\mu_s}$ were calculated employing Inverse Adding-Doubling method from the measured values of diffuse reflectance R_d and diffuse transmittance T_d. This part also includes breast cancerous-tissue differentiation from normal tissue on the basis of Raman Scattering, Polarization and Confocal Fluorescence Imaging. The second part of the research is devoted to the fluorescence diagnostics of biological tissues and cells. The Programmable Integrating Sphere Light (PISAL) source was designed, built and retro-fitted in Laser Scanning Leica-DMIRB Microscope for wide-field fluorescence microscopy of BV_2 cancerous cell line. The in-vitro fluorescence chemical quenching quantification of the native fluorophore, free and bound Reduced Nicotinamide Adenine Dinucleotide (NADH) was performed. Key results of fluorescence quenching quantification confirm, that Carbonyl Cyanide-P-Trifluoro-Methoxy Phenyl Hydrazone (FCCP) selectively quenches the fluorescence of free and bound-NADH in plated and suspended He-La cells. The auto-fluorescence quenching quantification of NADH/ NAD(P)H with FCCP has validated the results of unsupervised unmixing in

He-La cell using label-free optical method of Hyperspectral Auto-Fluorescence Imaging. The combination of Hyperspectral Auto-Fluorescence Imaging and unsupervised unmixing technique will be useful for tissue diagnostic for monitoring of Photo-dynamic Therapy using PISAL light source and Single Channel Analysis(SCA).

List of Symbols

μ_a .... absorption coefficient cm^{-1}

μ_s .... scattering coefficient cm^{-1}

g .... Anisotropy

λ .... wavelength nm

R_d .... diffuse reflectance

T_c .... diffuse transmittance

T_d .... diffuse reflectance

DSMO ..... Dimethyl Sulfoxide

PBS .... Phosphate-Buffered Saline

CCCP ...... Carbonyl Cyanide m-Chloro Phenylhydrazone

NADPH .... Nicotinamide Adenine Dinucleotide Phosphate

FCCP ...... Carbonyl Cyanide-p-Trifluoro Methoxy-Phenylhydrazone

NADH ...... Nicotinamide Adenine Dinucleotide

FAD .... Flavin Adenine Dinucleotide

GAPDH ... Glyceraldehyde- 3-Phosphate Dehydrogenase

List of Acronyms

AOTF	Acoustic Optical Tunable Filter
ANN	Artificial Neural network
BIL	Band Interleaved by Line
BSQ	Band Sequential
BIP	Band Interleaved by Line
(CARS)	Coherent Anti-Raman Scattering
CASSI	Coded Aperture Snapshot Spectral Imager
(CCD)	Charged Couple Device
CGH	Computer-Generated Holograms
CMOS	Complementary Metal-Oxide-Semiconductor
CNN	Convolutional Neural Network
CT	Computed Tomography
CTIS	Computed Tomography Imaging Spectrometer
DA	Diffusion Approximation
DDMCMC	Data-Driven Markov Chain Monte Carlo
DIS	Double Integrating Sphere
EEM	Excitation Emission Matrix
EMCCD	Electron Multiplying Charged Couple Device
FOS	First-Order Scattering
FNA	Fine Needle Aspirate
FOPEN-SAR	Foliage-Penetration Synthetic Aperture-Radar
GFP	Green Fluorescent Protein
HSFI	Hyperspectral Fluorescence Imaging

HIA	Hyperspectral Image Analysis
HM-CARS	Hyperspectral Multiplex Coherent Anti-Stokes Raman Scattering
HSI	Hyperspectral Imaging
HRC	Hyper-spectral Retinal Camera
IAD	Inverse Adding Doubling
ICA	Independent Component Analysis
IMS	Image Mapping Spectrometry
KMM	Kubelka-Munk Method
LCTF	Liquid-Crystal Tunable Filters
LSM	Laser Scanning Microscope
LDA	Linear Discriminant Analyser
LSU	Linear Spectral Unmixing
MAFC	Multi-Aperture Filtered Camera
MC	Monte-Carlo Simulation
MCT	Medical Computed Tomography
MELAS	Myopathy, Encephalo Myopathy, Lactic Acidosis, Stroke-Like Syndrome
MHFI	Medical Hyperspectral Fluorescence Imaging
OWA	Ordered Weighted Averaging
PCA	Principal Component Analysis
PET	Positron Emission Tomography
PISAL	Programable Integrating Sphere Light
PLSRA	Partial Least Squares Regression Analysis
PMVEC	Pulmonary Microvascular Endothelial Cells
PPI	Pixel Purity Index
PTT	Photon-Transport Theory
QY	Quantum Yield
RPE	Retinal Pigment Epithelium
RTT	Radiative Transfer Theory
SAM	Spectral Angle Mapper
SCAS	Spectral Control and Acquisition System
SHIFT	Snapshot Hyperspectral Imaging Fourier Transform
SID	(Spectral Information Divergence)

SNR	signal to Noise Ratio
SRD	Spontaneous Raman Data
SV	Stern-Volmer
SVM	Support Vector Machine
WBCD	Wisconsin Breast Cancer Data-set

List of Figures

List of Tables

Contents

1

General Introduction and Outline

1.1 Introduction

Biological tissue is a medium in which both absorption and scattering of light occur simultaneously and is called turbid medium . So total attenuation coefficient can be expressed as a sum of absorption and scattering coefficients. When light falls on a tissue, the detected intensity across the tissue surface is less as compared to incident intensity due to simultaneous absorption and scattering. The tissue diagnosis depends upon absorption, scattering and transmission intensity of light through tissue [1]. The Lambert's-Beer's Law describes the amount of absorption of light by the tissues. It tells us that transmitted intensity of light depends upon the incident intensity, the total absorption coefficient of the tissue, and (thickness or concentration) of the tissue constituents (chromophore) and is explained in subsection (2.2.1) optical properties of tissues are discussed. Every chromophore absorb light at a specific wavelength

λ of light from the electromagnetic spectra, which play an essential role in photodiagnosis and photodynamic therapy of biological tissues. The water, oxyhaemoglobin and de-oxyhaemoglobin in soft tissues absorb light in near-infrared therapeutic window (600-1200 nm), other chromophores such as melanin, lipids also absorb a fraction in therapeutic window, and due to scattering dominance over absorption, the propagation of light becomes diffuse [2, 3]. In the figure 1.1 which is taken and modified from reference [4] shows the spectral absorption of cell all basic constituents. The

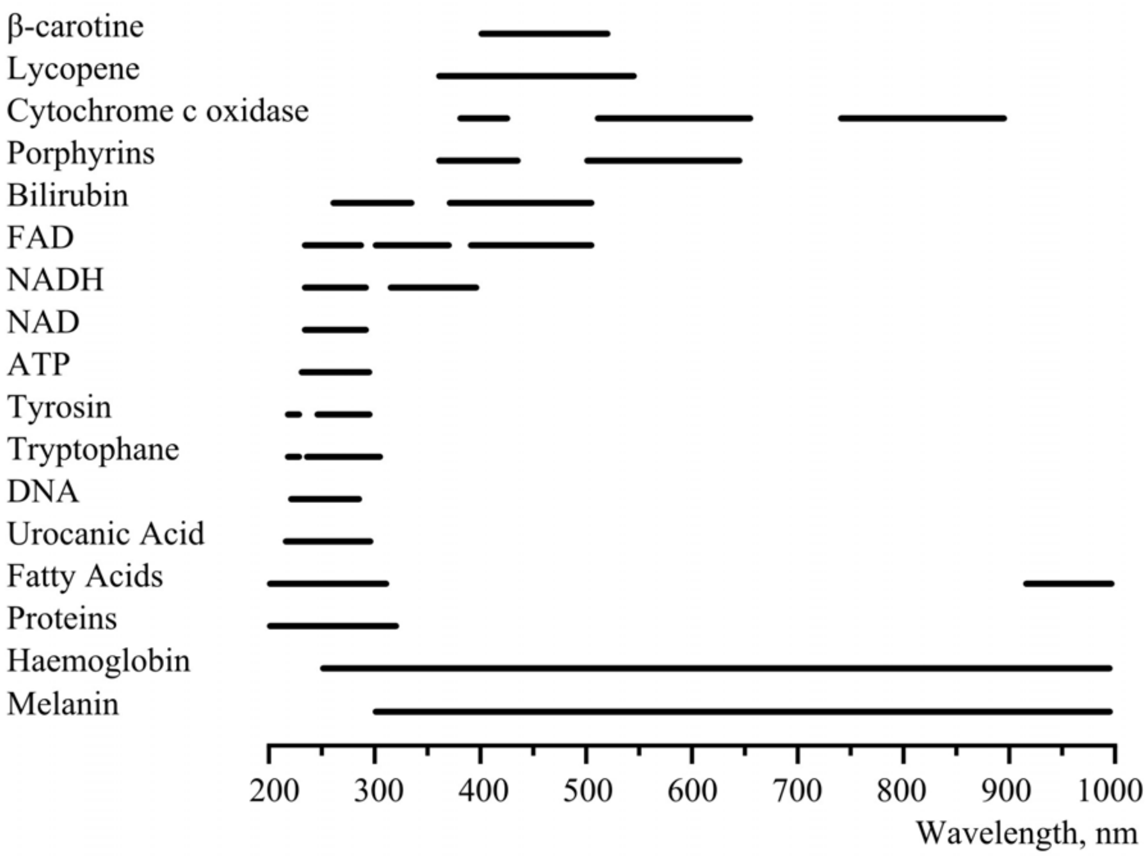

Figure 1.1: Spectral absorption of the tissue chromophores; reduced form of coenzyme NADH (Nicotinamide Adenine Dinucleotide), (FAD) Flavin Dinucleotide , (ATP) Adenosine Triphosphate, and human skin.

most exciting thing about biological tissue is that it neither follow Raleigh scattering nor Mie scattering but a third parameter called Henyey-Greenstein g function, which explains the scattering phenomenon in biological tissues [5, 6]. The values of g vary from -1 to +1 and the value -1 shows backward, +1 shows forward scattering and 0 value shows isotropic scattering. The quantitative measurement of diffuse reflectance signal R_d, however, requires accurate knowledge of tissue optical properties because of high scattering in light-tissue interaction. So, according to Radiative Transfer Theory (RTT), a turbid medium can be characterised by three parameters; absorption coefficient μ_a, scattering coefficient μ_s, and anisotropy factor g. These parameters are calculated using First-order scattering, Kubelka -Munk Theory, Monte-Carlo Simulation (MC) and Inverse Adding-Doubling (IAD) method from the measured values of diffuse reflectance R_d, diffuse transmittance T_d and collimated transmittance T_c using Integrating Sphere system. There exist natural fluorophores in the cells and tissue which give fluoresce upon excitation with a suitable wavelength λ of light. Most common fluorophores are Nicotinamide Adenine Dinucleotide (NADH), Flavin Adenine Dinucleotide (FAD) Tryptophan, and Protoporphyrin IX etc. The absorption spectrum for commonly known fluorophores is shown in figure 1.1. Wide-field fluores-

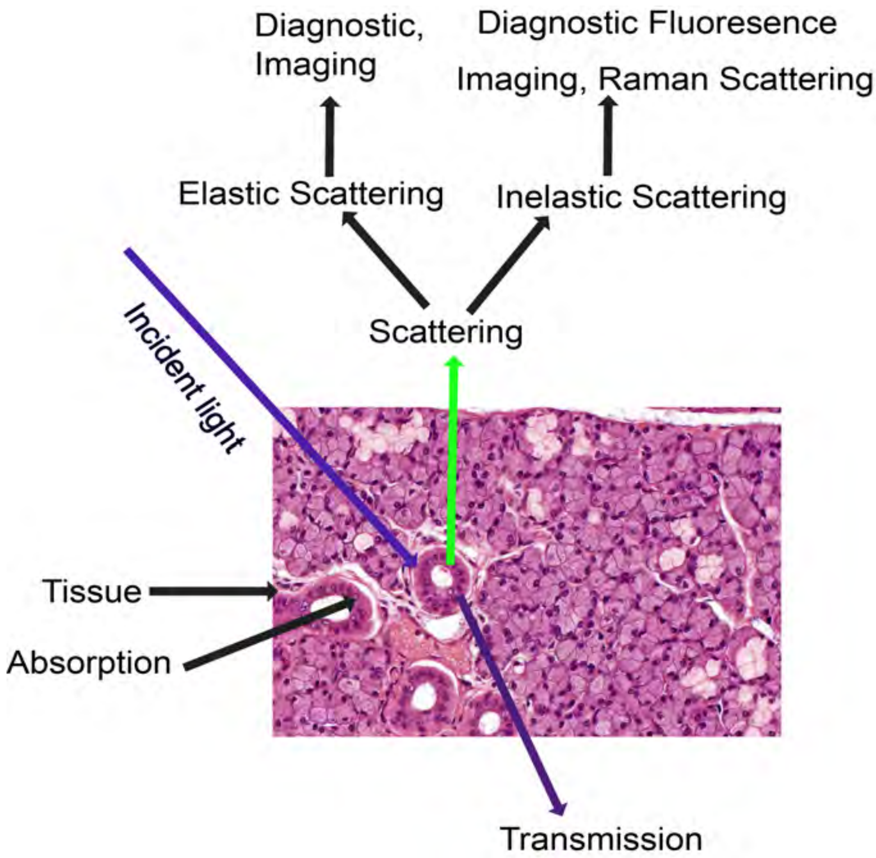

Figure 1.2: Light tissue interaction mechanism

cence microscopy, confocal microscopy, and fluorescence spectroscopy are the standard techniques used to diagnose normal and malignant cells and tissue using natural fluorophores optical properties. Since cells and tissues are turbid and thick enough, only the penetration of light inside the tissue limits the fluorescence diagnostic application.

So, natural fluorophores give auto-fluorescence upon excitation at a particular λ of light, which help to diagnose the healthy and diseased tissue using fluoroscopic techniques.The scattering of light from biological tissue is used for diagnosis of variety of diseases. There are two type of primary scattering; elastic scattering (Rayleigh and Mie) and inelastic scattering (Raman and Brillouin scattering). In case of Rayleigh scattering, the scattering particles are smaller than the wavelength λ of incident light and scattering intensity varies inversely with fourth power of λ and while in case of Mie scattering, the scattering particles are comparable to the wavelength λ of incident light and scattering intensity shows weak dependence on wavelength of light λ. Figure 1.2 shows possible type of interactions in biological tissues. It shows that every type of interaction may be elastic or inelastic scattering, absorption and transmission all of them provides useful information about biological tissue.

1.2 Motivation

The uncontrollable growth of abnormal cells or cluster is the primary cause of cancer. If these abnormal cells are uncontained, it can cause death. According to Atlanta report submitted by the statistical study group of researchers, that in USA cancer is the second cause of death among children (0-14) years age and up to December 2016 around 12% of children died due to cancer [7]. The data of female breast cancer based on survival, mortality, incidence and screening statistics in the US described that approximately 17.37% deaths occurred among US women in 2015 due to breast cancer [8]. The American Cancer Society and the National Cancer Institute around 3,560,570 breast cancer and 757,190 uterine corpus cases reported in females and more than 20 million people will survive with cancer history in January 1, 2026 [9]. Nowadays breast cancer diagnosis include microscopic analysis or affected part biopsy or x-rays based mammography. These methods are painful and uncomfortable. So, there is a need of painless optical methods to diagnose the cancer early as possible to increase the survival rate. Our goal is to diagnose the breast and cervical cancer using optical methods. These optical methods make use of diffuse reflectance R_d, diffuse transmittance T_d, Raman Scattering and fluorescence quenching from the tissues or cells to differentiate healthy and diseased cells and tissues.

1.3 Aims and Objective

The aims of this dissertation are as follows

- To fabricate a unique sample holder to measure for diffuse reflectance R_d and diffuse transmittance T_d highly diffusive tissue body phantoms Intralipid and Indian-ink in an Integrating Sphere System. The optical parameters (absorption coefficients μ_a and reduce scattering coefficient $\acute{\mu_s}$=μ_s(1-g)) of tissue mimic phantoms made from concentrated 20% Intralipid and 1% Indian-ink dilutions by applying Inverse Adding-Doubling (IAD) method.
- To use optical techniques to differentiate healthy and cancerous breast tissues.
- To make a high uniform profile programmable Integrating sphere light source for fluorescence imaging of breast cancer BV_2 cells. The PISAL source in the future can be used for wide-field fluorescence imaging of many chromophores like Tryptophan, DNA, Proteins, and many other fluoropheres in a cell using spatial uniform light source.
- To perform auto-fluorescence quenching quantification of free and bound NADH in biological tissues.
- The hyper-spectral imaging and unmixing of the cell auto-fluorescence for validation of unsupervised unmixing techniques.

1.4 Thesis Outline

This thesis is compiled in the form of nine chapters as follows

- Chapter 1 is a general introduction and outline which is an introduction of light-matter interaction and it highlights the electromagnetic spectral region use for optical photo-diagnostic techniques for biological tissues. The natural fluorophores NADH and FAD of the cell which give auto-fluoresce upon excitation with the suitable wavelength λ of light and have a critical role in cellular metabolism.
- Chapter 2 provides the detail literature survey of the optical parameters measurement of absorption coefficient μ_a, scattering coefficient μ_s, and anisotropy g

using Double Integrating Sphere (DIS) system. The photon transport equation and its solution using First-Order scattering, Kubelka -Munk Theory, Monte-Carlo simulation MC, and Inverse Adding-Doubling IAD Method. The current literature for tissue body phantoms (Indian ink and Intralipid), breast cancerous tissue differentiation based on optical parameters is also the part of this chapter.

- Chapter 3 consists of two published articles along with some theoretical background of light absorption and emission in tissues and motivation for the study. The first publication is a Laser Physics Journal article under the title Optical Properties Measurement of Highly Diffusive Tissue Phantoms for Biomedical Applications in Laser Physics 25, 025605 (2014), which gives change in optical parameters absorption coefficient μ_a and scattering coefficient μ_s upon percentage change of tissue body phantoms concentration. The second publication is the conference publication under the title Optical Parameter Measurement of Highly Diffusive Tissue Body Phantoms With Specially Designed Sample Holder for Photo Diagnostic and PDT ApplicationsProc. of SPIE 9668, 966842-966841(2015), which gives an idea of the specially designed sample holder for diffuse reflectance R_d and diffuse transmittance T_d measurement for high diffusive tissue body phantoms Intralipid and Indian-ink. The repeatability curve of optical parameters for 20% Intralipid is also part of this publication. The third part of the chapter provides the supplementary material for detailed experimental analysis.

- Chapter 4 consist s of the third publication under the title, Optical Diagnostic of Breast Cancer Using Raman, Polarimetric and Fluorescence Spectroscopy, in which we have differentiated the normal and malignant breast human tissue using optical techniques and a paper published in Laser Physics Letters 12, 045601 (2015).

- Chapter 5 consists of fourth publication under the title, Programmable LED-Based Integrating Sphere Light Source for Wide-Field Fluorescence Microscopy, in a journal of Photo-diagnosis and Photodynamic Therapy 20 201-206 (2017). In this article, we have indigenously developed and retrofitted a uniform profile light source consisting of nine LEDs in a Laser Scanning DMIRB Leica Confocal

Microscope for Fluorescence Microscopy of BV_2 cell line.

- Chapter 6 consists of a literature review of Hyperspectral Fluorescence Imaging (HSFI) system, its four types, Spatial-scanning, Spectral-scanning, Snapshot-scanning and Spatio-Spectral scanning. It also provides detail about hyperspectral image analysis methods, pre-processing methods, and feature extraction and selection methods and data classification techniques. The coupling of Hyperspectral Imaging Systems with optical modalities like Raman scattering, fundus cameras, confocal and conventional microscopes is also part of this chapter. The process of fusion of unsupervised-unmixing techniques with other classification methods, e.g., Support Vector Machine with Artificial Neural Network and Snapshot Hyperspectral Imaging with Vortex Analysis techniques. Finally, recent application of Hyper-Spectral Imaging System HSFI for cellular differentiation of a variety of cancers has been discussed.

- Chapter 7 consist of fifth manuscript, it shows the fundamental chemical reaction between Reduced Nicotinamide Adenine Dinucleotide (NADH) with Carbonyl Cyanide-p-Trifluoro Methoxy Phenylhydrazone (FCCP). In-vitro fluorescence quenching quantification of NADH versus FCCP in a wide range of concentration (0.01-5.0) μM for He-La cell line model are part of this manuscript. We plotted the Stern-Volmer Plots using peak fluorescence intensity values and presented the fluorescence quenching comparison of In-vitro NADH solution, suspended and plated cells. We studied the Excitation Emission Matrix EEM of NADH and FCCP quenching fluorescence. The manuscript ready for submission under the title Auto-Fluorescence Quenching Quantification of Free and Bound NADH In He-La Cell Line Model.

- Chapter 8 consists of sixth publication under the title, Fluorescence Quenching of Free and Bound NADH In He-La Cells Determined by Hyperspectral Imaging and Unmixing of Cell Auto-Fluorescence. The work beyond the chemical fluorescence quenching quantification and hyperspectral unmixing validation are part of this chapter. We did hyperspectral imaging of He-La cells at all the FCCP concentrations (50-1000) μM using 18 channel hyperspectral imaging system. The whole data has been unmixed using PCA-analysis. It validates that hyperspectral fluorescence imaging can be used to unmix NADH and FAD.

- Chapter 9 concludes the entire thesis work. It also gives the future direction, that how we can use optical techniques to monitor Photodynamic TherapyPDT.

2

Integrating Sphere, Its Biological Application (Literature Review Part-I)

2.1 Summery of the Literature Review

A literature review of Double Integrating Sphere (DIS) system to measure the optical parameters absorption coefficients μ_a and reduce scattering coefficients $\acute{\mu_s}$ of biological tissue is presented. We studied the photon transport equation and its solution using First-order scattering, Kubelka-Munk method, Monte-Carlo simulation and Inverse Adding-Doubling (IAD) method. We presented the up-to-date literature for the use of Indian ink and Intralipid as tissue body phantoms for medical applications. We also discussed normal and malignant breast-tissue differentiation on the basis of optical parameters.

2.2 Introduction

An Integrating Sphere is a hollow spherical cavity which conserves power but destroys the spatial information of the source. Its interior is coated with a diffuse white reflective layer and there are two small holes across the hollow spherical cavity, named as entrance and exit ports. Due to multiple reflections of the light radiation inside the spherical cavity, the light flux distribute uniformly at every point on the surface. The light produced by a source inside the sphere can be measured on a single point on the surface of the Integrating Sphere and has many application in science and technology [10]. For the theoretical assumptions to be valid, the area of all ports of the Integrating Sphere should be at most 5% of the sphere surface area. Applications of Integrating Sphere includes; the measurement of total power of a laser beam without direction, position and shape dependency [11], absolute quantum yield measurement [12–14], diffuse reflection and transmission measurement [15], construction of uniform light sources [16–19] and the optical parameter measurements of the biological tissues [20].

2.2.1 Optical Properties Measurements

In optical measurements, the intensity is a measurable quantity. Once light interacts with biological tissues, the total intensity of light is reduced, so measurements of the transmitted, reflected, and scattered intensities provide insight into the tissue structure. Photons absorbed by the tissue cannot be detected. Therefore, the absorbed intensity is calculated by subtracting the transmitted, reflected, and scattered intensities from the incident intensity. The experimental arrangement to measure the total attenuation coefficient μ_t is shown in figure 2.1 (a). There are two beams; one is the reference beam I_o and the second is attenuated beam I after interaction with the tissue or sample. The attenuation coefficient can be calculated using the Lambert-Beer law

$$I = I_o exp(-\mu_t D) \tag{2.1}$$

where D is the sample thickness. So, there is an exponential decay of the light intensity as it passes through the turbid media. Most of the biological tissues produce forward scattering after interaction with light. The anisotropy factor g, which gives the angular dependence of scattering, can be measured experimentally by fixing the sample and rotating the detector on 360 degree angle. The experimental arrangement to measure anisotropy g, is shown in the figure 2.1 (b). It can be measured by the following formula [21].

$$g = \frac{\sum_i (\cos\theta_i) I_i}{\sum I_i} \tag{2.2}$$

Here I is the measured light intensity at each scattering angle θ. It has a value of +1 for forward scattering, -1 for backward scattering and 0 for isotropic medium. For most of the biological tissues, its value lies in the range of 0.69 $\leq$ g $\leq$0.99 [22]. Now, we will investigate the measurement of diffuse reflectance R_d, diffuse transmittance T_d and collimated transmittance T_c. Single or double Integrating Spheres can be used to measure these quantities. Single Integrating Sphere experiment to measure R_d, T_d and T_c is shown in figure 2.1 (c, d) [23]. Since, biological tissue can change the optical properties during measurement, so in such cases, double Integrating Sphere experimental set up is the best choice and it is shown in figure 2.1 (e). The Photon Transport Theory (PTT) in biological tissues, radiance equation and its analytical and numerical solutions will be the subjects of the next section.

2.3 Photon Transport Theory, Solution and Applications

Light tissue interaction, at the single photon level, has been governed analytically by the photon transport theory. Specifically, the transport of each photon through the turbid medium (i.e., offering both absorption and scattering of light such as biological samples) is followed and recorded. This theory has been used extensively in understanding the underlying mechanism of the light-tissue interactions. Importantly, the analytical results of photon transport theory reasonably agree with the experimental evidence in many cases.The photon transport theory is based on the radiative transport equation, which describes the spatial variations of the photon beam radiance, as follows [24, 25].

$$\frac{dJ(r,s)}{ds} = -\mu_t J(r,s) + \frac{\alpha_s}{4\pi}\int_{4\pi} J(r,\acute{s})p(s,\acute{s})d\acute{\omega} \tag{2.3}$$

where J(r,s) is the radiance (W/cm^2 Sr^{-1}) and p(s,$\acute{s}$) is the phase function of the photon beam scattered from original direction $\acute{s}$ into s, ds is the differential path length, and $d\acute{\omega}$ is the solid angle in the direction s. The normalized value of p(s,$\acute{s}$) is called the anisotropy function g, given as

$$g = \int_{-1}^{1} \cos\theta.p(\cos\theta).d\cos\theta \tag{2.4}$$

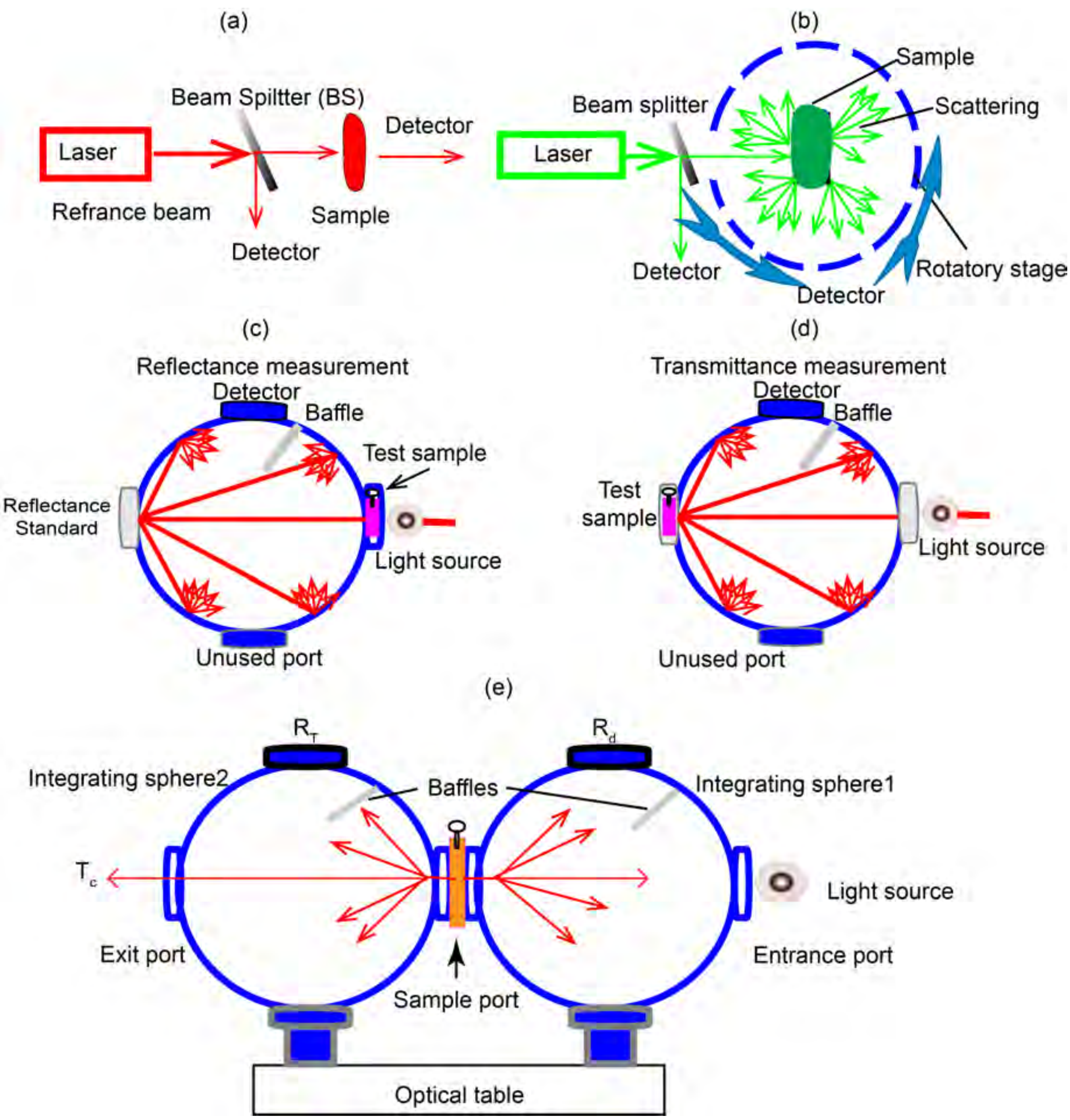

Figure 2.1: Experimental setup to measure optical properties of biological tissues (a) total attenuation coefficient μ_t using Lambert-Beer law (b) Goniometric setup to measure anisotropy g of biological tissue; sample or detector can rotate all around the sample to measure data from 360 degrees (c) single integrating sphere setup to measure diffuse reflectance R_d of any sample (d) single integrating sphere setup to measure diffuse transmittance T_d of any sample (e) The Double Integrating Sphere System to measure the optical properties diffuse reflectance R_d, diffuse transmittance T_d and collimated transmittance T_c of tissue and cells simultaneously.

g is a bounded function [-1, 0, 1] representing the backward, isotropic and forward scattering, respectively. In equation 2.3 μ_t is total attenuation coefficient which is the sum of the absorption coefficients μ_a and scattering coefficients μ_s can be written as follows

$$\mu_t = \mu_a + \mu_s \tag{2.5}$$

As equation 2.3 has more than one variables so it cannot be solved analytically it can be solved numerically by considering certain assumptions. The relationship between intensity and radiance is given by the equation

$$I(r,s) = \int_{4\pi} J(r,s)d\omega \tag{2.6}$$

The solution of equation (2.3) gives optical parameters (μ_a, μ_s, and g . The radiance J is the combination of coherent and diffuse parts given by

$$J = J_c + J_D \tag{2.7}$$

so to calculate the radiance, solutions of both coherent and diffusive part of the radiance are necessary. Coherent radiant equation and its solution can be written as

$$\frac{dJ_c(r,s)}{ds} = -\alpha_t \tag{2.8}$$

$$J_c = I_o\delta(\omega - \acute{\omega})exp^{-d} \tag{2.9}$$

Here I_o is the incident intensity, d optical depth (dimensionless quantity) and $\delta(\omega - \acute{\omega})$ is the solid angle change. We can write a relation between dimensionless parameter d optical depth and physical path length s. The physical path length s and the reduced coefficient $\acute{\mu_s}$ can be written by the equations as

$$d = \alpha_t s \tag{2.10}$$

$$\acute{\mu_s} = \mu_s(1-g) \tag{2.11}$$

From the measured intensity (radiance) of the light beam, the optical properties are calculated using various analytical models; these models include the First-Order Scattering (FOS) [26, 27] , Kubelka-Munk Method (KMM) [28] , Diffusion Approximation (DA), Monte-Carlo Simulations (MCS) [29], and Inverse Adding-Doubling (IAD) Method.

2.3.1 First-order Scattering

The basic assumption of the first order scattering method is that the diffuse intensity is much less than the coherent intensity during light tissue interaction such that

$$I_c + I_d \cong I_c \tag{2.12}$$

This assumption reduces the radiative transport equation (and its solution) to the simple case of Beer Lambert law, where the total attenuation coefficient μ_t is given by the following equation

$$\mu_t = \mu_a + \mu_s \frac{1}{D} \ln(\frac{I_o}{I}) \tag{2.13}$$

The first-order solution is applicable to problems where the incident beam is in the form of plane wave and the optical depth d« 1. Such scenarios are routinely found in optical diagnosis where the optical depth is considerably small. On the contrary, if the assumption that the optical depth d« 1 does not hold, the first order solution may not lead to accurate results. Previously, the method of first order scattering has been used in many biomedical applications of light. For instance, photons interaction with spherical particles in turbid media has been investigated, using first order diffuse scattering, towards facilitating the imaging applications in the presence of multiple scattering centers. The results showed the agreement of analytic solution with experimental data [30]. Moreover, the photon fluence distributions in biological tissues have been studied with the help of mathematical model, based on radiative transport equation in turbid media [31]. Jun Li et al. measured laser speckle pattern formation after transmission of light from ultrasonic modulation column to acquire two-dimensional images of thick (∼25 mm) biological-tissue with a low-power laser [32]. Further, it was demonstrated that "Born Approximation" fails in case of strong perturbations; however, the iterative algorithm can still yield accurate results in scattering media for higher order approximations [33] .

2.3.2 Kubelka-Munk Method

Kubelka and Munk (1931) proposed two flux theories having J_1 & J_2 radiances, i.e. forward and backward flux instead of first order scattering in which $J_c = 0$. Due to two fluxes, there are two Kubelka-Munk absorption and scattering coefficients i.e., A

$_{KM}$ and S_{KM}. They can be calculated from the measured values of diffuse reflectance R_d, diffuse transmittance T_d and unscattered T_c. If we know the values of R_d, T_d and T_c then A_{KM} and S_{KM} can be found using the following equations [34]

$$\acute{x} = \frac{1 + (R_d)^2 - (T_d)^2}{2R_d} \tag{2.14}$$

,

$$\acute{y} = \sqrt{x^2 \acute{-} 1} \tag{2.15}$$

$$S_{KM} = \frac{1}{\acute{y}t} \ln(\frac{1 - (\acute{x} - \acute{y}R_d}{T_d}) \tag{2.16}$$

$$A_{KM} = S_{KM}(\acute{x} - 1) \tag{2.17}$$

$$A_{KM} = 2\mu_a \tag{2.18}$$

$$S_{KM} = 3\mu_s(1 - g) - \mu_a \tag{2.19}$$

The K-M method may be iterative and non-iterative method. In case of non-iterative K-M method A_{KM} and S_{KM} can be obtained by putting the values of R_d and T_d in equations 2.14-2.19 and an anisotropy g can be measured goniometrically [21]. Hua et al. applied K-M two-flux model to calculate the μ_t of human normal small-intestine tissue and explored that optical parameters variation with wavelength, can be used for tissue diagnostics [35]. Yang et al. provided a revised Kubelka-Munk theory-I, using a statistical approach, and considering the effect of scattering on the optical path length in turbid media. According to their results, A_{KM} and S_{KM} depend non-linearly on both μ_a and μ_s and experimental findings on dye paper cannot be explained using ordinary K-M approach so they revised K-M theory and explained the results on dye and paper numerically. This new approach can be used to solve many complicated problems including (dental resin composite material [36], fluorescent turbid media[37], 3-D radiative transfer [38], low-scattering sample calibrations [39], decoupling of scattering and absorption in turbid materials [40], and scattering or absorption of light in non-homogeneous materials [41]. Yang et al. also presented a revised K-M theory II in which they provided unified framework for homogeneous and inhomogeneous optical media by studying ink penetration depth for linear and exponential homogeneous model. They studied this framework for A_{KM} and S_{KM} as well as flux in and out for vertical light streams [42]. Yang et al. proposed a revised general K-M theory III of light propagation in turbid media. The relation between K-M theory and RTT equation, valid only for scattering dominating media. Arindam, R. et al. measured R_d and T_d values for tissue phantoms and their results indicate that S_{KM} depends only on $\acute{\mu_s}$ while A_{KM} depends on μ_a and $\acute{\mu_s}$ [43]. Rehman et al. applied KM- Model (KMM) to calculate the optical parameters of He-La cell suspension by measuring measured R_d, T_d and T_c by placing the sample sandwich between two integrating spheres [44].

2.3.3 Diffusion Approximation DA

When scattering become dominant on absorption like in tissues, the diffusion radiance can be expanded as

$$J_d = \frac{1}{4\pi}(I_d + 3\mathbf{F}_d\mathbf{S} + ...) \tag{2.20}$$

I_d is the diffuse intensity, and F_d is the vector flux can be expressed by the following equation.

$$\mathbf{F}_d(r) = \int_{4\pi} J_d(\mathbf{r}, \mathbf{s})\mathbf{s}d\omega \tag{2.21}$$

Thus total intensity in case of diffusion approximation can be written as

$$I = I_c + I_d = Aexp^{\alpha_t z} + Bexp^{\alpha_{eff} z} \tag{2.22}$$

Here z is the path length, the solution of equation 2.22 gives the relation for optical parameters (α, α_s, and g) as

$$\alpha_{eff} = \sqrt{3\alpha\acute{\alpha_t}} \tag{2.23}$$

Diffusion approximation applications include (measurement of optical properties of thin samples [45], light scattering from red blood cells [46], human tissue diffuse reflectance measurement with CCD [47], diffuse optical tomography [48] and the accuracy improvement of the scattering model in highly absorbing media [49]. The diffusion approximation technique is used to study the fractal mechanism of light scattering tissue optical biopsy [50], early detection of breast cancer using novel estrogen conjugate fluorescent dyes [51], and analysis of optical tomography with non-scattering regions [52]. Keith, D. Paulsen et al. developed a finite element algorithm for the analysis of frequency domain optical data based on a diffusion approximation. They did the computation for a tissue-like phantom and simulated the boundary condition of multi-detector, multi-source measurement and excitation strategy to elucidate μ_a and μ_s [53].

Daniele, C. et al. reported an analysis of the time-dependent DA, getting solutions for the slab geometry and a semi-infinite diffusing medium. They concluded that in case of transmittance, the effect of the refractive index mismatch cannot be ignored in obtaining an expression of the diffusion absorption coefficient (α) [54]. James, L. Karagiannes et al. measured the optical parameters of animal and plant tissues over a wide spectral range and found that the data match well with known fluoropheres in the cells [55]. Serge Grabtchak et al used the diffusion approximation to simulate experimental interstitial radiance data obtained for homogenous 1% Intralipid-liquid phantoms and observed the optical absorption and scattering properties in the range of λ=650-900 nm [56].

2.3.4 Monte Carlo Simulations (MC)

Monte-Carlo (MC) simulation solves equation 2.3 numerically in which N photons are generated randomly using computer random generator. The photons follow the optical path through a turbid medium during absorption and scattering events and the distance between two collisions is noted through computer algorithms. If scattering occurs, a new direction is adopted by the photon with new probity phase function and a random number. As the photons propagate through the turbid medium, their weight reduces continuously until reaches a threshold value where they can escape from the given volume and is detected [57, 58]. Marquet Pierre et al. modeled light distribution in turbid media based on a single MC approach, which can save time just avoiding repetition of certain parameters. It uses two probability distribution radiance functions, one depends on geometry and anisotropy while the other depends on optical coefficients [59]. Oliveira, L. et al. estimated the evolutionary states of rabbit muscle immersed in an osmotic solution using MC simulation. They examined the optical transparency by reducing the value of absorption coefficient simultaneously and independently [60]. Chu, S. et al. made the analysis of the fluorescence spectra of the colon and cervical tissues at different dysplasia grades using MC simulation. The simulation results matched well with the in-vivo optical parameter μ_a, μ_s [61]. Jagajothi, G. et al. determined the optical parameters μ_a, μ_s and g of the skin lesion with MC simulation and made the tissue-body phantom with white paraffin wax mixed with colour pigments in multiple proportions [62]. Alwin, K. described a fast, accurate method for determination of the optical properties of an infinite and semi-infinite turbid media proved that the single MC method can be used to extract optical parameters μ_a, μ_s with less than 1% and 2% errors, respectively [63]. Chatigny, S. et al. developed a Hybrid Monte-Carlo (HMC) technique to model time-domain transillumination measurements with small-area detectors to reduce the time calculations, but it produces spikes in the temporal signals [64]. Lin, L. et al. developed condensed MC methods to predict the spatially resolved reflectance from a turbid medium with arbitrary μ_a, μ_s and their direct scaling of the radial reflectance of baseline simulation is more efficient and faster than conventional scaling methods [65]. Nunu, R. et al. presented the concept of parallel MC simulation of light photon transmitting through a heterogeneous tissue medium. A combination of triangle meshes can make this type of heterogeneous surface. The MC simulation is implemented on graphics processing units (GPU) [66].

2.3.5 Inverse Adding Doubling Method

The Inverse adding-doubling (IAD) method is a numerical approach introduced by Prahl et al. in 1999 to solve transport equation 2.3. This method takes the values of the optical parameters and match the corresponding values of R_d and T_d layer by layer continuously and make the layer thickness double to estimate the double layer parameters for a thin slab, which is also implementable for dissimilar slabs of tissues also [67, 68]. John, W. Pickering et al. devolved a system which can calculate the optical parameters of tissue μ_a, μ_s and g simultaneously. Scott, A. Prahl 1999 explained it more and provided the code to the general public to calculate the optical parameters μ_a, μ_s and g from the measured values of R_d, T_d and T_c using single or double Integrating sphere. It takes R_d, T_d and T_c, ports diameters, Integrating sphere diameter, number of ports, the refractive index of the sample as input and gives optical parameters μ_a, μ_s, and g as output [69]. The Henyey-Greenstein phase function which gives the anisotropy can be calculated theatrically and experimentally using equations 2.4 and 2.2 respectively [70]. The inverse adding-doubling method is used in many photo-diagnostic and photodynamic monitoring applications. A diagnosis study is based on measured values of optical parameters, because healthy and diseased tissue vary in optical parameters. Inverse Monte-Carlo (IMC) simulation in combination with IAD algorithm can be used with real-time Photodynamic Therapy (PDT) for dosimetry calculations. Morales, C. et al. iteratively solved the radiative transport equation using genetic algorithms and Monte-Carlo Multi-Layer (GA-MCML). It is robust search technique that avoids the local minima for the optimization problem on a set of phantoms using a single integrating sphere system [71]. Xiaoyan, Ma. et al. measured optical parameters of mammalian tissue phantoms based on the integrating sphere and spatial filtering techniques from the UV-NIR region. The corresponding procedures for inverse determination of optical parameters from the experimental data have been established [72]. Dhiraj, K. Sardar et al. used an integrating-sphere system and IAD method to differentiate normal and diseased skin tissues. They also calculated the optical parameters for human retinal tissues using the IAD method [21, 73, 73–75]. Andre, R. et al. used an integrating-sphere and IMC simulations to measure optical parameters (μ_a, μ_s and g of human blood at λ=633 nm [76]. Optical parameters are the measurement of state of a tissue, so the real time state of a tissue is possible during treatment. To account these variations, Katsunori, I. et al. measured optical parameters of tissue in the range of λ=350-1000 nm, using a tunable Er:YAG laser [77] after the PDT treatment. Honda N. et al. investigated the effects of PDT on the optical parameter μ_a, $\acute{\mu_s}$ of lung carcinoma employing IAD from the measured values of R_d , T_d using integrating sphere for λ=350-1000 nm. They found that coagulation and ablation phenomenon results in increase of $\acute{\mu_s}$ and decrease of μ_a values while in PDT both μ_a, $\acute{\mu_s}$ are increased [78]. Bashkatov, A. N. et al. measured the optical parameters μ_a and μ_s of the human skin, subcutaneous adipose tissue and human mucosa with Integrating-Sphere System using IAD method from λ=400-2000 nm [79]. Baba, Justin S. et al. and Allegood, MS. et al. measured μ_a, μ_s using the g value for a specified λ. They used an Integrating-sphere with a collimated white-light source for diffuse reflectance and transmittance measurements. Their Lab-View program takes input from IAD method to produce optical parameters of tissue body phantoms and they called this technique as Hybrid Inverse-Adding Method (HIAD) [80]. Wei, Huajiang et al. checked normal human pulmonary artery tissue spectral dependence of the optical parameters μ_a, $\acute{\mu_s}$ with IAD method. Their results indicate that μ_a and the penetration depth (l) show direct relation, while $\acute{\mu_s}$ and backscattered reflectance show an inverse relation with λ [81].

2.4 Tissue Body Phantoms

To find the optical properties of biological tissue there is a need for such materials which have the tissue-like optical properties. In the literature, Intralipid and Indian ink are used as tissue body phantoms. When light interacts with the tissue, it is either scattered or absorbed. Ideally, if tissue body phantom absorbs light completely and scattering is negligible, then its optical properties resembles Indian-ink, and if tissue body phantom scatters light completely and absorption is negligible, then its optical properties resembles with Intralipid. Different groups of scientist used uniform micro-spheres (Duke Scientific Corporation), 10-20% Intralipid and 1.0% Indian-ink for the Integrating sphere calibration to use it for biological applications. To observe μ_s variation with Intralipid concentration at a specific λ, the Indian-ink % value should be fixed at some arbitrary value, and R_d, T_d should be measured using a series of Intralipid concentrations in an Integrating-sphere system. A summary of tissue body phantom optical parameters are shown in table 2.1, 2.2 and 2.3. Conversely, to observe μ_a variation with Indian-ink concentrations at a specific λ, Intralipid concentration should be fixed at some arbitrary value and R_d, T_d should be measured using a series of Indian-ink concentrations in an integrating sphere system [82–84].

Krainov, A.D. et al. analysed the optical parameters of Lipofundin and Indian-ink to create tissue mimic phantoms at the wavelength range of 700-1100 nm. The optical parameter measurement analysis results indicate that for bowel tissue, the Lipofundin and Indian-ink should be 2.9% and 0.018% while for muscles its value is 0.89% and 0.024%, respectively [85]. Driver, I. et al. studied fat emulsions (tissue phantom materials) and found that μ_{eff} and l (penetration depth) of an Intralipid suspension, are not directly proportional to the concentration because water absorption plays an important role [86]. Alida, Mazzoli et al. made semi- indigenous tissue body phantoms by adding scattering and absorbing particles to a Poly Vinyl Alcohol) (PVA) gel having the degree of hydrolysis greater than 99% to which particles were added, and liquid Indian-ink used to simulate melanin (pigment cells) [87, 88]. Ruiqi, L. at al. made a Poly-dimethyl-siloxane (PDMS) based liver phantom by using Al_2O_3 powder 99.99% as primary scatterer (0.5-1) μm and Inframat and black-ink to mimic absorption over in the range of λ=700-1000 nm. Their calculated values (μ_a, $\acute{\mu_s}$) for tissue body phantoms were (3.0-0.5) cm^{-1} and (4.0-8.0) cm^{-1} at λ=200-1100 nm, respectively [89]. Idit, F. et al found an isobaric point using new tissues-like phantoms made of polyvinyl chloride-plastisol (PVCP), silicone elastomer-PDMS and PDMS-glycerol mixture [90].

2.4.1 Breast Tissue Differentiation

Breast cancer is a very common disease in women. Most commonly used effective screening tool against breast cancer was X-Ray mammography but with 50% false negative results [116]. The researchers started research on breast-cancer diagnostics using optical techniques which include; time-independent and dependent measurements of scattered light [117–120]. The table 2.4 and 2.5 show a complete list of breast-tissue diagnosis results using different optical techniques along with the commonly used method of optical parameters extraction programs, like IAD, IMC and Diffusion-approximation.

2.5 Conclusion

Double-Integrating Sphere along with theoretical models (First order scattering, K-M Theory, Monte-Carlo Simulation, and Inverse Adding Doubling(IAD) Method) will always remain a compulsory instrument to measure the optical parameters absorption coefficients (μ_a) and reduced scattering coefficients ($\acute{\mu_s}$) of biological tissues accurately and precisely. These optical parameters are very helpful in PDT treatment planning.

Table 2.1: A summery of the Optical parameters of the tissue body phantoms, by different research groups

Tissue Body Phantom	μ_a cm^{-1}	$\acute{\mu_s}$ cm^{-1}	Measurement-Method	Analysis-Method	Detector	λ (nm)	ReF
Intralipid 20% (Fresenius Kabi, Uppsala, Sweden) and Indian ink (Rotring waterproof)	$\star\star\varepsilon_{a\ il} \times 10^3 (mm^{-1})$ 2.25 ± 0.26	$\star\star\varepsilon_{s\ il} \times 10^3 (mm^{-1})$ 20.3 ± 0.3	Diffusive medium+Fiber [91]	Simple Inversion Procedure (Linear fit)	a	750	[92]
Intralipid ®20% (IL, Fresenius Kabi Italia, Italy) and Higgins Waterproof Black India Ink, Sanford, USA	$\star\star\varepsilon_{a\ ink} \times 10^3 (mm^{-1})$ 39.0±1.0% 34.0±1.0% 30.0±1.0%	$\star\star\varepsilon_{s\ il} \times 10^3 (mm^{-1})$ 25.1±1.5% 26.0±2.0% 22.3±2.0%	Double Integrating Sphere	IAD Linear method	b	633 751 833	[93]
Methylene Blue (M9140, Sigma-Aldrich, Missouri, USA), Intralipid ®20% (batch 10FH1726,Fresenius Kabi, Germany) and water	1-85 d=0.55 mm 1-65 d=1.1 mm	250- 25 d=0.55 mm 300-15 d=1.1 mm	Double Integrating Sphere	IAD	c	450-2400	[94]

$\star\star\varepsilon$ Intrinsic Coefficient, Double Integrating Sphere (DIS) $\star$ Detectors : (a) Photomultiplier tube(PMT); (b) RT-060-SF sphere with SDA-050-U detector (Lab sphere Inc., North Sutton, NH, USA) ; (c) Peltier-cooled extended-InGaAs detector (PDA10DT-EC Thorlabs Inc., New Jersey, USA) 1050-2250 nm and a Si detector (PDA100A) for the 500-1050 nm range; (d) Fiber Probe Cables (5) 250μm diameter; (e) (ISP-75, Instrument Systems Optische Messtechnik GmbH, Munich, Germany); (f) Blue enhanced silicon detector, Edmunds Optics Inc., Barrington, New Jersey; (g) Bidirectional Reflectance and Transmittance Distribution Function; (h) Photodiode; (I) Photo-dyne Model 66 XL radio-meter

Table 2.2: A summery of the Optical parameters of the tissue body phantoms, by different research groups

Tissue Body Phantom	μ_a cm^{-1}	$\acute{\mu_s}$ cm^{-1}	Measurement-Method	Analysis-Method	Detector	λ (nm)	ReF
Indian ink 1.2% and Intralipid 1.6%	0.36±1.25% 0.32±1.4% 0.31±1.3% 0.66±1.85%	13.4±0.85% 11.2±0.65% 11.0±0.75% 8.75±0.80%	Fiber Probe	Multiple Polynomial Regression (MPR)	d	660 785 805 974	[95]
(RTV Silicon Rubber and TiO_2-particles) to make Maternal, fetal and blood tissue phantom	MAT= 0.13 Fetal =0.16 Blood =2.81	MAT= 10.77 Fetal =9.71 Blood =0.82	Double-Integrating Sphere	KM-Method	e	960	[96]
Polyurethane,(TiO_2) scatterer and carbon black absorbing component (Biomimic, INO Inc Quebec, Canada)	0.118±2.4% d=5.08 mm 0.111±2.25% d=5.08 mm	0.94±6.0% d=5.08 mm 0.111±2.25% d=5.08 mm	Double Integrating Sphere	IAD [97]	f	543.5 632.8	[98]

Table 2.3: A summery of the Optical parameters of the tissue body phantoms, by different research groups

Tissue Body Phantom	μ_a cm^{-1}	$\acute{\mu_s}$ cm^{-1}	Measurement-Method	Analysis-Method	Detector	λ (nm)	ReF
(TiO_2) scatterer and carbon black absorbing componen.(Biomimic, INO Inc., Quebec, Canada)	0.064±20.7% d=4.81 mm	10.24±0.29% d=4.81 mm	Double Integrating Sphere	MCML [99]	g [100]	805	[101]
10%- Intralipid, and 0.1% India ink (Faber-Castell, TN)	0.0029 ±	0.0134 60 ± 8	Glass Cuvette	Radiative Transfer Theory [102]	h	633	[103]
20% Intralipid (Fresenius Kabi Clayton, L.P. Clayton, NC lot ♯ 1022848) 10% water diluted	2.4± 0.6	170± 8.0	Double Integrating Sphere	If(D) curve and MC model	h	633	[104][105]
Intralipid-10% (KabiVitrum, Clayton, NC) India ink (Pelikan, Germany)	0.055±0.02 35.99±4.28	0.65±0.05 3.25±2.25	Double-Integrating Sphere	IAD	I	1064	[106]

Table 2.4: A summery of the Optical properties of the breast cancer by different research groups

Tissue Body Phantom	μ_a cm^{-1}	$\acute{\mu_s}$ cm^{-1}	Measurement-Method	Analysis-Method	Detector	λ (nm)	ReF
Infiltrating CA N=48	0.147±0.143 0.044±0.083 0.100±0.188	10.914±5.5948 10.125±5.048 9.097±4.5368	Double Integrating Sphere	IAD	Photodetector (71822, Oriel, Stratford, CT)	749 789 836	[107]
Fatty Normal N=23	0.184±0.159 0.082±0.104 0.108±0.097	8.477±3.428 7.673±2.567 7.274±2.400	Double Integrating Sphere	IAD	Photodetector (71822, Oriel, Stratford, CT)	749 789 836	[108]
Normal tissues	23± 0.091	7.82±0.02	Fiber Probe	Monte Carlo (MC)	CCD camera	633	[109]
Malignant tissues	10.2±0.19	29.03±0.02	Fiber Probe	Monte Carlo (MC)	CCD camera	633	[109]
Normal tissues (Semi-Infinite Medium)	0.003 0.002 0.004 0.001	1.100 0.890 0.890 0.891	Fiber Probe	FDPM [110]	Avalanche photodiode (Hamamatsu model C5658)	674 811 849 956	[111]

⋆⋆ Diffuse Optical Imager (DOI), Frequency-Domain Photon Migration (FDPM), Diffusion Approximation (DA)

Table 2.5: A summery of the Optical properties of the breast cancer by different research groups

Tissue Body Phantom	μ_a cm^{-1}	$\acute{\mu_s}$ cm^{-1}	Measurement-Method	Analysis-Method	Detector	λ (nm)	ReF
Malignant tissues (semi -infinite medium)	0.007 0.007 0.008 0.0167	0.799 0.677 0.666 0.665	Fiber Probe	FDPM [110]	Avalanche photodiode (Hamamatsu model C5658)	674 811 849 956	[112]
Healthy breast tissue(in-vivo)	0.046±0.027 0.041±0.025 0.046±0.024	8.3±2.0 8.5±2.1 8.7±2.2	(Compressed Breast)	FDPM+DA+MC [54, 113]	Fiber Coupled PMT	830 786 850	[114]
Breast tissue for PDT	0.03-1.06	1.2-40	DOI (Compressed Breast)	(Reflectance +TOF) Spectroscopy	Fiber Coupled PMT	600-900	[115]

3

Tissue Optical Parameter Measurements (Publication I and II)

3.1 Addendum

3.1.1 Accessories to Measure R_d and T_d

The accessories consist of Double Integrating Sphere (Optoprim Germany), each sphere has a diameter of 300 mm and 20 layers of $BaSO_4$. There are two stoppers of 1 inch diameter were locally fabricated to measure the reference signals and optical fiber 200μm. An Ava-spec, Russia, 2048 spectro-photometers and a red λ=632.8 nm He-Ne laser 17 mW output power. The Integrating sphere set up is shown in the figure 3.1.

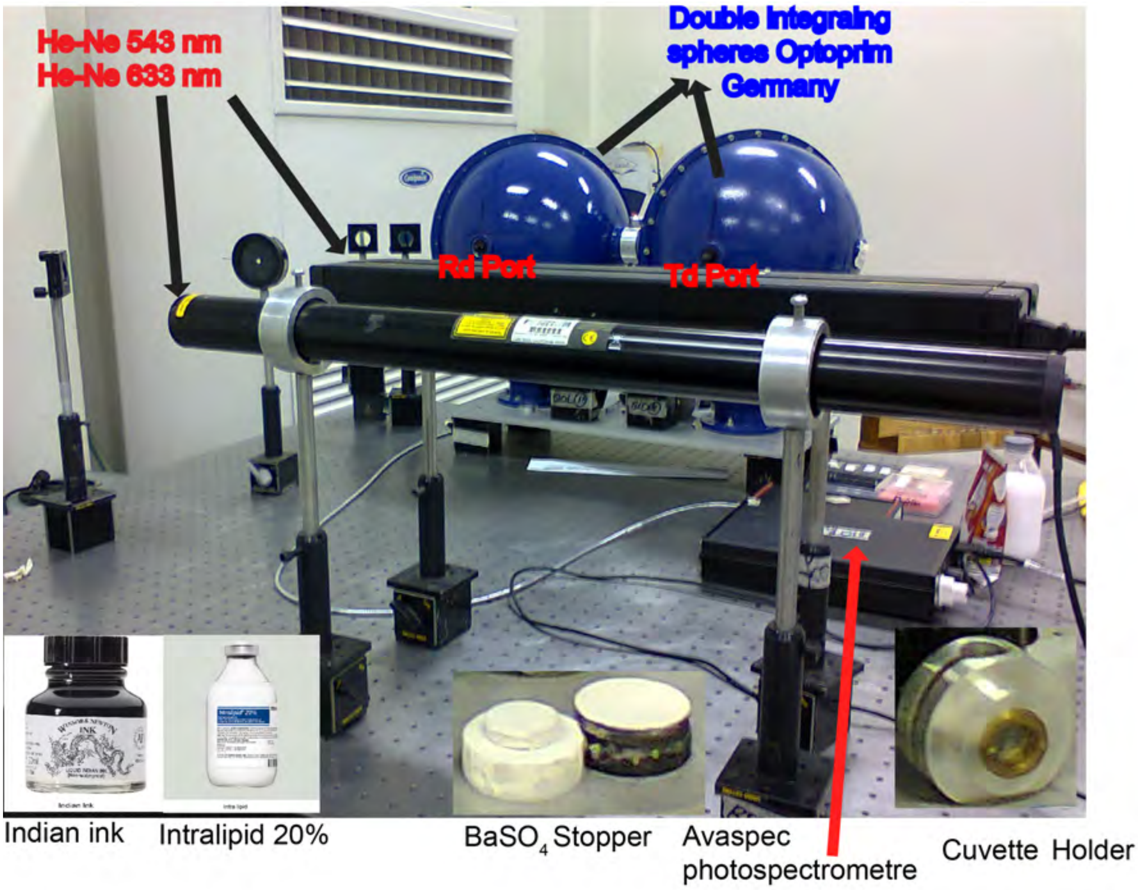

Figure 3.1: Real experimental set up

3.1.2 Integrating Sphere System calibration

Different groups of scientist use uniform microspheres (Duke Scientific Corporation), 10%, 20% Intralipid and Indian ink for the integrating sphere calibration. To draw the linearity curve for scattering coefficient μ_s from the measured values of R_d and T_d, Indian ink concentration is fixed while Intralipid concentration is varied according to the requirement of biological tissues. Similarly to draw the linearity curve of absorption coefficient μ_s from the measured values of R_d and T_d, The concentration of Intralipid is fixed is while the concentration of Indian ink is varied according to the requirement of biological tissues [82–84]. The table 3.1 and table 3.2 show the prepared samples for tissue body phantoms. Table 3.3 shows the concentration of Intralipid used for absorption and scattering coefficient. Here S.S stands for Stock Solution.

Table 3.1: % Intralipid samples Indian Ink$_{fix}$,total volume of the solution V_{total} (μl)

% Intralipid Rqd	0.1% Intralipid S.S (V)(μl)	Water (V) (μl)
0.01	0500	4500
0.02	1000	4000
0.03	1500	3500
0.04	2000	3000
0.05	2500	2500
0.06	3000	2000
0.07	3500	1500
0.08	4000	1000
0.09	4500	0500
0.10	5000	0000

Table 3.2: % Indian ink sample Intralipid$_{fix}$,total volume of the solution V_{total} (μl)

% Indian-Ink Rqd	0.01% Indian-Ink SS (V) (μl)	Water (V) (μl)
0.001	0500	4500
0.002	1000	4000
0.003	1500	3500
0.004	2000	3000
0.005	2500	2500
0.006	3000	2000
0.007	3500	1500
0.008	4000	1000
0.009	4500	0500
0.010	5000	0000

Table 3.3: Different concentration of Intralipid solution used,total volume of the solution V_{total} (μl)

%Intralipid	10% Intralipid S.S (V) (μl)	Water (V) (μl)
0.5	0250	4750
1.0	0500	4500
1.5	0750	4250
2.0	1000	4000
2.5	1250	3750
3.0	1500	3500
3.5	1750	3250
4.0	2000	3000
4.5	2250	2750
5.0	2500	2500
5.5	2750	2250
6.0	3000	2000
6.5	3250	1750
7.0	3500	1500

3.2 Motivation for Optical Parameter Measurement

During light-tissue interactions, some part of light penetrates in the tissue while most of the light scatter. To find the actual contribution of each constituent of the tissue, exact knowledge of optical parameters of tissue absorption coefficient (μ_a), scattering coefficient (μ_s) and anisotropy g is necessary. Moreover, the malignant tissues, having significantly higher (absorption coefficients μ_a and reduce scattering coefficients $\acute{\mu_s}$=μ_s(1-g)) lower the Signal to Noise Ratio (SNR).

We have fabricated a unique sample holder using microscopic coverslips to measure the signal from highly concentrated Intralipid and Indian-ink tissue mimic body phantoms. The diffuse reflectance R_d and diffuse transmittance T_d of 1.0% Indian-ink and 20% Intralipid tissue body phantoms have measured by placing the sample holder in an Integrating Sphere System at λ=632.8 nm and Inverse Adding-Doubling method used to calculate optical parameters (μ_a and $\acute{\mu_s}$) from measured values of R_d and T_d.

3.3 Author's Contribution to Publication-I

Being the principal author of this paper, Ph.D. candidate (Aziz ul Rehman) performed the whole experimental work, made the tissue body phantoms and produced all the data for each tissue body phantom, implemented Inverse Adding Doubling (IAD) method to calculate optical parameters and wrote the manuscript. Second author Iftikhar Ahmed was responsible for proof reading, figures of our specially designed sample holder, and corresponded with the Editor of the Journal. All other authors, each has 5% contribution. They did the proofreading and helped to manage every facility needed to carry out this research work. Two papers were published from this data. Aziz ul; Rehman presented this work in SPIE conference held in Sydney in 2015.

3.4 Publication-I

All material adapted from the publication by Aziz ul Rehman, I Ahmad, K Rehman, S Anwar, S Firdous and M Nawaz, Optical properties measurement of highly diffusive tissue phantoms for biomedical applications Laser Physics 25, 025605 (2014)

Pages 34-40 of this thesis have been removed as they contain published material. Please refer to the following citation for details of the article contained in these pages.

Rehman, A., Ahmad, I., Rehman, K., Anwar, S., Firdous, S., & Nawaz, M. (2015). Optical properties measurement of highly diffusive tissue phantoms for biomedical applications. *Laser Physics*, 25(2):025605.

DOI: 10.1088/1054-660X/25/2/025605

3.5 Author's Contribution to Publication-II

Being the principal author of this paper, Ph.D. candidate (Aziz ul Rehman) did the whole experimental work, make the tissue body phantoms and generated all the data for each tissue body phantom, applied Inverse Adding-Doubling (IAD) method to calculate optical parameters and wrote the manuscript. All other authors, each have 5% contribution. They did the proof reading and helped to mange every facility needed to carry out this research work. Two papers were published from this data. Aziz ul Rehman presented this work in SPIE conference held in Sydney in 2015.

3.6 Publication-II

Aziz ul Rehman, K Rehman , S Anwar, S Firdous,and M Nawaz , Optical parameter measurement of highly diffusive tissue body phantoms with specially designed sample holder for photo diagnostic and PDT applications,Proc. of SPIE 9668, 966842-966841(2015).

Pages 42-47 of this thesis have been removed as they contain published material. Please refer to the following citation for details of the article contained in these pages.

Rehman, A., Rehman, K., Anwar, S., Firdous, S., & Nawaz, M. (2015). Optical parameter measurement of highly diffusive tissue body phantoms with specifically designed sample holder for photo diagnostic and PDT applications. *Proceedings of SPIE*, 9668:966842.

DOI: 10.1117/12.2202497

4

Optical Diagnostic of Breast Cancer (Publication III)

4.1 Tissue Optical properties

4.1.1 Fluorescence

During light-tissue interaction, molecules are excited by absorbing t light. Fluorescence is the emission of light when molecules or atoms make a transition from higher energy states to lower energy states. The emitted electromagnetic waves have longer wavelength (λ) or lower energy as compared to the energy absorbed by the molecules. This increase in wavelength of emitted light is due to Stokes shift $\triangle\lambda$, named after Irish physicist George G. Stokes and according to thumb rule it is ≈25-50 nm for most of the molecules [121]. The process of fluorescence can be best explained by Jablonski diagram as shown in figure 4.1 which is taken from [122]. The electronic transition for fluorescence from excited state of molecule to the ground state of a molecule can

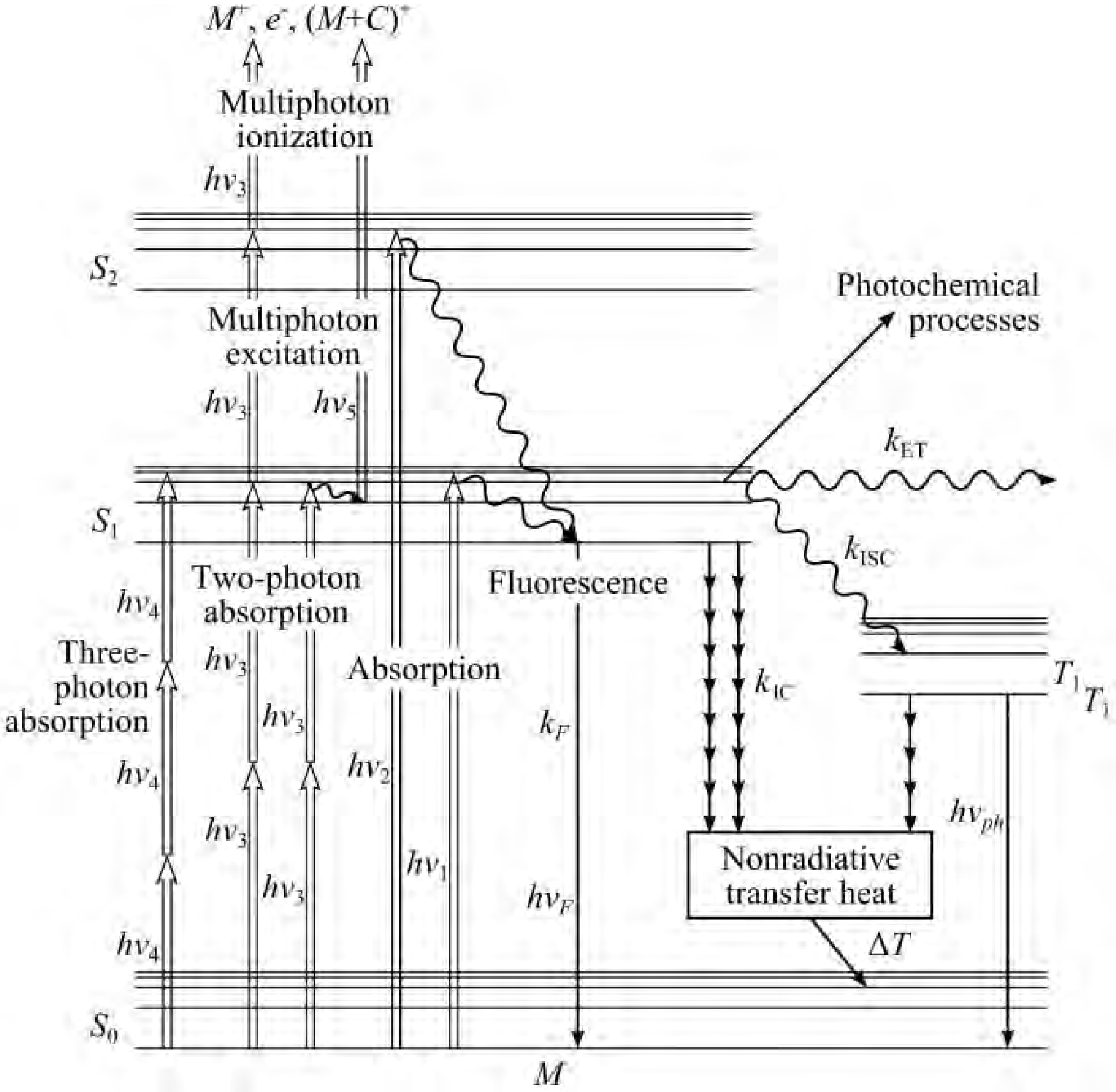

Figure 4.1: Jablonski diagram for tissue fluorescence, phosphorescence and non radiative decays.

be seen in figure 4.1. Its intensity is given by the absorbed intensity multiplied by fluorescence quantum yield) η_F and ratio of the solid angle made by the radiation with the detector Ω to the total solid angle 4π.

$$I_F(\lambda) = I_o(1 - exp(-\epsilon_\lambda c_a d)\eta_F \frac{\Omega}{4\pi}) \tag{4.1}$$

In case of monolayer equation 4.1 exponential higher terms can be neglected and equation 4.1 can be simplified as equation 4.2.

$$I_F(\lambda) = I_o \eta_F \epsilon_\lambda c_a d) \frac{\Omega}{4\pi} \tag{4.2}$$

The equation 4.2 shows that, fluorescence intensity is proportional to the concentration and η_F of tissue molecules.

4.1.2 Raman Scattering

Raman scattering is an inelastic scattering of light photons from molecules which are in higher vibrational levels during excitation state. It was discovered by C.V.Raman and K.S. Krishnan from liquid molecules [123–125]. Raman shift may be Stokes- or anti-Stokes depends upon the loose or gain of energy by the scattering photons. Raman shift is the characteristics of molecules so it can be used for diagnosis purposes. Raman spectroscopy which rely on Raman scattering is a very useful technique to see the biochemical change at the molecular level. It is used to differentiate normal and diseased cells and tissues [126]. Figure 4.2 which is taken from [127] explains the molecular level energy diagram where acronym MIR stands for mid-infrared, RS for Raman Scattering and RRS stands for Resonance Raman Scattering. Raman scattering signal is weak signal compared with fluorescence signal. There different type of Raman effects e.g., Surface-Enhanced Raman Scattering (SERS), Stimulated Raman Scattering (SRS), Resonance Raman scattering (RRS), and Coherent Anti-Stokes Raman Scattering (CARS), which give less fluorescence background for bio-molecules.

4.1.3 Polarization Imaging and Muller Matrix Polarimetry

Bio-molecules are birefringent and they rotate the state of polarization when light fall on them [128, 129]. The ability to rotate the sate of polarization differs for normal and diseased molecules, so it can be used for diagnosis. Polarization imaging is used to differentiate tissue and cells. The Mueller matrix imaging of the breast cancer samples were obtained from λ=400-800 nm of light experimentally. By measuring optical polarization parameters (transmission and reflection), 4×4 Mueller matrix can be generated [130]. The main important parameters from 4×4 Mueller matrix are the diagonal elements M_{11}, M_{22}, M_{33}, and M_{44}. These diagonal elements of the Mueller matrix give retardance, diattenuation, and depolarization of the sample under investigation. By decomposing the measured Mueller matrix into retardance, diattenuation, and depolarization components can provide a complete description of effect of light state in a sample. In Muller matrix polarimetry, there is a common way to express Muller matrix

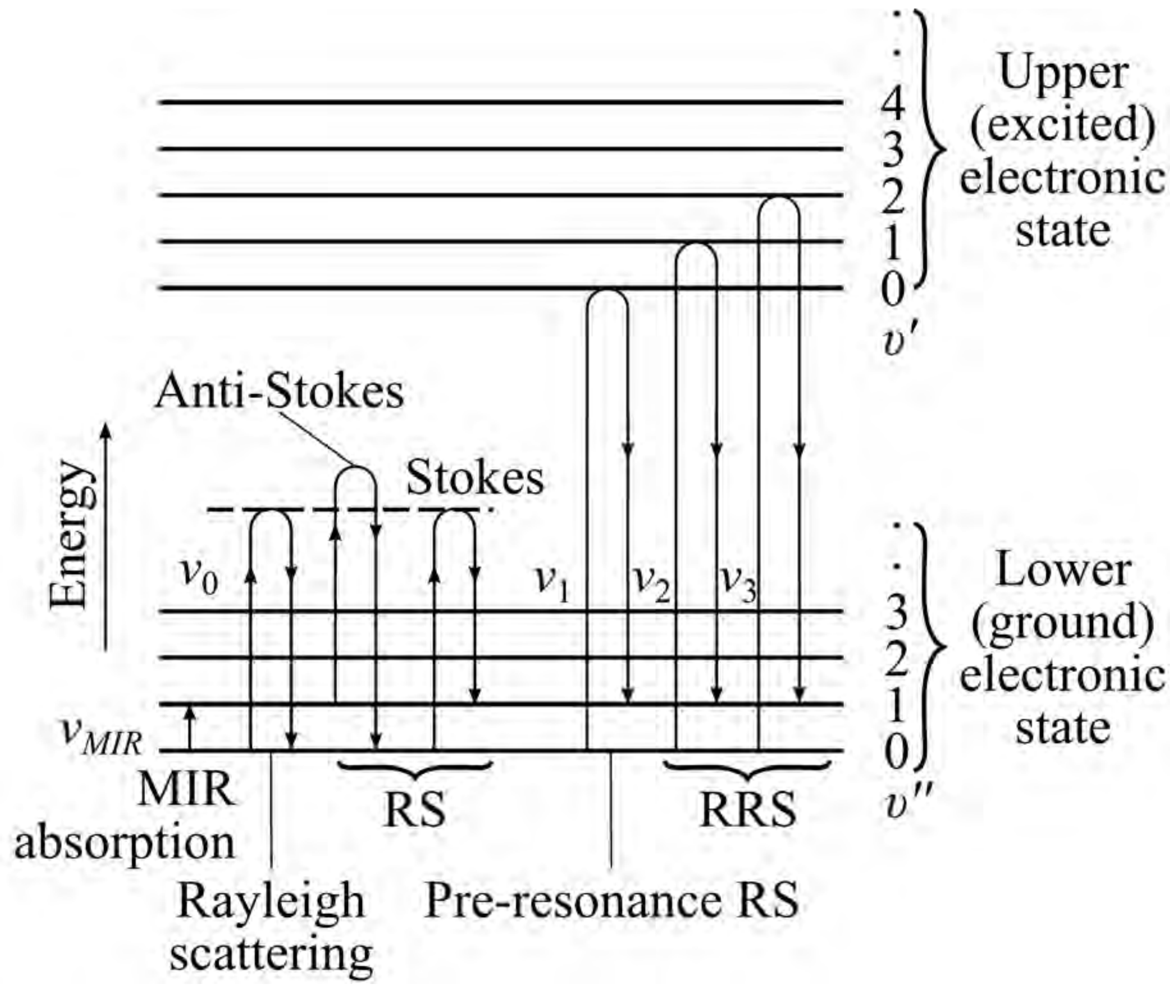

Figure 4.2: Raman scattering illustration using a molecular energy level diagram, $\acute{v}$ and $\acute{\acute{v}}$ are the vibrational states of the molecule

without any dimension. [131]. In our experiment we have scanned the circle marked ROI as in figure 2 of the publication III as 16×16 (106.0 $\mu m^2/pixel$) [132].

4.2 Motivation for Optical Diagnostic of Breast Cancer

The optical detection of early biochemical changes associated with the benign tumor, before the pathological diagnosis can revolutionize the cancer diagnostics. The best way to improve the survival rate of breast cancer is that it should be detected as early as possible. According to the National Cancer Institute, up to 20% of all breast cancers fail to be discovered by x-ray mammography (uses ionizing radiation) [133]. The ultra-sound and MRI provide high spatial resolution, but comparatively less information about the molecular-level changes [134, 135]. Raman spectroscopy along with fluorescence and polarimetric imaging is the best solution to diagnose breast cancer as early as possible.

4.3 Author's Contribution to Publication III

We obtained the breast tissue samples from the pathology department of Pakistan Institute of Medical Sciences (PIMS) Islamabad Pakistan thorough clinical history and patients consent after a surgical breast biopsy and shaped into tissue block after passing through formalin fixing method. Aziz ul Rehman completed fluorescence microscopy section. Shahzad Anwar completed Raman spectroscopy section. Dr Shamaraz Firdous completed the polarimetry section. Each of the authors has written his relevant part, and Dr Shamaraz Firdous made correspondence with the editor.

4.4 Publication III

Shahzad Anwar, Shamaraz Firdous, Aziz ul Rehman and Muhammad Nawaz, Optical diagnostic of breast cancer using Raman, polarimetric and fluorescence spectroscopy. Laser Physics Letters 12, 045601 (2015).

Pages 54-60 of this thesis have been removed as they contain published material. Please refer to the following citation for details of the article contained in these pages.

Anwar, S., Firdous, S., Rehman A., & Nawaz, M. (2015). Optical diagnostic of breast cancer using Raman, polarimetric and fluorescence spectroscopy. *Laser Physics Letters*, 12(4):045601.

DOI: 10.1088/1612-2011/12/4/045601

5

Integrating Sphere Light Sources (Publication IV)

5.1 Excitation Spectrum of Common Fluoropheres

The excitation spectra of the native fluoropheres in a cell are determined from excitation wavelengths. For this, biological samples (cells and tissues) are excited at appropriate wavelength (λ). Figure 5.1 is taken and modified from reference [136] gives the excitation spectra of commonly known fluoropheres in a cell, including NADH, FAD, and porphyrin. The idea for light source fabrication was derived keeping in view the excitation spectra of common fluoropheres.

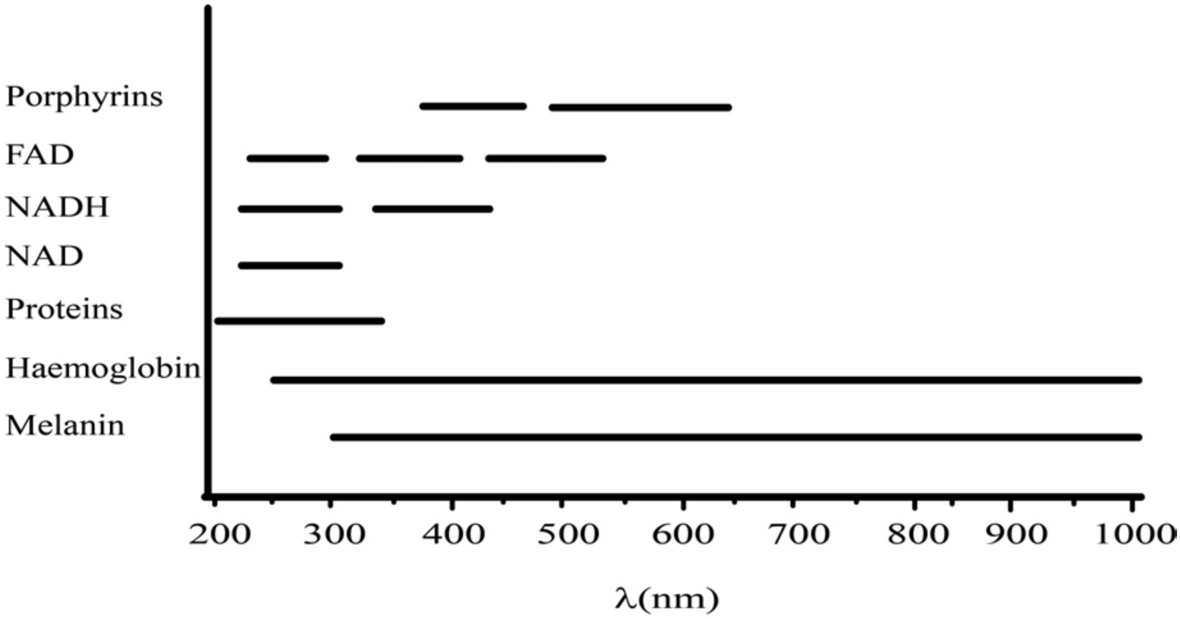

Figure 5.1: Spectral absorption ranges of tissue chromopheres NADH, NAD, FAD etc.

5.2 Emission Spectrum of Common Fluoropheres

Fluorescence is the emission of light when molecules or atoms make a transition from higher energy states to lower energy states. The emitted electromagnetic waves have longer wavelength (λ) or lower energy as compared to the energy absorbed by the molecules. Figure 5.2 which taken and modified from [4] shows the emission spectrum, of common fluoropheres which is helpful in emission filters selection in a filter cube.

5.3 Motivation to Build Light Source

Mercury lamp with suitable optical filters are used for wide-field fluorescence microscopy. Since mercury lamp has a spectrum with characteristic absorption peaks and very less power in ultra violet (UV) range especially 340 nm and 365 nm. These are the wavelengths on which most important of the key fluoropheres NADH, FAD can be excited. The $Baso_4$ coated integrating sphere along with high power deep UV light emitting diodes (LEDs) are enough to build these type of light source. Deep UV LEDs are available in open market in these days. The idea is to build a light source which has the uniform spatial profile and can be tuned across electromagnetic spectrum especially in the spectral region where most important fluoropheres can be excited. In this study

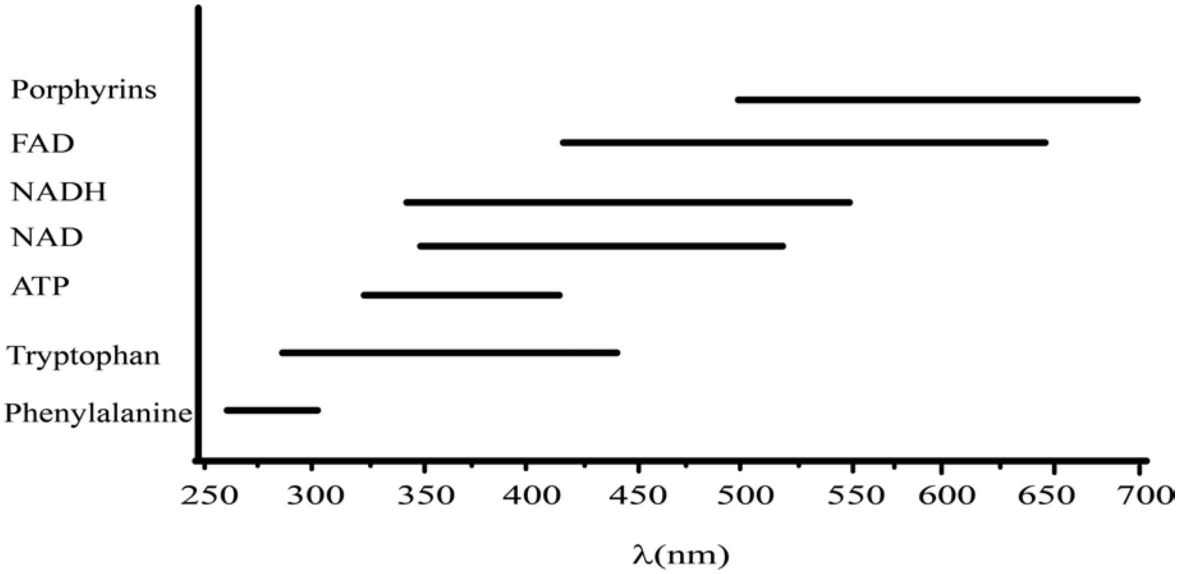

Figure 5.2: Spectral emission ranges of tissue chromophores NADH, NAD, FAD etc.

Deep UV LEDs light source is retrofitted in to the LSC Leica-DMIRB Microscope to do fluoresence microscopy on room temperature along with CMOS camera instead of EMCCD. The end use of this light source is to do single channel hyperspectral fluoresence imaging to monitor PDT of biological tissues.

5.4 Author's Contribution to Publication IV

Being the principal author of this paper, the Ph.D. candidate (Aziz ul Rehman) discussed this idea with principal supervisor Ewa M. Goldys. Author purchased the accessories like filter cubes, high power LEDs, power source to operate LEDs, made the controller circuit from Macquarie University MET services to operate the LEDs. He did the whole experiment and acquired data analysed it and wrote the article. Being the Principal supervisor Ewa Guided on each step in the manuscript and did revisions until it is finalized and published. Fluoresence Microscopy was performed on BV_2 cells so Ayad Anwer helped in cell culturing and wrote the method for it.

5.5 Publication IV

Material taken from Aziz ul Rehman, A.G. Anwer, E.M. Goldys, Programmable LED-Based Integrating Sphere Light Source for Wide-Field Fluorescence Microscopy, Photodiagnosis and Photodynamic Therapy 20 201-206 (2017)

Pages 65-70 of this thesis have been removed as they contain published material. Please refer to the following citation for details of the article contained in these pages.

Rehman, A., Anwer, A. G., & Goldys, E. M.. (2017). Programmable LED-based integrating sphere light source for wide-field fluorescence microscopy. *Photodiagnosis and Photodynamic Therapy*, 20, p.201-206.

DOI: 10.1016/j.pdpdt.2017.10.002

5.6 Supplementary Material

Supplementary material includes Integrating Sphere dimensions, reflexivity curve of the Integrating Sphere, PISAL source electronic circuit diagram, and real experimental setup.

5.6.1 Light Source Conceptual Diagram

An integrating sphere conceptual light source is shown in figure 5.3

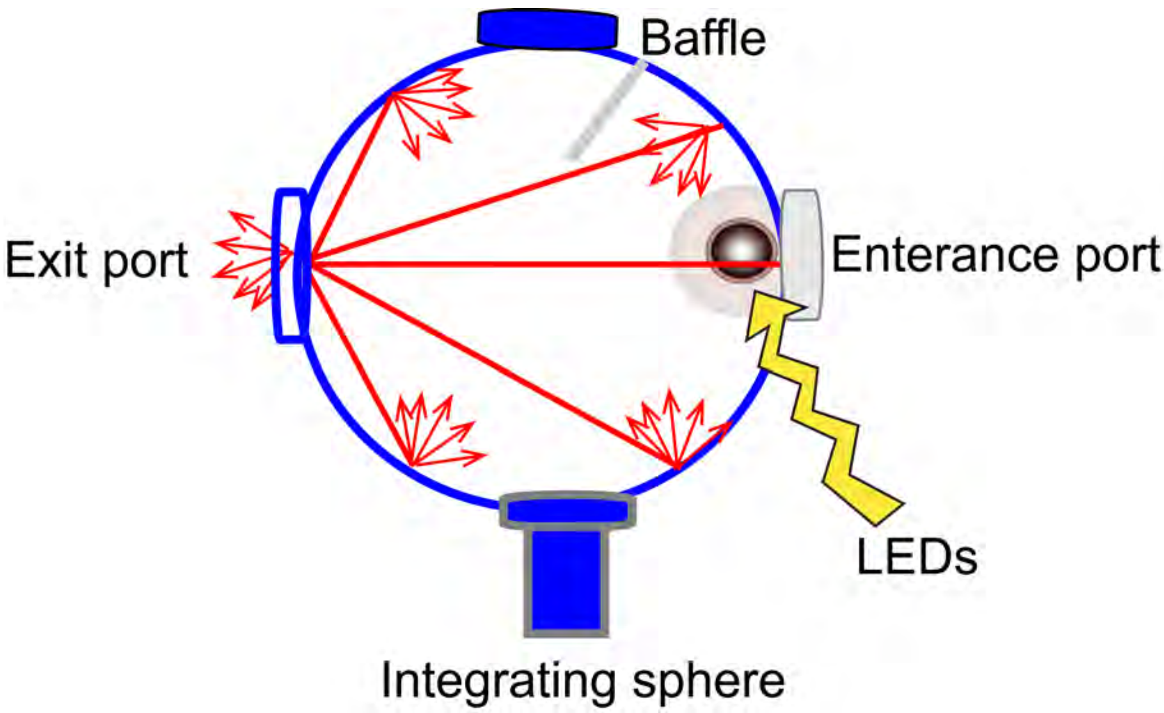

Figure 5.3: Integrating Sphere light input and light output diagram

5.6.2 Barium Sulphate Reflectance Spectrum

Reflectivity curve for $BaSo_4$ and PTFE is shown in the figure 5.4 which is taken and modified from [137]

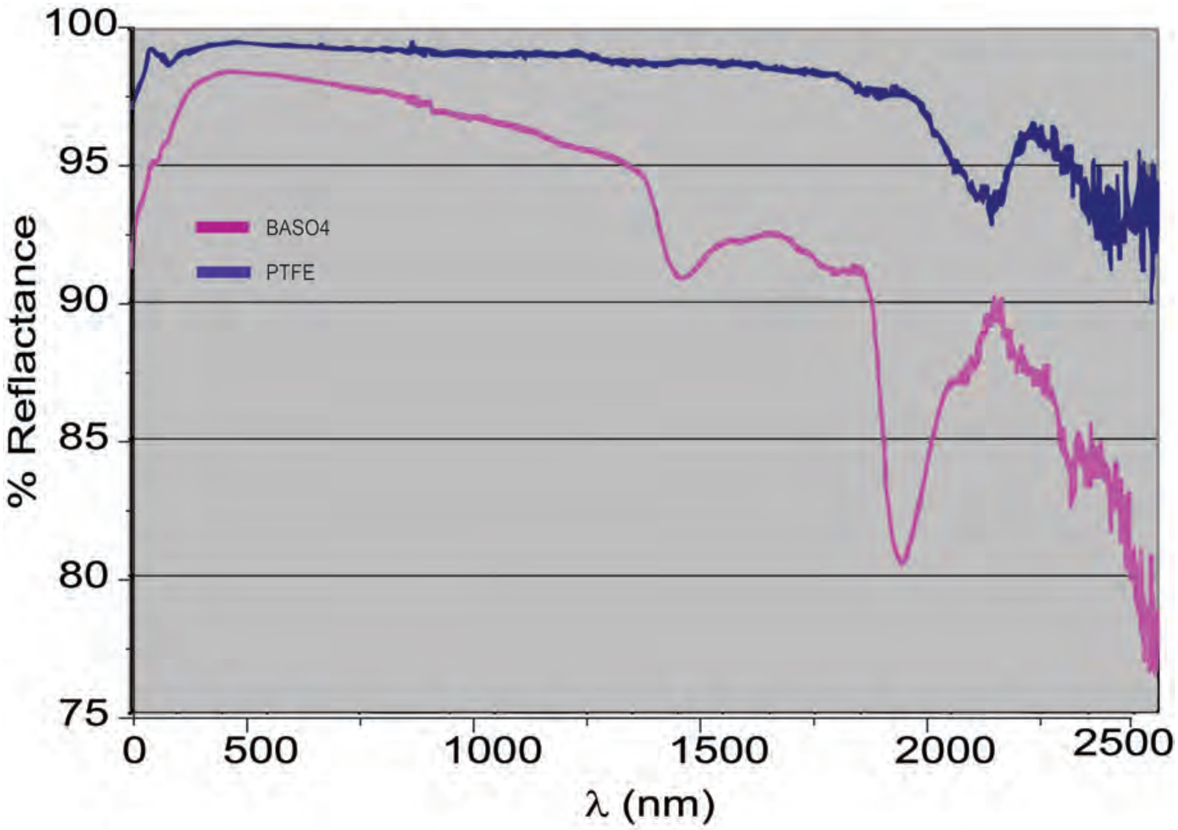

Figure 5.4: Reflectivity curve of the $BaSO_4$ and PTFE

5.6.3 Real Experimental Setup

It is a general purpose integrating sphere, its diameter is 152 mm and a hole was tapped to fit the LEDs mounting head. A real setup for the light source is shown in the figure 5.5.

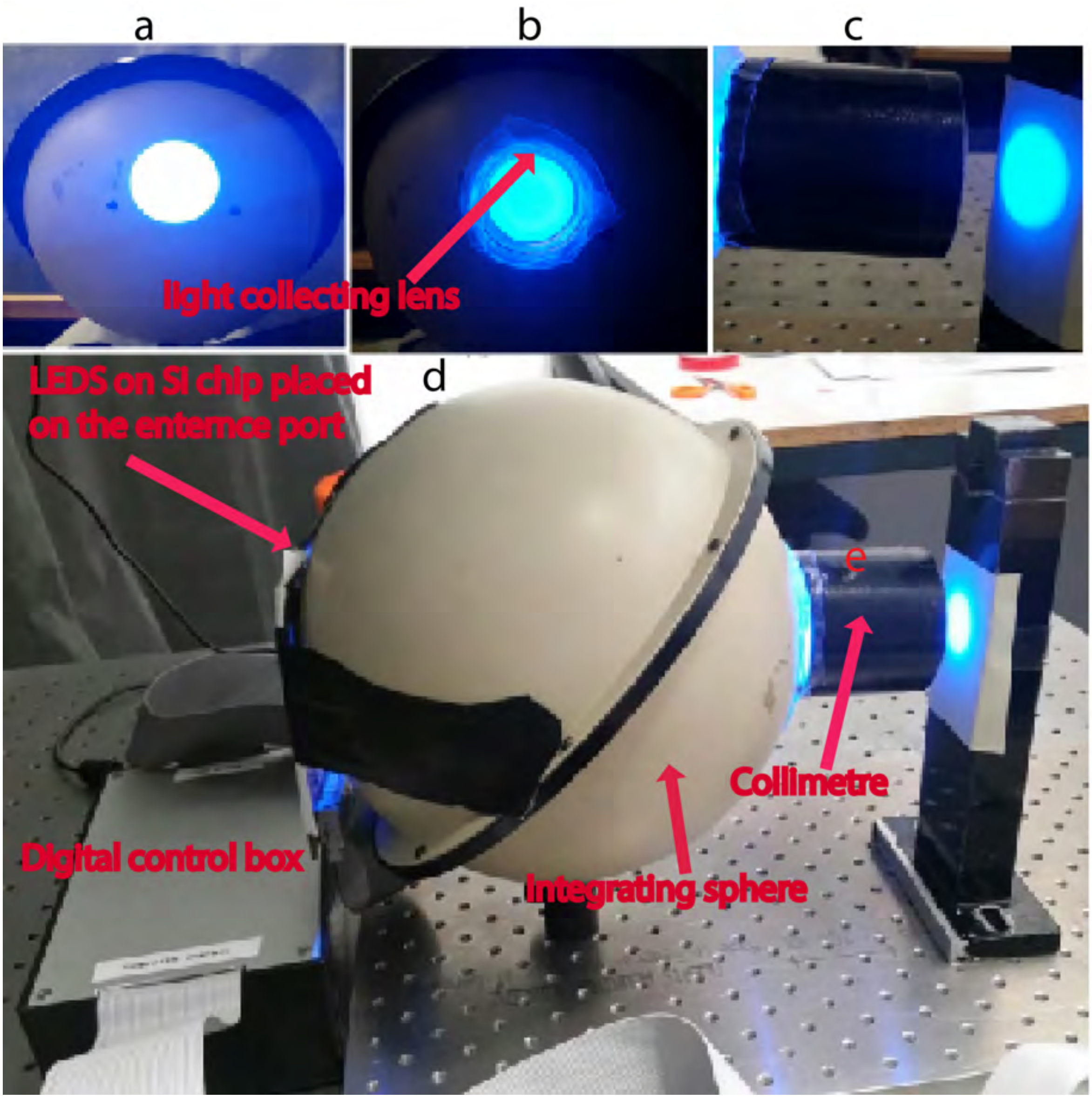

Figure 5.5: (a) integrating sphere as a light source without any Lens spreading light in all direction (b) Integrating sphere as a light source with light collecting lens (UV fused silica Plano Convex lens uncoated D=50 and F=60.0) (c) beam spot from the light source after passing through the collimator (d) The complete light source along with control box and collimator showing the light spot during operation (e) It is commercial collimator taken from DM IRB (Leica) to collimate the light coming from the sphere

5.6.4 Electronic Controller

Electronic controller circuit diagram and mounting head for LED is shown in the figure 5.6

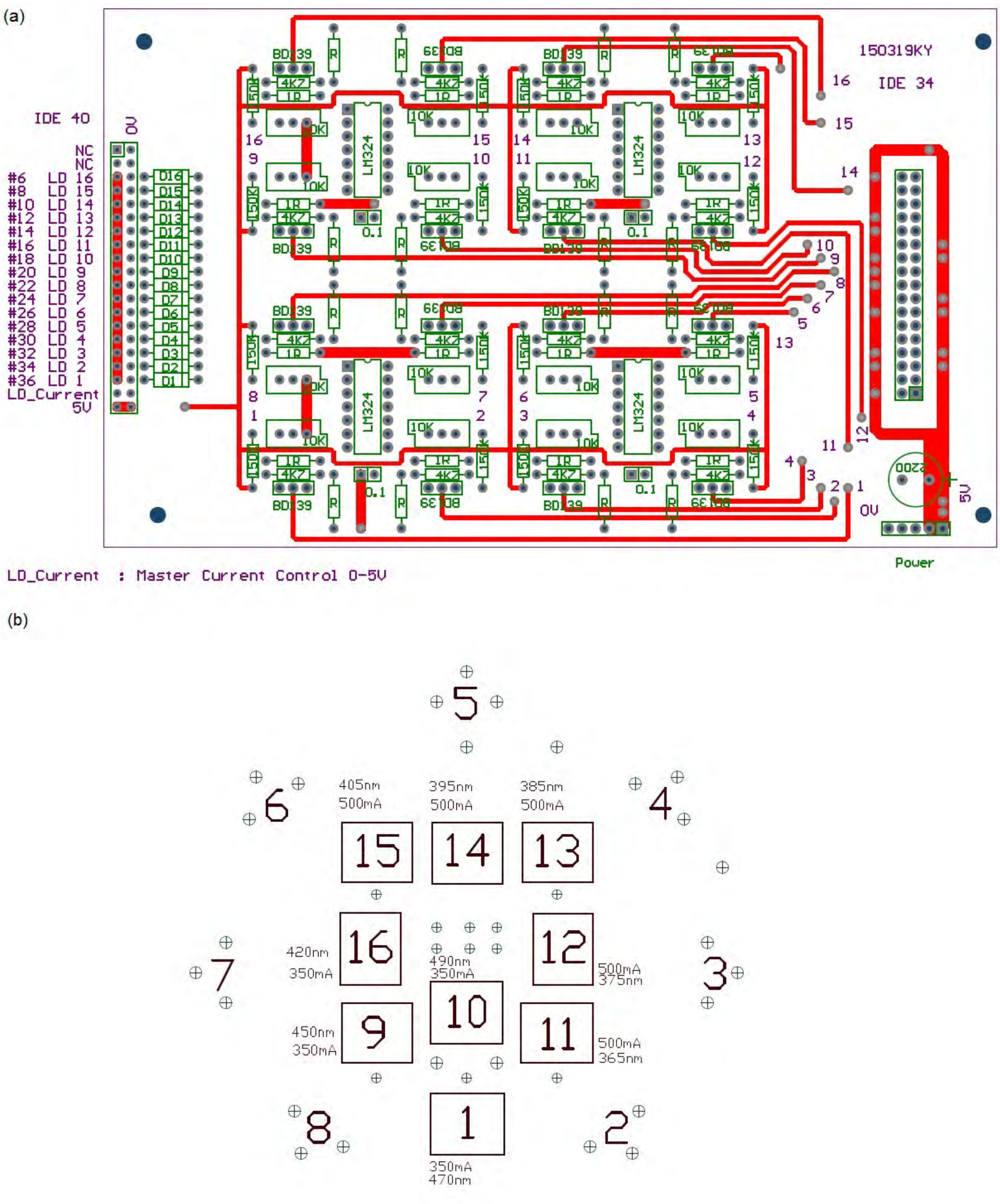

Figure 5.6: LED controller PC circuit diagram

6

The Hyperspectral Imaging and Unmixing in Biological Tissues (Literature Review Part-2)

6.1 Summery of Literature Review

Hyperspectral Fluorescence Imaging (HSFI) is a well-known technique in the medical research field and is considered as a non-invasive tool for tissue diagnosis. Implementation of HSFI imaging along with feature selection and extraction techniques are useful for image analysis. This literature review gives a brief introduction to hyperspectral imaging acquisition methods and its types. We presented the image analysis, pre-processing methods, feature extraction and selection methods and data classification techniques. The coupling of hyperspectral imaging systems with well-known optical modalities like Raman scattering microscopes, fundus cameras, confocal and conventional microscopes is discussed. The fusion of unsupervised unmixing techniques with classification methods i.e., the combination of Support Vector Machine with an Artificial Neural Network and Snapshot Hyperspectral Imaging with Vortex Analysis Techniques is outlined. Finally, we discussed the recent application of Hyperspectral Imaging System for cellular differentiation of different types of cancer.

6.2 Introduction

A conventional RGB image contains three colours, red, green, and blue, but a hyperspectral image can have many colours depending on the number of channels used for imaging across the whole electromagnetic spectrum. The absorption, scattering, and transmission are main type interaction of electromagnetic rays with cells and tissue. The interactions give rise to a lot of information from the tissue in the form of spectral images used for analysis. Every individual constituent or fluorophore present in the cells or tissues, when interacting with electromagnetic radiation carries an intrinsic spectral signature with it. An unknown fluorophore can be identified after making a comparison with intrinsic spectral signature. In Hyperspectral Imaging System(HSFI), we use both spectral and spatial intrinsic signatures to create a 3-D data called hyperspectral data-cube. So in hyper-spectral data-cube, there are three dimensions (x,y,λ), first two (x, y) represent spatial dimensions of molecule while the third one represents the spectral signature (λ) for hyperspectral imaging. Every pixel of the spectral image carries some spectral signature. A HSFI has an excellent potential for non-invasive diagnosis of malignant diseases.

Biological tissue behaves as turbid mediums and transportation of light through it incurs multiple scattering from tissue surface along with absorption in melanin, water, and haemoglobin [136, 138, 139]. The hyperspectral image which is formed by the reflection, fluorescence or transmission of light from tissue contains quantitative diagnostic information about tumour delimitation, identification, and pathological conditions [140]. The idea of the hyperspectral image initially developed for remote sensing [141] and now this technology has been successfully implemented in other research areas in the medical field. Now there are numerous application of hyperspectral imaging to diagnose the malignant diseases such as cancer using label-free non-invasive methods. Currently, the hyperspectral imaging sensors are being used to capture and build a λ-I profile of a scene with exceptionally high spatial and spectral resolution [142]. The HSFI Applications include (agriculture [143–145], eye care [146, 147], food processing [148, 149], mineralogy [150, 151], detection of environmental pollutants [152], chemical imaging, astronomy for space and surveillance [153, 154] and medical in-vivo and in-vitro diagnostics [155] in the surgical marking of tumors [156, 157]).

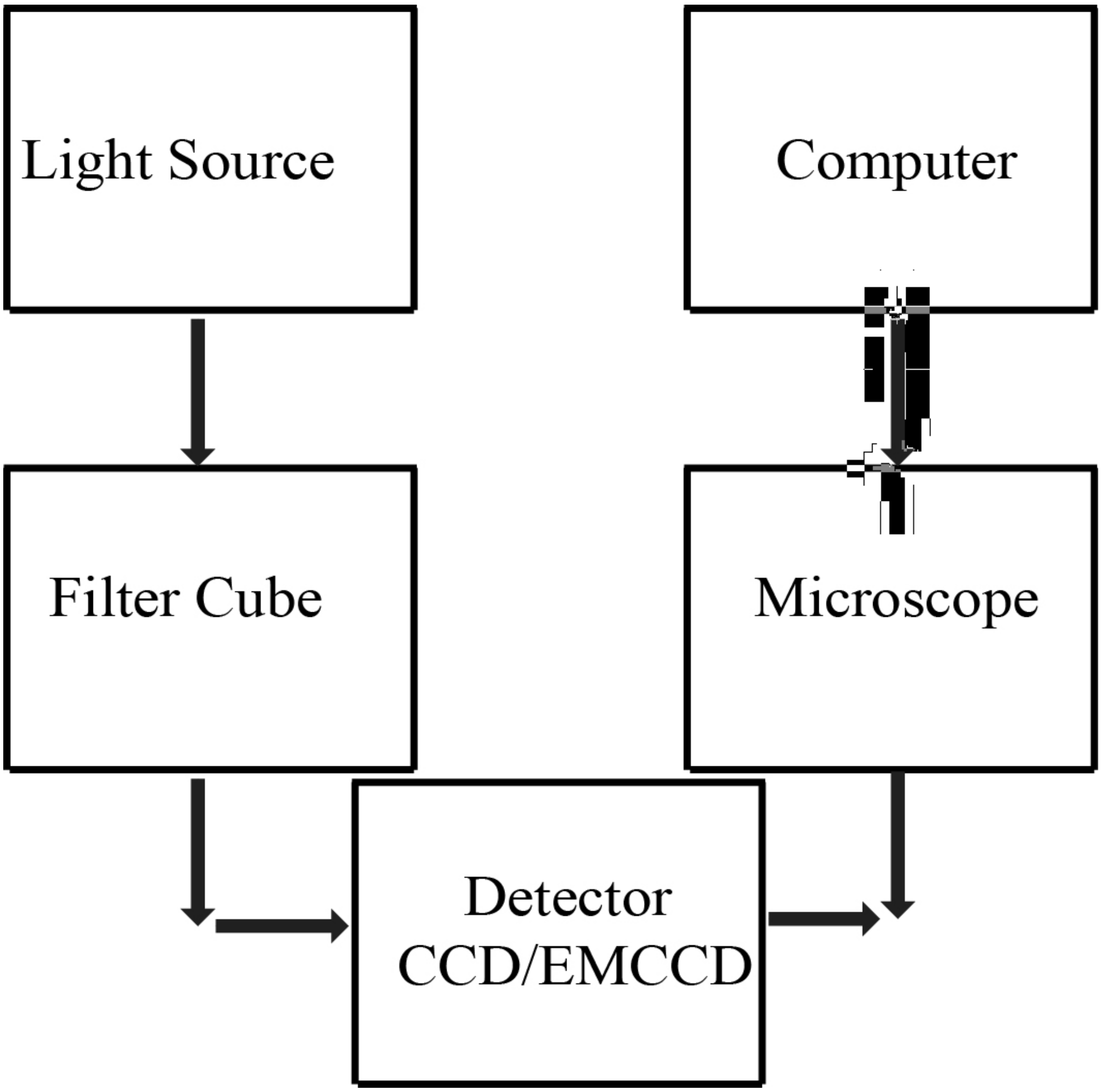

Figure 6.1: Schematic diagram of a typical auto-fluorescence Hyperspectral Imaging System.

6.3 Fluorescence Hyperspectral Imaging System

A HSFI system consists of the following components

- A light source lamp combination with a monochromator for λ selection, or LEDs of suitable λ.
- A filter cube (exciter, dichroic and emitter.
- A microscope along with suitable objective to image tissues.
- A detector (CCD/EMCCD) array with suitable quantum efficiency.
- A computer system to operate the whole imaging system.

The schematic diagram of HSFI is shown in figure 6.1

6.4 Hyperspectral Image Acquisition Methods

There are four hyperspectral image acquisition methods which include Spatial, Spectral, Snapshot and Spatio-Spectral scanning. They acquire a three-dimensional (X,Y,λ) data-set i.e., hyperspectral data cube. Here X and Y represent the spatial coordinates while the λ coordinate corresponds to the spectral dimension and can have any value across the whole electromagnetic spectrum depending on the availability of light source, detectors, and the particular application. We will discuss each of the acquisition methods below, addressing in detail.

6.4.1 Spatial Scanning Hyperspectral Imaging Method

In this hyperspectral imaging method, a complete spectrum for each pixel obtained spectrally (like in point or line scanning than system scans spatially throughout the image area). Figure 6.2 (a) which is taken and modified from reference [158–160] shows the line or push-broom scanning. An optical slit formes a thin strip of the image which passes through a dispersive device which creates the image on the detector as shown in figure 6.2(b). So, a grating can produce a high spectral resolution image having maximum spectral information in spatial scanning systems because it spatially cover a small image area. Line scanning, consisting of whisk-broom or push-broom

HSFI, is not able to provide a live display of images. Devices based on this type of acquisition method were mainly installed in applications, such as quality control in food production, airborne mounted systems, food inspection and geological remote-sensing applications [161, 162].

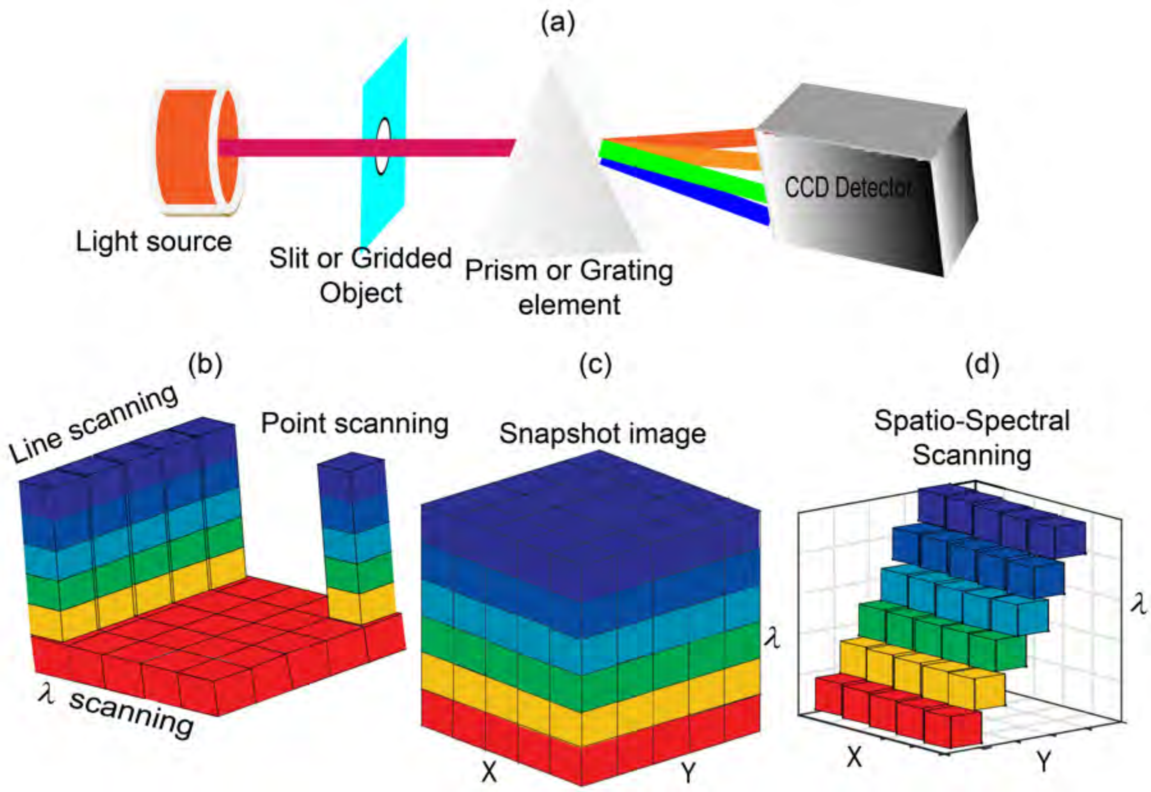

Figure 6.2: (a) A diagram demonstrating the essential components used in a line or Push-Broom Scanning Hyperspectral Imaging System. A slit permits a small portion of the incoming light from a source to split into different wavelengths via a prism or grid. A CCD/EMCCD detector records information corresponding to each λ, stored in a hyperspectral data-cube (b) Image output storage format depends upon the method of scanning (line scanning, point scanning, λ scanning, (c) Snapshot Scanning and Spatio-Spectral scanning) with a data-cube construction per unit time for each hyperspectral imaging technique.

6.4.2 Spectral Scanning Hyperspectral Imaging Method

Spectral-scanning hyperspectral systems capture the full scene in a single exposure with 2-D detector arrays and then make a λ scan to complete the hyperspectral data cube. An Acoustic Optical Tunable Filter (AOTF) is used to tune the light of a particular

λ across the whole range of the electromagnetic spectrum which is ultimately detected by linear variable filters [163], filter arrays [164–166] and the camera sensor [167]. The Liquid-Crystal Tunable Filters (LCTF) [166–168] use the same techniques found in LCDs to adjust their spectral transmittance [169]. The Figure 6.3 shows a diagram for

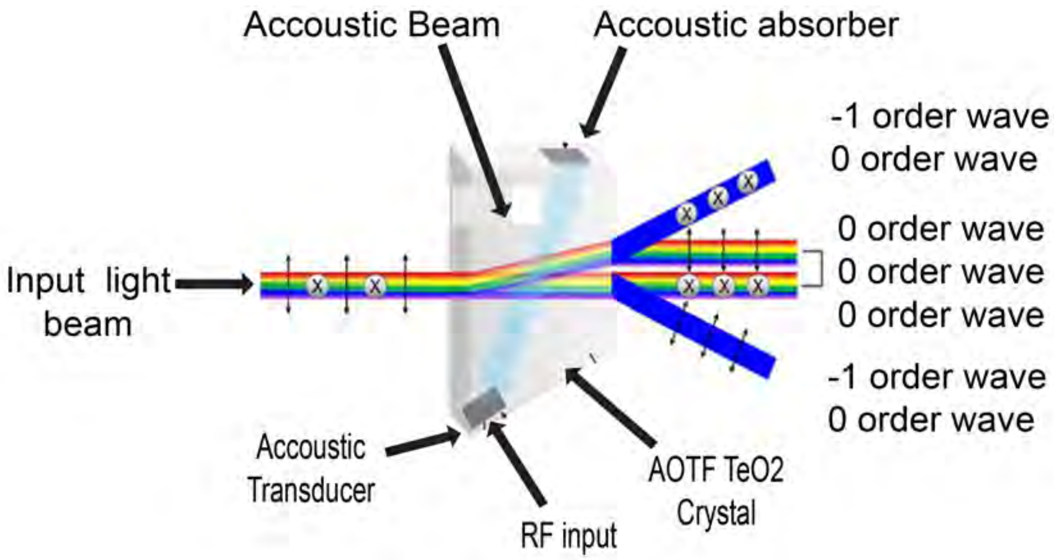

Figure 6.3: Illustration of an Opto-mechanics behind an Acoustic Optical Tuneable-Filter, In this filter a piezoelectric crystal alters the geometry of light slightly. The crystal is tuned in such a way that only a particular λ exits along the 0-order plane toward a monochromatic imaging sensor

AOTF mechanics. Since a hyperspectral scanning system first captures the scene, then scans across λ covering all the bands or channels, the hyperspectral data cube cannot be stored simultaneously [170]. An AOTF is one of the examples of a tunable filter [171]. A tunable filter camera uses a tunable electrical filter to perform the hyperspectral imaging and a modified image taken from reference [172] is shown in the figure 6.3.

6.4.3 Snapshot Hyperspectral Imaging Method

A Snapshot Hyperspectral Imaging System (HSI) or Non-Scanning imaging method acquires a simultaneous image of all the elements of the data-cube by taking multiple 2-D slices, i.e., 2-D detector arrays with a higher number of pixels which can again unite them into a data-cube. Figure 6.2 (c) shows the Snapshot Hyperspectral Imaging Method. The single-shot imager of Computer-Generated Holograms (CGH) is one of the examples to disperse light in snapshot HSI systems [173, 174]. They consist of cells of square pixels arranged in arrays to form a 2-D grating which assists a computed tomography imaging spectrometer (CTIS) to acquire spatial and spectral information in a single shot. Since this method does not involve any scanning, it is superior to use it in hyperspectral imaging where we motion artefact cannot be avoided, e.g., hyperspectral eye images. Snapshot HSI can capture each band for a single data-cube simultaneously, eliminating spatial and temporal misrepresentations. A snapshot image can be obtained using an integral field spectrometry with faceted mirrors [175, 176], coherent fibre, and lens-let arrays [177]. Hyperspectral imaging resembles real-time volumetric molecular imaging, in which a sample is illuminated with an x-ray pencil beam, and an energy-sensitive- detector is used for detection. The Computed Tomography Imaging Spectrometer (CTIS) [178], coded aperture snapshot spectral imager (CASSI) [179], multi-aperture filtered camera (MAFC), image mapping spectrometry (IMS) [180, 181] and the Snapshot Hyperspectral Imaging Fourier Transform (SHIFT) spectrometer [182–184] are the best examples of these types of systems. They are used for non-destructive examination in a variety of medical diagnostics [185] applications and its image may involve spectro- polarimetry and Computed Tomography (CT) together. For spectro polarimetric images all four Stokes parameters in a spectrum are encoded through modulation to find the spectral dependence. The spatial and spectral information are reassembled using Inverse Medical Computed Tomography (IMCT) mathematical techniques [186].

6.4.4 Spatio-Spectral Scanning Imaging Method

The Spatio-Spectral scanning imaging method takes advantage of both spatial and scanning imaging and put into practice for constituents situated at angled positions and difficult to image, using line scanning, spectral scanning, and snapshot scanning imaging methods. It produces a series of diagonal thin slices in a hyperspectral data cube. More accurately speaking, each image represents two dimensions in which one is λ coded. It combines partial advantages of spatial and spectral scanning and acquires the spectrum of a given sample using point scanning. A prototype Spatio-Spectral scanning system consists of a slit spectroscope at some suitable, non-zero distance before a camera, in which scanning each 2-D sensor output represents a λ=λ(y)-coded, spatial (x,y) map of the scene. An entire array of pinholes is used to project a series of projections onto the prism or grid. Each projection is used to make a rainbow-coloured strip which adds to the recorded 2-D image. The scanning process is accomplished through camera movement orthogonal to the slit or entire system can be displayed at a right angle to the slit, or a dispersive element can be placed just before a spatial scanning system. The Figure 6.2 (d) shows the spatio-spectral system image formation or scanned image. The remote sensing, with the idea of super-resolution, uses the Spatio-Spectral approach extensively [187–189]. Masia, F. et al. have presented the concept of sparse sampling for fast hyperspectral Coherent Anti-Stokes Raman scattering imaging while retaining the original spectral information. For a human osteosarcoma U_2OS cell, the hyperspectral imaging acquisition time was reduced by a factor of 25, and this method applies to hyperspectral imaging techniques with sequential spectral acquisition [190].

6.5 Coupling Optical-Modalities with HSFI

A hyperspectral imaging system can be combined with different imaging modalities to obtain the collective benefits of each imaging modality for disease diagnosis in cells and tissues. Combined Imaging techniques include confocal microscopy [191–195], polarimetric imaging [196–200], fundus cameras [201–204], Raman microscopy [205–209] and laparoscopy [210–212]. Investigations of the spectral properties of tissue become much easier after the fusion of HIS with above mentioned techniques in providing useful information. Fu, D. et al. fused a hyperspectral imaging system with stimulated Raman scattering by chirping femtosecond laser, and explored that the combination of fast spectroscopy and label-free chemical imaging enabled new applications in studying biological systems [213]. The combination of hyperspectral point-scanning microscope, a confocal microscope along with a point-scanning spectrometer (fluorescence light from the sample falls on the prism) before a linear detector array which has a high spectral resolution of 0.003 μm with the diffraction-limited spatial resolution and multiplex technology for live cell imaging [214, 215]. The fusion of a hyperspectral line-scanning microscope system and Image Spectrometer (IS) used a Powell lens for line-focusing of excitation light on the sample plane [216]. The same objective used for light collection creates an image on the entrance slit of the Image Spectrometer. A two dimensional detector array is used to capture the dispersed spectral components of the line image. There is an increase of the image data cube acquisition speed and spectral range from VIS to IR of the imaging system, but it affects the image contrast and spatial resolution due to the slit operation [2, 217–220]. Billecke, N. et al. did chemical imaging of lipid droplets in muscular tissues using hyperspectral coherent Raman microscopy, and correlated these signatures towards Obesity and pathogenic development of insulin resistance in type-2 diabetes. Label-free stratification of ectopic fat deposition and cellular organelle imaging becomes possible in fresh tissue sections with virtually no sample preparation [221]. Milos Miljkovic et al. developed a method based on a Raman label-free imaging method for human cells with less than a micrometre of spatial resolution. The Raman hyperspectral image is reconstructed by spectral contrast due to biochemical compositional changes, which provides further insight for the spatial information signature in a sample [222]. Francesco, M. et .al. improved the abilities of Hyperspectral Image Analysis (HIA) in combination with Coherent Anti-Raman Scattering (CARS), Stimulated Raman Scattering (SRS), and Spontaneous Raman Data (SRD) by reducing the spatial variation in the spectral error and speeding up sequential hyperspectral imaging to suppress motion artefacts. Xu J. et al. developed an ultra-broadband Hyperspectral Multiplex Coherent Anti-Stokes Raman Scattering (HM-CARS) system to perform chemo-selective histological imaging for stain-free clinical histopathology of clonal tissue samples. This system along with PCA can bypass many complicated histopathological procedures, providing a tissue fingerprint [223]. Vasefi, F. et al. developed a multimode dermoscope that can be used to map the distribution of specific skin molecules by combining polarization and hyperspectral imaging along with an efficient analytical model. It has matched physiological and anatomical expectations, confirming a technologic approach applied to next-generation dermo-scopes which appeal to dermatologists very well [224]. The Hyperspectral Imaging System coupled with fundus camera to acquire auto-fluorescence images of eye is the latest emerging technology, and is an important tool for non-invasive diagnosis of the eye disease [225, 226]. Roger, A. Schultz et al. developed a prototype hyperspectral imaging system capable of capturing the emission spectrum from a microscope optically coupled to an imaging spectrograph, with output recorded by a CCD camera; using the software it can reconstruct hyperspectral data samples relevant to cytogenetic, histologic and cell fusion [227]. Imaging spectrometers and fluorescence microscopy combine together in the form of a hyperspectral imaging system in which simultaneous capturing of typical biomolecular signatures is used for the location of emissions. There is a construction of spectral libraries for automatic analysis in successive acquisitions [228]. The small fields of view FOV's of the imaging system limit application, which can be replaced with large FOV by integration with confocal scanning microscope [229].

6.6 Hyperspectral Fluorescence Imaging System Comparison

In the chapter 2 we have discussed in detail the optical properties of biological tissues. Based on optical properties of biological tissue which are reflectance, fluorescence, and transmission the hyperspectral system can work in different measurement modes across the whole range of the electromagnetic spectrum. Most of HSI systems work on reflectance and in many cases, fluorescence and reflectance modes are coupled together to identify bimolecular signatures of various tumors [230]. In transmission mode, light is transmitted through tissue samples from a light source placed below the sample holder and collected by an imaging spectrograph placed above the sample [231]. In our laboratory, we have implemented the fluorescence mode along with EMCCD camera in an inverted microscope for hyperspectral fluorescence imaging of biological cells and tissues. In a hyperspectral imaging spectral resolution depends upon the number of channels in a given wavelength band, if there more channels in a given band the resolution will be more. Similarly the spatial resolution depends upon the camera used in hyperspectral imaging system. If camera has high spatial resolution hyperspectral system will be better in spatial resolution. Table 6.1 shows the comparison of different fluorescence and reflectance hyperspectral imaging systems along with spatial and spectral resolution.

6.7 Hyperspectral Image-Processing Methods

Image-processing methods make use of computer-based algorithms for the extraction, storage, and manipulation of information from hyperspectral image data. The extraction of relevant information make use of processing and data-mining techniques. Analysis, classification, regression, target detection, and pattern recognition are commonly used in data-mining and processing techniques [241]. The image obtained by the camera is stored in the system as a hypercube (M×N×λ). Here M is the number of rows, N the number of columns and λ the number of channels (for the hyperspectral image case it is more than three). The Spectral Control and Acquisition System (SCAS) written by the specific user can do specific hyperspectral application depending upon the capability of the code. Statistical information about the image is analysed in a histogram of pixel values [242]. The 3D hyperspectral data-cube usually store images in format Band Interleaved by Line (BIL), Band Sequential (BSQ) or Band Interleaved by Pixel (BIP). All of these file formats are known as ENVI, based on commercial software. Every file format has advantages and disadvantages for particular hyperspectral analysis, but BIL formats are most suitable to the majority of hyperspectral image- processing tasks. There are many spectroscopic, chemometric analysis, and machine-learning tools such as Principal Component Analysis (PCA) and Partial Least Squares Regression Analysis (PLSRA) which can provide real-time detection of multiple constituents and can be used to process the spectral information within the hyperspectral image. The hyperspectral image workflow consists of image acquirement, calibration, Spectral-Spatial Pre-processing, and reduction of dimensions, and detection of a specific target.

6.7.1 Hyperspectral Image Analysis

A medical hyperspectral data cube contain much diagnostic information extracted at the level of tissue, cells, and molecules. All spectral and spatial information present in the hyperspectral data cube has a crucial importance for disease screening, diagnosis, and treatment. The hyperspectral data-sets use advanced image-classification methods for extraction, unmixing, and classification of relevant spectral information from the data of the captured image [243]. The goal is to relate these molecular signatures with the state of the specific disease by decomposing mixtures of spectral and spatial information spectra into intrinsic molecular components. Hyperspectral image analysis, in the field of remote sensing has made much progress, but there is less improvement of hyperspectral image-analysis methods in the clinic. The hyperspectral image consists of many objects with different spectral properties, and not every pixel in the image represents a single fluorophore but may be a combination or mixture of various spectra. The complexity of this mixing depends upon the spatial resolution of the system, what type of fluorophores are present in the image, and the distance of the image formation from the camera [244]. A hyperspectral imaging system must have enough spatial resolution relative to the number of target endmembers so that the abundance of each target end-member within a given pixel makes it possible to implement he extraction techniques [245, 246]. The image pre-processing, feature extraction/selection, and classification are the fundamental step involved in HSI analysis.

6.7.2 Hyperspectral Image Pre-Processing Methods

Hyperspectral image pre-processing methods aim to display image information more clearly and pre-processing is used to process the image in spatial as well as spectral domains. Noise reduction, image segmentation (Selection of ROI by masking the image areas) [247–250], image smoothness, flattening, normalisation, baseline correction and compression of image data are used in image pre-processing. Background masking also called binarization, uses factor analysis or PCA methods [251], and is just like choosing a sample from some population in statistics [252]. Spatial pre-processing can affect the spectral signature so that it is usually not applied to calibrated images or raw data. Spatial post-processing is commonly used for interpretation, manipulation and pattern recognition for ordinary images. Specific features that exist in signal in the time domain are extracted using appropriate filters in the frequency domain [253]. Spectral features like spectral shape and peak width can be obtained using the differentiation tool (first and second order derivative tests) and baseline corrections [254, 255]. Tsai, F. et al. used differentiation analysis of hyperspectral data for detecting spectral features, and extracted subtle information at different spectral scales of interest [256]. In spectral pre-processing of hyperspectral images, endmembers can be extracted using the spectral library of intrinsic signatures. Pixel Purity Index (PPI) and N-finder algorithms require pre-processing methods such as spectral unmixing, target detection and classification before their implementation [141]. Maider Vidal et al. showed that the removal of noise, dead pixels, spiked points, and data compression from the hyperspectral image are a prerequisite for image analysis [257]. Estimation of abundance in unmixing is similar to concentration in PLS regression. Robert Korprowski et al. proposed a method which subdivides spectral image processing into three steps: reading image from the data file, matrix conversion of raw data and preliminary image analysis, and provided the solution to extract the selected features from the massive data image in the MAT-LAB platform [258]. Image segmentation is necessary with a medical hyperspectral fluorescence image and can be done either manually or automatically [259, 260]. Both spatial and spectral pre-processing techniques can be fused together under an integrated processing algorithm or unified mathematical framework [261]. One researcher used crossed information in composite kernel methods by the fusion of spatial and spectral pre-processing methods integrally for the classification, segmentation and unmixing of the hyperspectral image data. Mendoza et al. extracted both spatial topological and spectral latent variables in image segmentation using a butterfly approach [262]. Data-Driven Markov Chain Monte Carlo (DDMCMC) used the computer simulation for image segmentation which operates in the Bayesian statistical unification the framework in which many segmentation algorithms play roles such as edge detection, clustering, region growing, split-merge, snake/balloon, and region competition [263]. Fu, D. et al. used a cell-segmentation method based on spectral phasor analysis of hyperspectral stimulated Raman scattering image data. They combine the technique with the branch-bound algorithm for optimal unsupervised segmentation selection of cellular organelles of mammalian cells [264]. Gabriel, Martin, Antonio, and Plaza et al. developed a pre-processing method after fusion of spatial and spectral information. Spatially homogeneous and spectrally pure pixels are used from each cluster in image analysis before end-member identification and spectral unmixing [265].

6.7.3 Feature Extraction and Selection Methods

Hyperspectral images have a lot of redundant information in both spectral and spatial domains. Feature extraction is a linear or nonlinear transformation that reduces the data redundancy by transforming it into a new lower-dimension space, so there should be efficient and accurate extraction of diagnostic information from the data-set. General feature extraction methods include PCA [266], PLS [267] , Kernel PCA [268] and a Linear Discriminant Analyser (LDA). All of the above methods preserve the information necessary for the application under consideration, for example, classification and detection minimising the classification error. A detailed explanation of the PCA steps used for medical hyperspectral images was presented by Guolan, Lu. and Baowei, Fei. [226]. Other PCA techniques include Independent Component Analysis (ICA) [269] and Minimum Noise Fraction MNF [270]. The relative distributions of molecular component mixtures, identification of vital discriminative features, and estimation of spectrum in the spectroscopic data are possibly using these PCA-based methods. Unlike the extraction technique, the feature-selection method does not require low- dimensional space. In this extraction method well-known algorithms (branch and bound [271], greedy hill climbing [272], exhaustive search [273], floating search methods [274–276], bidirectional search [277], projection pursuit) [278, 279] are used to find the optimized solution from the given hyperspectral image data. In bioinformatics, its use is for contents and micro-array analysis. Its objective function is subdivided into three methods: filters, wrapper, and embedded. Every technique has specific advantages and disadvantage for a given application [280]. Mehmet Fatihakay analysed the Wisconsin Breast Cancer Data-set (WBCD) using a combination of SVM and a feature selection method without compromising classification accuracy or sensitivity; specificity and classification accuracy was found to be 99.51% for s SVM model that contains five features [281].

6.8 Hyperspectral Data Classification

Classification methods applied for most hyperspectral medical imaging include pixel and subpixel methods. The (mostly supervised) classification methods include Support Vector Machines (SVMs) [282], Artificial Neural Networks (ANN) [283], Spectral Information Divergence (SID) [284], and Spectral Angle Mapper (SAM) [285].

6.8.1 Support Vector Machines

The SVM algorithm is a kernel-based machine-learning technique, commonly used in hyperspectral-image data classification and relying on statistical learning theory that separates the linearly separable feature space with maximum margin into classes [286]. A non-linear SVM having a higher-dimensional feature space can be used along with slack variables in case the feature space is not linearly separable. They are less sensitive to the curse of dimensionality, so are used for universal classification solutions. The disadvantage of SVMs includes the trial-and-error based method of finding the best kernel function for a given problem. Therefore, non-linear SVMs can be used in combination with feature-extraction methods to make an effective framework for classification and regression analysis, such as kernel- PCA, kernel discriminant analysis [287] and LDA-SVM [288]. Masood, K. et al. used SVM algorithms for Hyperspectral Texture Analysis (HTA) for colon tissue biopsy classification [289]. Kong et al. used support vector machine analysis for hyperspectral fluorescence imaging data analysis to detect skin tumours, in which hyperspectral images were obtained on 21 channels with λ=440-640 nm [290]. SVMs along with feature-selection techniques were used to detect breast cancer [291, 292], classification and validation of cancerous tissue [293], gene selection to detect cancer [294], bladder cancer recognition [295]. In Raman hyperspectral imaging SVMs are used for prostate cancer detection hyperspectral imaging [296].

6.8.2 Artificial Neural Networks

An Artificial Neural network (ANN) is a classification method whose implementation on the hyperspectral image depends on the information acquired from different sensors, the parameters used to obtain an image, the nature of the pixel information and the number of outputs generated for each spatial element of data [297, 298]. The Convolutional Neural Networks (CNNs) are used for a feature-learning approach for the classification of hyperspectral images. They provide information about the structured features, spectral band-pass filters resemblance, using the direct input of hyperspectral data [299]. Qian Wang et al. developed an identification method combining both spectral and spatial features and an SVM recursive feature to differentiate lymphoblasts from lymphocytes. The Marker-based ANN learning vector quantisation was proposed to perform identification with the integrated features [300]. Romuald Jolivot et al. used an ANN based algorithm to construct a hyperspectral data-cube from multi-spectral image data, which can improve diagnosis of skin cancer and inflammatory diseases [301]. Frederic Ratle et.al. proposed a semi-supervised framework of ANN and a bendable embedding regularizer for the classification of unlabelled samples. The classification accuracy and scalability for hyperspectral image improved and the system can handle millions of specimens in remote sensing [302].

6.8.3 Data Unmixing Models

Linear Spectral Unmixing (LSU) is a fundamental method for data analysis [303]. Its underlying assumption is that observed spectra should be a linear combination of all the constituents spectra, called end-members. The linear combination consists of concentrations of fluorophores, absorption and reflectance coefficients. In fluorescence hyperspectral imaging method tissue or cell image signatures are linear combinations of the fluorophores and they can be expressed in an equation

$$A_p = Xf + r = \sum_{i=1}^{N} X_i f_i + r \tag{6.1}$$

Here is the observed spectrum, f is the abundance coefficient vector, N the number of end-member spectra of X, r is the residual or noise, and can be found in the literature [304]. Linear spectral unmixing may be supervised or unsupervised whether X is known or not [236]. If there is no noise r and there are M materials present in the unknown sample, there should be M vertices of the hull in (M-1)-dimensional space. If there are four materials A, B, C and D present in the spectrum, the tetrahedron should show four vertices for the pure constituents in three-dimensional space. A convex hull showing vertices A, B, C and D is shown in the Figure 6.4 below. Similarly, for three pure constituents, a two-dimensional triangle exists having three vertices [305, 306]. A straightforward geometrical interpretation to find end-members is that the spectra of all individual pixels represent a specific cluster in an N-dimensional space. The cluster contained within a convex hull is called a simplex, and each pixel spectrum point within this simplex represents a linear combination of the spectra presented on the vertices of that simplex. Errors are typically between 5-10%. According to Liang Gao.et al.

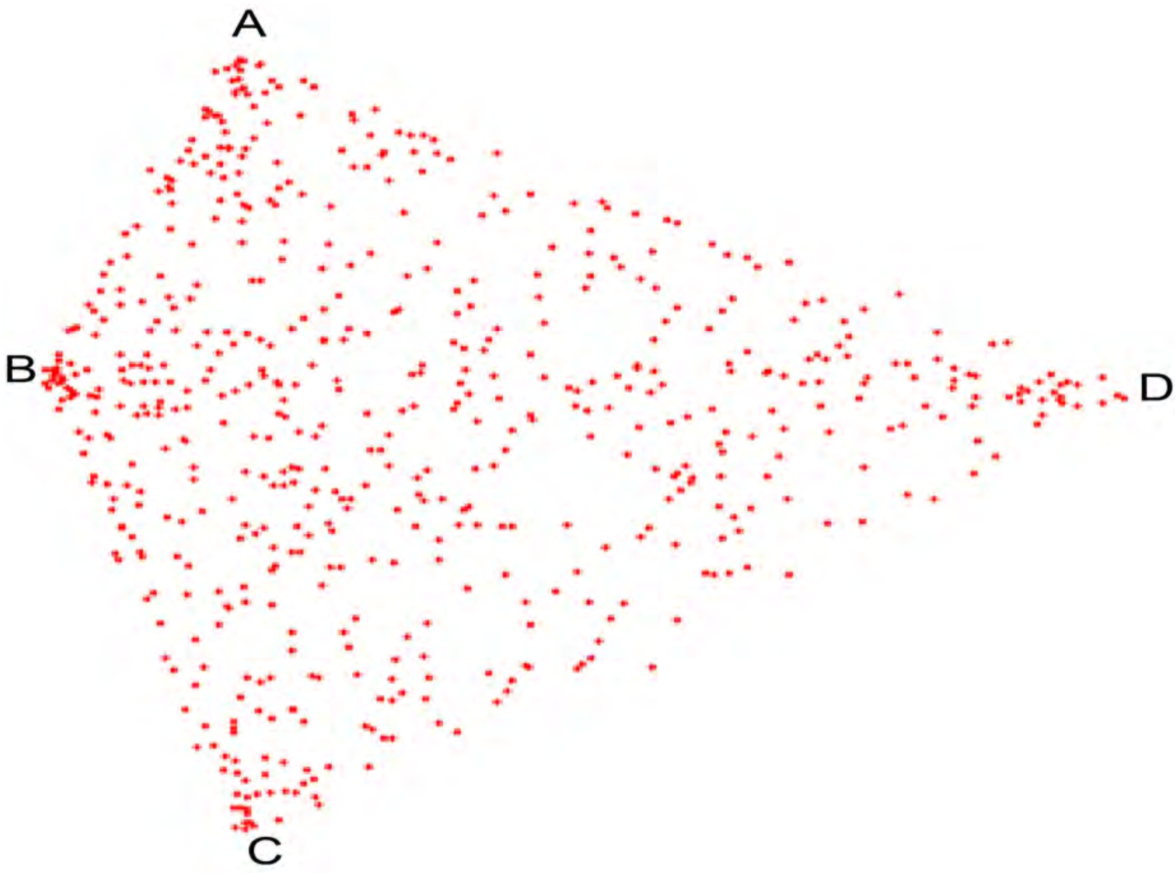

Figure 6.4: A convex hull showing four vertices

LSU contains a hyperspectral measurement matrix X having dimension $M \times P$, here P image pixels and M spectral bands. In Linear Spectral Unmixing (LSU), X denotes a linear combination of the fundamental elements given by the following equation [307].

$$X = SC + R \tag{6.2}$$

S is the spectral constituent matrix having dimension $M \times K$, C is the chromophore concentration $K \times P$ matrix, and R is the additive noise matrix. For supervised unmixing, the equation is

$$C^{\star} = S^{\ddagger}X \tag{6.3}$$

is an estimation of C* and the Moore-Penrose pseudo-inverse of matrix $S^{\ddagger}$. The rank of the matrix C and the spectral-component matrix $S \geq$ postulated chromophores. It has two advantages:

1. The hyperspectral imaging permits a general experimental procedure for imaging a diversity of chromophore mixtures with no change of filters.

2. It expedites the unsupervised Linear Spectral Unmixing.

For the formation matrix S, supervised LSU requires accurate and up-to-date information of the emission and reflection spectra of biomarkers and database. For in-vivo tissue measurements, prior knowledge of the emission and reflection spectra is challenging to obtain or sometime not reliable for use, e.g. when the experimental chromophore spectra show unrepeatable results or biological variations, supervised spectral unmixing become inapplicable. Under such situations, HSFI become necessary for the collection of spectral samples to estimate spatial and spectral components [308, 309], green, yellow, and red are used for normal, precancerous, and cancerous fibroblast nuclei respectively.

6.9 HSFI Application in Optical Diagnostic

A hyperspectral imaging system along with software analysis tools is used for the diagnosis of a variety of malignant diseases. Almost all types of cancers e.g. (breast cancer [310], head and neck cancer [311] , colon cancer [312], skin cancer [219, 313]), (crime-scene investigations and age estimation [314, 314]. Gastric cancer [219, 315–317], cervical cancer [318, 319], ovarian cancer [320, 321], oesophageal cancer, brain cancer [322], colorectal cancer [323], and cancer metastasis [324], are diagnosed using different hyperspectral acquisition methods, and the heart and circulatory pathology, retinal diseases, diabetes, haemorrhagic shock by taking real-time images using label-free tissues and cells. Beule P. et al. used hyperspectral fluorescence lifetime imaging with an optically sectioned whole-field for label-free biological tissues [325]. Bjorgan, A. et al. developed a hyperspectral imaging system to estimate optical parameters of skin for real-time tissue diagnostic [326]. Cancio, L.C. et al. proved that HSI is an innovative approach to diagnose haemorrhagic shock [327]. Cassidy, R. J. et al. analysed hyperspectral colon-tissue images using vocal-synthesis models. [328]. Wang, C. et al. introduced a hyperspectral imaging method for detection and quantitative analysis of cervical neoplasia for the comparison with clinical findings to assess the accuracy and efficacy of the process [329]. Martin, E. Gosnell et al. did hyperspectral autofluorescence imaging of neurosphere-derived cells to investigate neuro-degenerative diseases from olfactory patient mitochondrial MELAS (myopathy, encephalomyopathy, lactic acidosis, stroke-like syndrome). cellular maps of the native fluorophores, free and bound NADH, flavin, and retinoid revealed subtle subpopulation metabolic signatures. We now present some of the novel hyperspectral images techniques for disease diagnosis.

6.9.1 Breast Cancer

Due to the massive time consumption in the standard diagnosis of an image pattern by a professional radiologist, automated classifiers process the diagnosis in mammography, saving time without any cost of accuracy in distinguishing benign and malignant tumours. Figure 6.5 is taken and modified from refrence [330] shows the image differentiation enhancement after Artificial Neural Network (ANN) processing. ANN plays

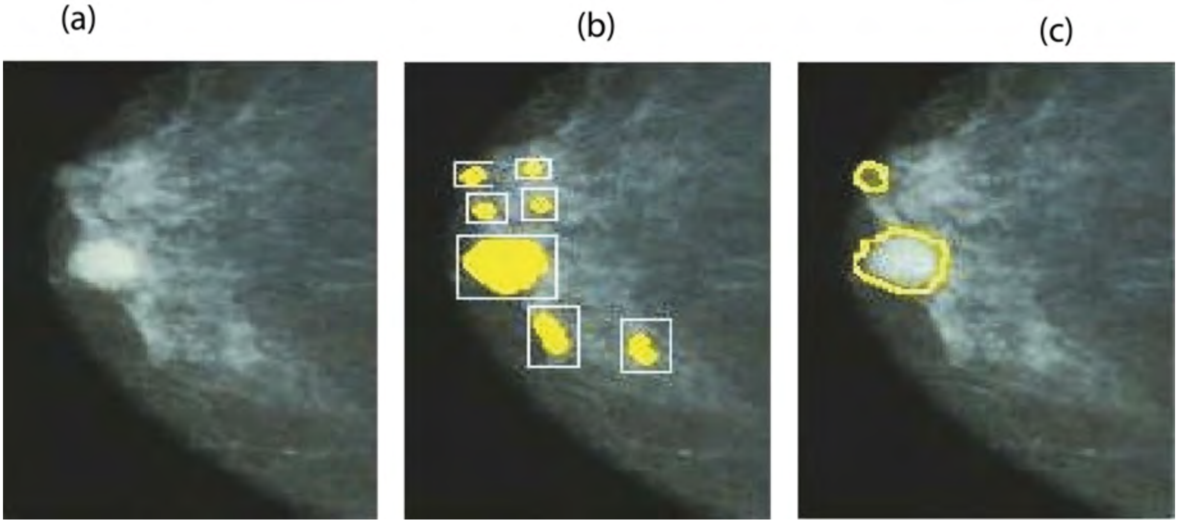

Figure 6.5: Results (a-c) original image, Image after ANN processing, and image after ANN processing along with Gabor wavelets as input

a vital role to diagnose breast cancer. Much less data is available for these detection techniques concerning specificity and sensitivity. Support Vector Machine (SVM) decision tree and ANN are frequently used classifications to detect breast cancer at the early stages by statistics. Emad, A. Mohammed et.al implemented Fine Needle Aspirate (FNA) technology and analysed the data using new Ordered Weighted Averaging (OWA) operator for early diagnosis of cancer with 99.71% accuracy [331].

6.9.2 Cellular Differentiation Using Hyperspectral Imaging

Hyperspectral images along with algorithms can be used to distinguish normal, precancerous, and cancerous cells. The figure 6.6 is taken and modified from reference [332] shows left and right image comparisons based on spectral libraries. Comparison of normal human fibroblast, as well as its telomerised and SV 40-transformed derivatives, have been made using the standard algorithm. Gaudi, S. et al. explained that hyperspectral imaging of melanocytic lesions allows the identification of objects through their unique spectral signatures. Further investigation of HSI in classifying a neoplasm is encouraged [333]. Guolan, L. et al. drew tumour margins in an animal study during surgical resections which always remained a challenging task [334]. Hattery, D. et al. created a blood volume and obtained blood oxygenation hyperspectral images using a multilayered tissue model used for patient treatment monitoring [335]. Amicia, D. Elliott et al. did real-time hyperspectral snapshot fluorescence imaging of pancreatic b-cell dynamics in combination with an image-mapping spectrometer (IMS), and their device can acquire real-time signals from multiple fluorophores with high collection efficiency of 65% and an image acquisition rate 7.2 fps. The figure 6.7 which is taken and modified from [336] shows how they reconstructed He-La cell images using their protocol. Kester, R. et al. put forward an image-mapping spectrometry introducing a new snapshot hyperspectral imaging platform for a variety of applications starting from remote sensing, to surveillance, and live-cell microscopy to medical diagnostics [337]. It facilitates the capturing and identification of the different spectral signatures present in an optical field during a single-pass evaluation, including molecules with overlapping but distinct emission spectra.

6.9.3 Fundus Camera and Hyperspectral Imagining

Gao, L.et al. did hyperspectral images of the eye at λ=470-650 nm wavelengths to reveal minute eye differences. This optical technique can perform real-time imaging of oxygen saturation dynamics with a sub-second temporal resolution [338]. Sunni, R. Patel et al. measured the retinal reflectance of arterioles and venules using a prototype hyperspectral retinal camera repeatedly, giving hope for correct retinal-oxygen saturation values in future imaging [339]. D.C. Gray et al. made use of the advantages

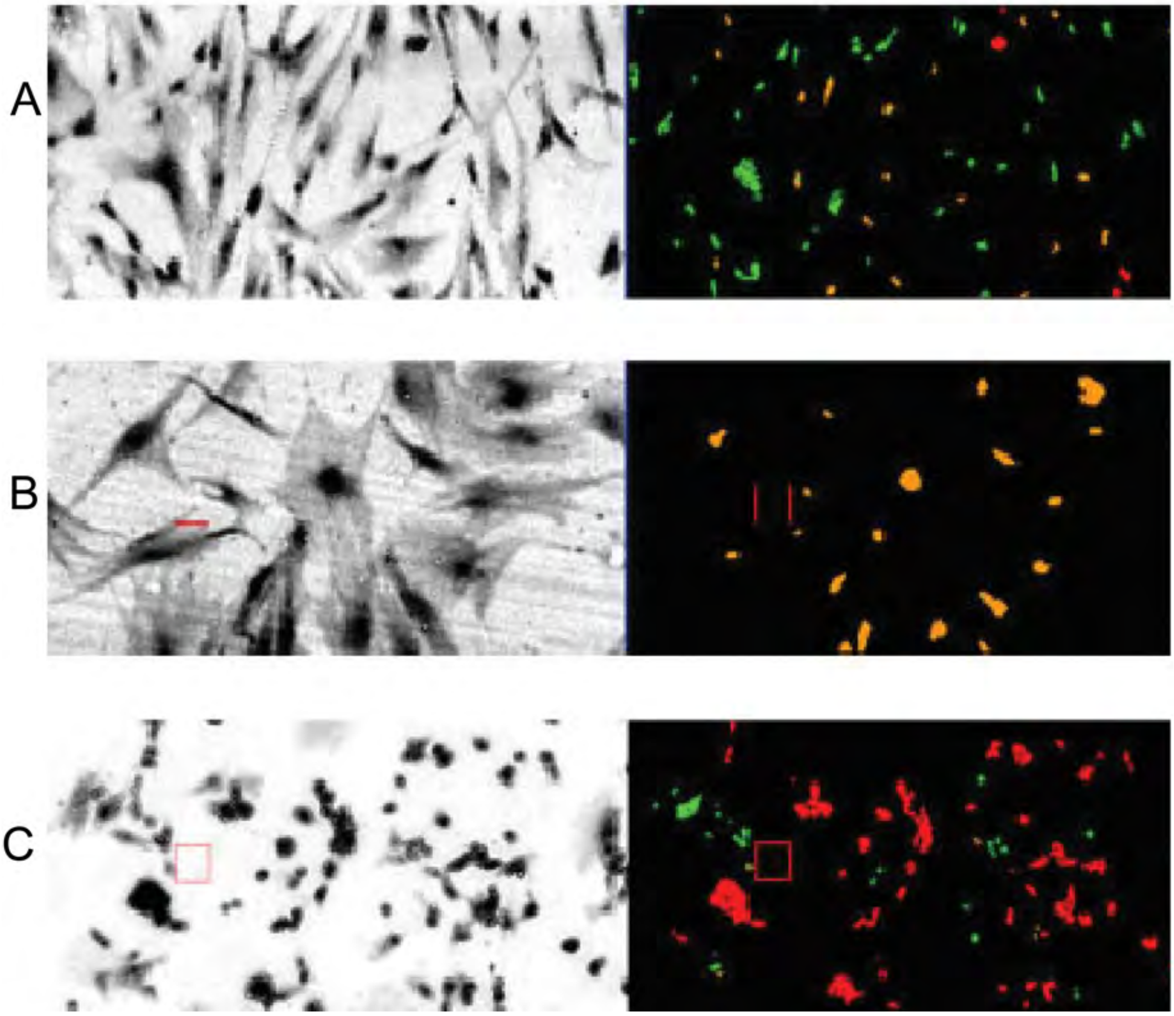

Figure 6.6: (A) Corrected hyperspectral image of normal fibroblasts and algorithm-based nuclear classification on the left and right respectively; (B) Corrected hyperspectral image of precancerous fibroblasts and their algorithm-based nuclear classification on the on the left and right respectively; (C) Corrected hyperspectral image of cancerous fibroblasts and their algorithm-based nuclear classification on the left and right respectively Note: Green, yellow and red are used for normal, precancerous and cancerous fibroblast nuclei respectively

of multi-spectral, adaptive optics and confocal fluorescence imaging to resolve single cells in healthy and diseased retina. The figure 6.8 is taken and modified from reference [340] shows the images and their resolution at the different wavelengths. Julia Schweizer et al. diagnosed age-related macular degeneration in the eye; they acquired and analysed hyperspectral images to detect the oxidative state of cytochrome-C in real time [341]. Measuring biochemical status without additional biochemical markers

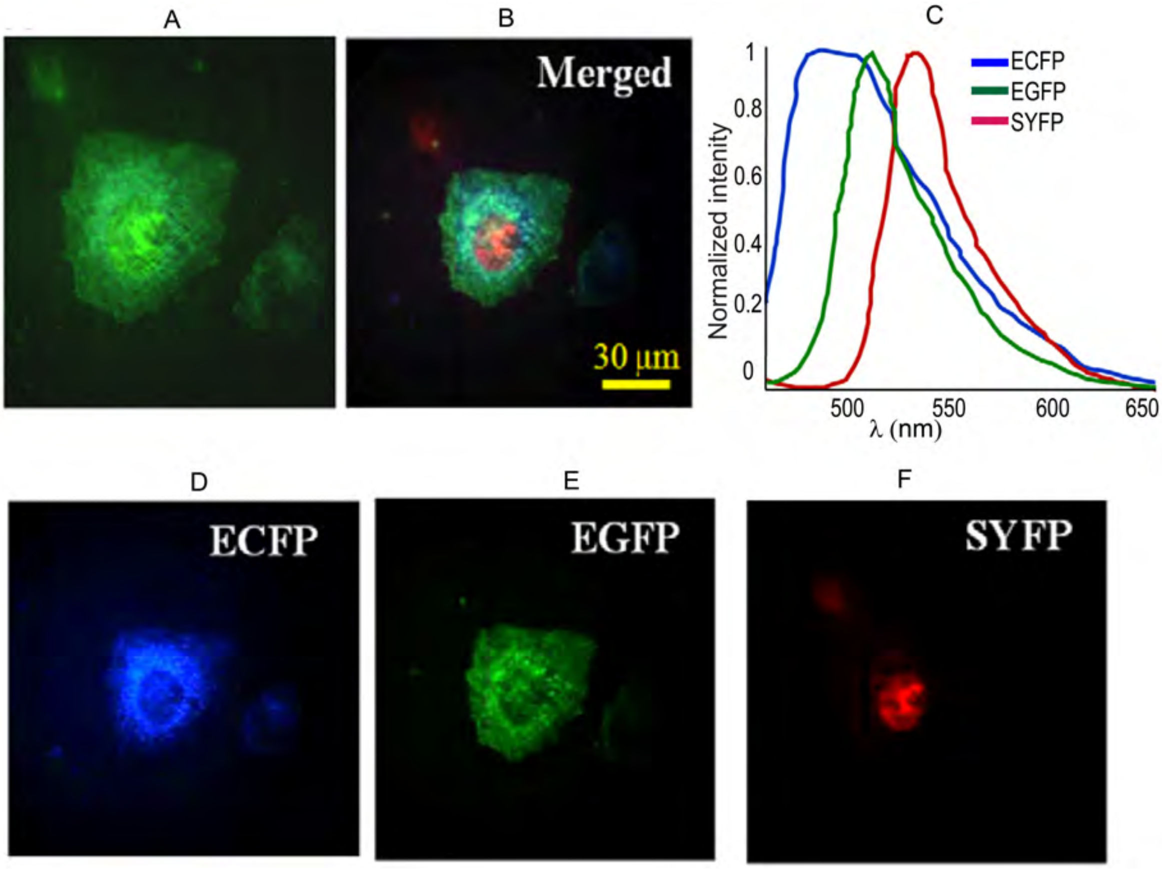

Figure 6.7: Triple-labelled He-La cells and spectral unmixing in ECFP, EGFP and SYFP; (A) The reference image was taken by a colour camera directly at a microscope slide; (B) D, E and F are the images obtained after merging; (D-F) Pseudo-coloured images of the unmixed component in a linear unmixing algorithm on am Image mapping spectrometer (IMS) measured data-cube. The spectral-component images indicate subcellular localisations of the FPs

in-vitro is possible using the developed system. It has been applied in ophthalmology to detect macular degeneration in the eye [342], oxygen saturation and diabetic retinopathy applications [343].

6.9.4 Lung Cancer Detection

Silas, J. Leavesley et al. did hyperspectral imaging microscopy for identification and quantitative analysis of fluorescently labeled cells in highly autofluorescent tissues.Su, M.et al. fused HIS data with Foliage-Penetration Synthetic Aperture-Radar (FOPEN SAR) data which can enhance overall detection and classification performance [344].

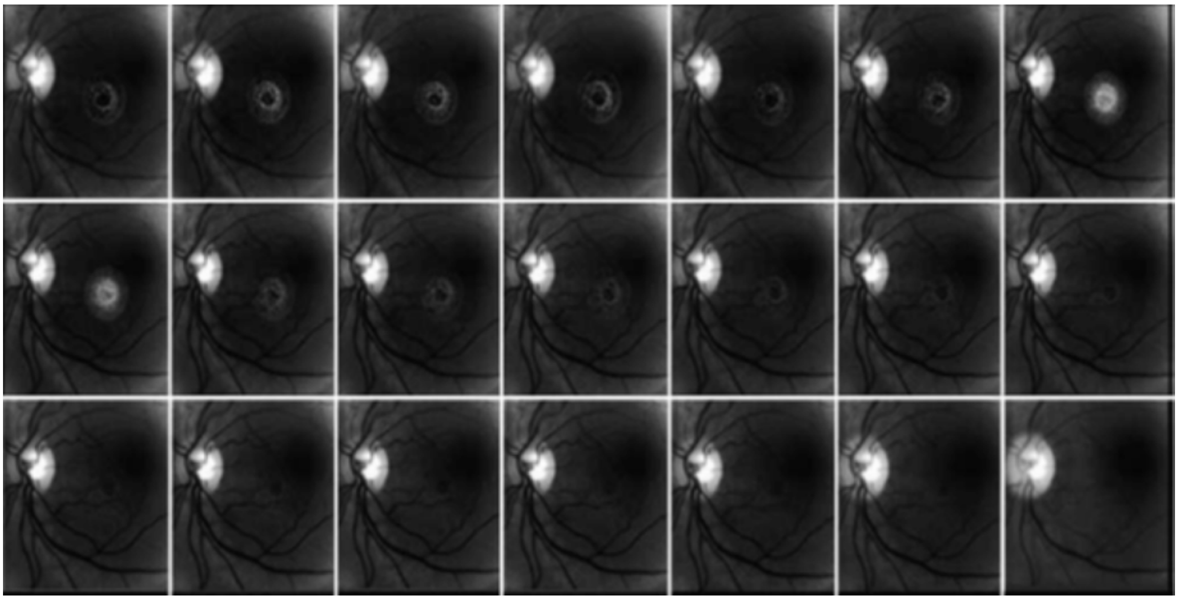

Figure 6.8: Typical images taken by the HRC to create a hyperspectral cube of retinal images between 500 and 600 nm at 5 nm intervals with an exposure time of 80 ms

Eung, S.H. et al. made hyperspectral fluorescence imaging of cellular iron for in vitro model of Parkinson disease and said that the diagnosis application might expand to various neurological disorders involving alkalis and alkaline metals in the body.

6.10 Discussion

Medical hyperspectral fluorescence imaging (MHFI) technology is a methodology which can solve our complex medical problems more efficiently and precisely. Medical Fluorescence Hyperspectral Imaging (MHFI) is used in image analysis for visualizing the chemical composition of the compartments in the body of the living organisms. MHFI is also used to keep an eye on tissue oxygenation and blood volume during surgery to provide real-time data continuously during surgical procedures [345, 346].The optical penetration depth is inversely proportional to λ and cannot penetrate deep into tissue, which limits the application of HFI. The optical penetration depth of light in the tissue is 0.0357 cm at λ=850 nm and 0.048 cm at λ=550 nm respectively. This penetration depth limitation can be avoided by using reflectance hyperspectral images. Snapshot hyperspectral imaging facilities have much usage where there is a possibility of motion artefacts, and data analysis can be made using latest data cube formats like vortex data analysis in MATLAB using the latest Math-Work-Simulink facilities. Fluorescence and reflectance based hyperspectral imaging methodology have been used successively to probe and diagnose tissues with a healthy and diseased state. Still, there is much research remaining in hyperspectral imaging on a molecular level. To investigate the fusion of a hyperspectral imaging system with Raman spectroscopy is s a better choice. So Raman hyperspectral imaging in combination with HSFI, or in some cases unification of CARS, also provides insight into the molecular level. The spectral libraries of tissues, cells, and molecules signatures should be up-to-date, so that this database should be used effectively for various disease diagnosis and treatment. Furthermore, advanced data-mining and classification methods are still essential to fully utilise the plentiful spectral and spatial marks of the constituents in hyperspectral images.

6.11 Conclusion

Hyperspectral imaging methods obtain a 3-D hyperspectral image data-cube, having spatial and spectral dimensions. All of the four data-acquisition and imaging techniques are fully described along with the latest research. As an emerging imaging technology, Hyperspectral Imaging applications exist from research to medical trials. Fusion of HSFI with other imaging modalities, including Raman scattering, confocal microscopy, the fundus camera and PET scanning, results in acquiring more useful data. Analysis of hyperspectral data with the latest unmixing and classification algorithms is detecting changes in cells at the molecular level and diagnosing malignant disease at early stages with astonishing results. The combination of research results along with clinical trials provides an excellent potential in improving the hyperspectral imaging modalities to produce reliable and accurate results in terms of diagnostics, monitoring and tumour marking during surgical procedures. The spectral libraries including the latest research discoveries can improve the supervised unmixing techniques. In unsupervised unmixing new advanced classification algorithms like the combination of support vector machines and artificial neural networks are promoting. Snapshot hyperspectral imaging along with vortex analysis has made Hyperspectral Imaging much fast in processing.

Table 6.1: Comparison of hyperspectral fluoresence imaging techniques

Hyperspectral imaging Techniques	Spectral range (nm)	Resolution	Applications	Ref.
Hyperspectral (Fluorescence and Reflectance) Imaging	200-700	~5 μm/pixel	Cervical neoplasia	[232]
Hyperspectral (Fluorescence and Reflectance) Imaging	330-480	5 μm/pixel	Cervical cancer	[233]
Hyperspectral fluorescence Imaging System 3D	400-1000	3 nm	Invivo optical imaging	[234]
Hyperspectral fluorescence imaging (Author used in lab)	450-700	0.9 μm/pixel	Cellular Diagnostics Application	[235–237]
Hyperspectral Fluorescence Imaging	440-640	10 nm	Mouse Skin Tumor Detection	[238]
Parallel Scan Hyperspectral Fluorescence Imaging	632.8,473	Spectral 0.2 nm , Spatial 2-30 μm	Fluorescent Dyes Cy5 and Dylight 680	[239]
Fluorescence Hyperspectral Imaging	580-920	3.0 nm	Fluorescent Dyes	[240]

7

Auto-Fluorescence Quenching Quantification of NADH (Manuscript V)

7.1 Fluoroscopic Data Acquisition Instruments

A spectro-photometer is an instrument used to measure the intensity of light across a wavelength (λ) in a spectrum. It can be used to measure the excitation and emission spectra of materials under investigation. Figure 7.1 (a) shows the schematic diagram of a spectro-photometer. The light source, excitation monochromator, sample housing, emission monochromator, and detector are the main component of any fluorescence measurement setup. The Continuous Wavelength (CW) λ source produces light of all wavelengths and a monochromator selects wavelength used to illuminates the sample. The emission filter is used to collect the fluorescence light from the sample at a right angle to the incident beam and finally detector gives the fluorescence signal. In next, section we will explain the fluorometer components and their functions in detail. The light source shown in the figure can be a Xenon arc lamp, a high-pressure mercury lamp, a quartz-tungsten halogen lamp or a solid state light source like LED or a laser. Among these light sources Mercury arc lamp is the one which emits high-intensity

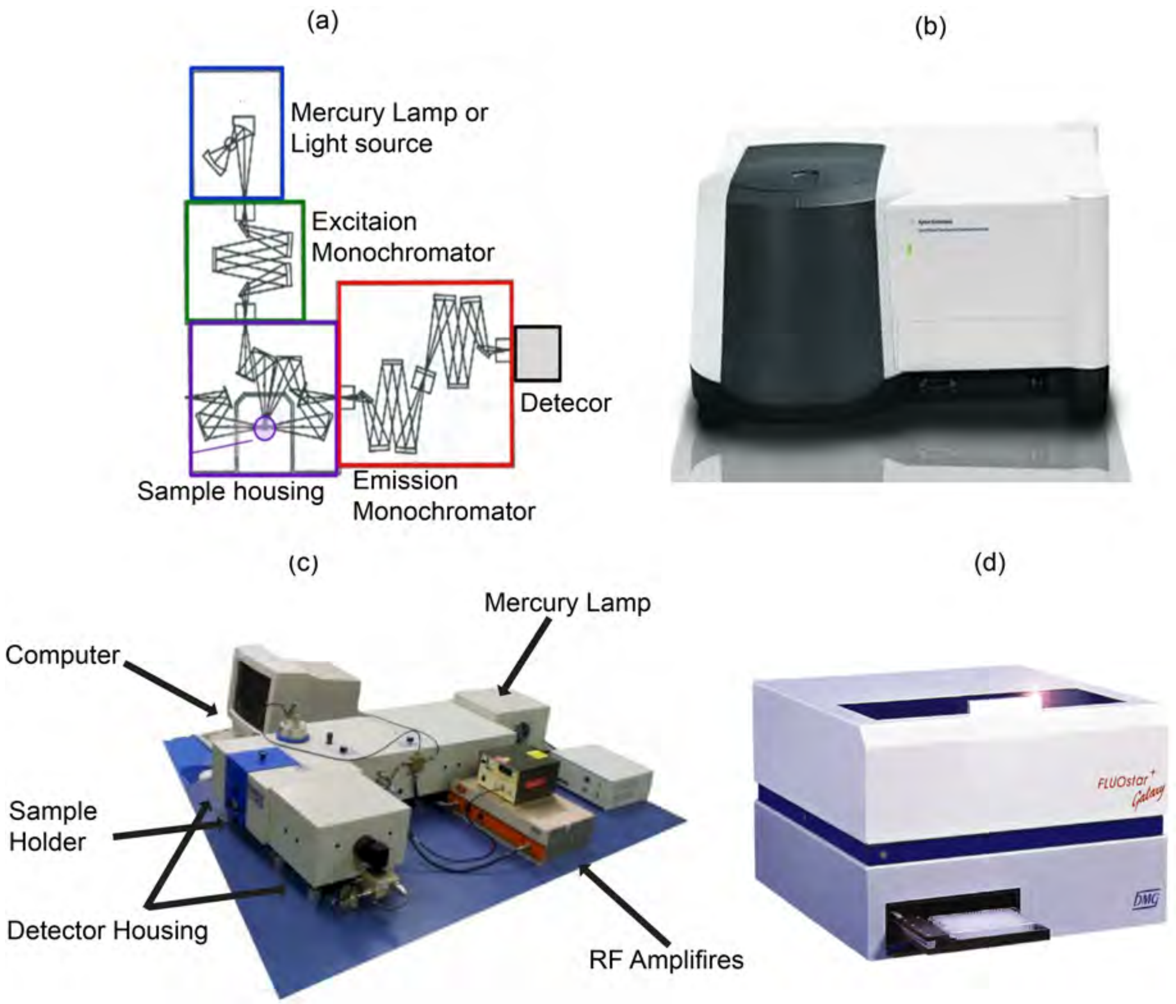

Figure 7.1: (a) Schematic diagram for fluorescence spectro-photometer (b) Cary Eclipse fluorescence spectro-photometer used for In-vitro for experimental measurement (c) Different components of Fluoro-log Tau-3 system (d) Fluoro-star Galxy photo-spectrometre to read fluorescence data from micro-plates

light over a broad range of wavelengths covering UV to near IR region. This broad-band light spectrum consists of many wavelengths which can be separated using a monochromator. The monochromator makes use of basic filters, a diffraction grating for wavelength selection and is designed to have a high efficiency and sensitivity. The detector consists of a photomultiplier tube (PMT) to detect the fluorescence signal over a wide range of λ's with high sensitivity and gain. Most of the spectro-photometer available now use a PMT as the detector and even it can detect single photon also. In our experiments, we used Fluorolog Tau-3 for auto-fluorescence measurement it is shown in figure 7.1 (c) with its components. We used it for auto-fluorescence signal measurements of He-La cell suspension targeting NADH emission spectra. We excited the He-La cell suspension at λ=340 nm and emission collected from λ=400-650 nm. The Cary Eclipse Fluorescence spectrometer is simple and capable of collecting the light from four different modes. These are fluorescence, phosphorescence, bioluminescence, and time-resolved phosphorescence. But the sensitivity of Cary Eclipse spectrometre is lower as compared to Fluorolog Tau-3 system, therefore, we used it for In-vitro fluorescence measurements and to acquire the in-vitro data of NADH for EEM. It is shown in the figure 7.1 (b).

7.2 Motivation for Auto-fluorescence Quenching Quantification

NADH is a coenzyme which plays an important role in energy metabolism, mitochondrial functions, oxidative stress generation, and cell death [347]. So NADH fluorescence quenching can tell us about the state of the cell which can be used in cellular diagnosis. In this work, we performed in-vitro and in-vivo fluorescence quenching quantification experiment of free and bound NADH in He-La cell line model.

7.3 Author's Contribution to Manuscript V

Being the principal author of this paper, the Ph.D. candidate (Aziz ul Rehman) has discussed an idea of fluorescence quenching with principal supervisor Ewa M. Goldys. This work has generated two articles, one article having the title Fluorescence quenching of free and bound NADH in He-La cells determined by hyperspectral imaging and unmixing of cell autofluorescence has been published in Biomedical Optics Express and the second article is ready for submission. For the second manuscript having the title, Auto-Fluorescence Quenching Quantification of Free and Bound NADH In He-La Cell Line Model, principal author acquired preliminary data for in-vitro results of NADH and FCCP quenching on Cary Eclipse Fluorescence spectrometer. Idea worked very well, so we have extended this in-vitro work towards cellular studies for He-La cell line. Second author Ayad G. Anwer involved in the rest of the experimental work for cellular fluorescence quenching studies in He-La cell line model. We did red to green ratio experiment for mitochondrial membrane potential. The Manuscript has been written by Aziz ul Rehman and Prof. Ewa M. Goldys checked it and highlighted the shortcoming.

7.4 Manuscript V

Aziz ul Rehman, Ayad G. Anwer, and Ewa M. Goldys, Auto-Fluorescence Quenching Quantification of Free and Bound NADH In He-La Cell Line Model (Ready for submission)

7.5 Auto-Fluorescence Quenching Quantification of NADH In He-La Cell Line Model

Aziz ul Rehman[1,2,3], Ayad G. Anwer[1,2], and Ewa M. Goldys[1,2]

[1]Department of Physics and Astronomy Macquarie University, Sydney, 2109, New South Wales, Australia

[2]ARC Centre of Excellence in Nano-scale Bio-photonics, Macquarie University, Sydney, 2109, New South Wales, Australia

[3]Biophotonics Laboratory, National Institute of Lasers & Optronics, Lehtrar Road, Islamabad 45650,Pakistan

Abstract

Nicotinamide Adenine Dinucleotide (NADH) is an intrinsic key fluorophore in cells and tissues of key relevance importance to cellular energy metabolism, mitochondrial functions, antioxidation/generation of oxidative stress, and cell death. Its fluorescence can be quenched by Carbonyl cyanide-p-trifluoro methoxy phenylhydrazone (FCCP). We have investigated in-vitro and cellular (He-La cells) chemical auto-fluorescence quenching quantification of the free and bound NADH/NADPH in a broad range of FCCP quencher concentrations (0.010-5.0) mM. In-vitro studies show significant and more

pronounced fluorescence quenching rate in free-NADH as compared to bound-NADH. The suspended cells show a higher auto-fluorescence quenching rate as compared to both plated cells and free NADH solution. The decrease in red to green ratio with increasing concentration of quencher confirms that FCCP is responsible for mitochondrial depolarization in He-La cells.

7.5.1 Introduction

Fluorescence quenching has turned out to be a valuable tool to explore various aspects of protein binding studies and it first exploited for these type of applications in the late 1960s and early 1970s [348–350]. In Fluorescence quenching phenomenon the fluorescence intensity of the fluorophore is reduced (quenched) while interacting with another molecule, called a quencher. Fluorescence quenching occurs due to many interactions including a Dynamic Quenching [351–353], chemical reaction, and a transfer of energy to the vicinity molecules. The quencher molecule may form a complex by reaching in close proximity, probably with one or more intervening solvent molecules and when this complex is excited, it returns to the ground sate without light emission resulting in static quenching. Fluorescence quenching has many applications including diffusion of oxygen in membranes [354], sensing of a wide variety of analytes including heavy metals [355], Nitric Oxide (NO) [356] and oxygen [357].

The Nicotinamide Adenine Dinucleotide (NAD) is a key cellular water-soluble fluorophore found in bound and free forms in mitochondria and cytosol respectively [358]. This coenzyme is frequently used as a metabolic fingerprint [359, 360]. The NADH, the reduced form of NAD, absorbs at λ=340 nm and emits around λ=465 nm. Upon binding with proteins, change in NADH fluorescence Quantum Yield (QY) occurs (increase or decrease) depending upon the type and way the protein binds with NADH. For example if the NADH binds with protein in an elongated fashion there is a four-fold increase in QY yield which is due to contact prevention between adenine and the fluorescent-reduced nicotinamide group [361]. This increase in QY has been used to study binding of NADH to proteins and single-molecule protein-folding [362, 363]. It contributes in energy metabolism, reductive biosynthesis, and anti-oxidation [364–366], and can be used for cellular investigation without any physical perturbations [367].

The NADH and FAD are metabolic pathways co-enzymes involved in glycolysis, Krebs cycle, and Oxidative phosphorylation [347]. The fluorescence of NADH and flavin represent a major contribution to autofluorescence from the cells [368, 369]. In the reduced state NADH is fluorescent and while in oxidized form NADH is non fluorescent[370]. The oxidation of NADH can be induced by sodium borohydrate, cyanides, and oxygen which react both with free and bound NADH [371, 372]. In the present work we are reporting first time, in-vitro (in solution) fluorescence quenching quantification of FCCP with NADH in a broad range of FCCP concentration i.e, up to 5 mM. We are providing fluorescence quenching quantification across the whole Excitation Emission Matrix (EEM) of NADH. We have extended this in-vitro study towards cellular study in case of He-La cell line. We did auto-fluorescence quantification of free and bound NADH in He-La cells across a broad range of FCCP concentrations (0.010-1.00) mM. We did comparison auto-fluorescence quenching of plated and suspended He-La cells with NADH solution fluorescence quenching study. The JC-1 staining experiment was performed on He-La cells and plotted the red to green ratio versus FCCP concentration.

7.5.2 Materials and Methods

Free and bound NADH Sample Preparation

To prepare free NADH and NADPH solution first a stick solution of 5 mM of NADH and NADPH was prepared. Other concentrations were obtained just by dilution in distilled water. To prepare bound-NADH in solution, 50 μM β-NADH was prepared by binding the L-Malate Dehydrogenase (L-MDH, Sigma Aldrich ♯10127248001, from pig heart) protein. Both 50 μM NADH (Sigma Aldrich ♯ 10107735001) and 100 μM L-MDH was dissolved in 100 mM Mops (Sigma Aldrich ♯ M1254) buffer (pH 7.0) to prepare 50 μM β-NADH. Moreover, to prepare 50 μM β-NADPH, 50 μM NADPH (Sigma Aldrich ♯ 10107824001) and 100 μM L-MDH was mixed in 100 mM Mops buffer (pH 7.0). Meanwhile 50 mM of FCCP (Sigma Aldrich ♯ C2920-50MG) solution was prepared in Dimethyl Sulfoxide (DMSO, Sigma Aldrich ♯ 8418-50ML). Appropriate amount of FCCP is mixed with the β-NADH solution to yield the following final concentration of FCCP; 0 μM (control), 10 μM, 20 μM, 30 μM, 40 μM, 50 μM, 100 μM, 150 μM, 200 μM, 250 μM, 300 μM, 500 μM, 1 mM, 2 mM and 5 mM. The same procedure was followed for the β-NADPH. The L-Malate Dehydrogenase (L-MDH, Sigma Aldrich ♯10127248001, from pig heart) was used to bind NADH with protein [372]. The experiment was performed in quartz cell on room temperature.The fluorescence emission was measured on a Cary Eclipse fluorescence spectrometer (Varian) by exciting the sample at λ=340 nm, while the emission recorded in the range of λ=400-550 nm.

He-La cell Suspension and Fluorescence Spectra

The He-La cells from ATTC (CCL-2) were sub-cultured and maintained in the complete culture medium (Dulbecco's modified Eagle's medium (DMEM)-high glucose, Sigma Aldrich, D5796) containing 10% fetal bovine serum (FbS; Gibco, Catalog No: 16000-044), penicillin/streptomycin (P/S; 100U/ml; Gibco, Catalog No $\sharp$ 15240-062). Cells were incubated at 37 C^o 5% CO_2 incubator. Passaging of cells performed as they reach at confluence of 80 %. Cells were washed PBS and trypsinised with TrypLE (GIBCO, Australia, Catalog No $\sharp$ 12563-029). Following incubation with trypsin for 5 minutes at 37 C^o, a complete medium was added to trypsinised cells. The cell suspension was centrifuged at 500 g for 5 minutes. After removing the supernatant, the cell pellet was resuspended in the complete medium. The Trypan blue 0.4% (Sigma Aldrich, Australia, Catalog No: T8154) used for cell viability test. The He-La cells from ATTC (CCL-2) sub-cultured. The He-La cells were resuspended in the Hanks solution in a quartz cell 750 μl excited at λ=340 nm and fluorescence data acquired from λ=400-650 nm on a Fluorolog Tau-3 Lifetime System.

Measurement of Membrane Potential

The cultured He-La cells in dishes were treated with (0.050 mM, 0.100 mM, 0.150 mM, 0.200 mM, 0.300 mM and 1.0 mM) of FCCP concentraion. The JC-1 staining dye (Life Technologies, Cat# M34152) was used for labeling cells treated with FCCP. The DMSO of 230 μl was used to dissolve the contents of one vial which results in the formation of a 200 μM stock solution of JC-1. The He-La cells incubated at a final 0.002 mM concentration of JC-1 and followed by 20 minutes incubations after washing in phosphate-buffered saline (PBS). Leica SP-2 confocal microscope used for imaging of the labeled cells. The spectral images were collected at λ_{exc}=488 nm for each group of treated and control He-La cells in the range of λ=520-660 nm by keeping a 10 nm window. The emission spectra were collected with peak emissions at λ=590 nm (red) andλ=535 nm (green). These wavelengths are respectively appropriate for the aggregated and monomeric forms of JC-1. The red to green fluorescence intensity ratios provides the membrane potential estimation in mitochondria.

7.5.3 Results and Discussions

Free and Bound NADH/NADPH Quenching in Solution

For in-vitro studies 0.050 mM of free and bound NADH/NADPH solutions placed in the quartz cell and excited at λ_{max}=340 nm. The emission recorded at λ=400-550 nm. The fluorescence intensity change and λ shift are the two parameters which are used to differentiate free and bound-NADH /NADPH. In the literature a blue shift of 20 nm and increase in fluorescence intensity reported due to proteins binding with NADH/NADPH [373]. Chemical reaction of FCCP with NADH is given below 7.2 and image taken from [235]. The figure 7.3 (a-e) shows in-vitro fluorescence quenching

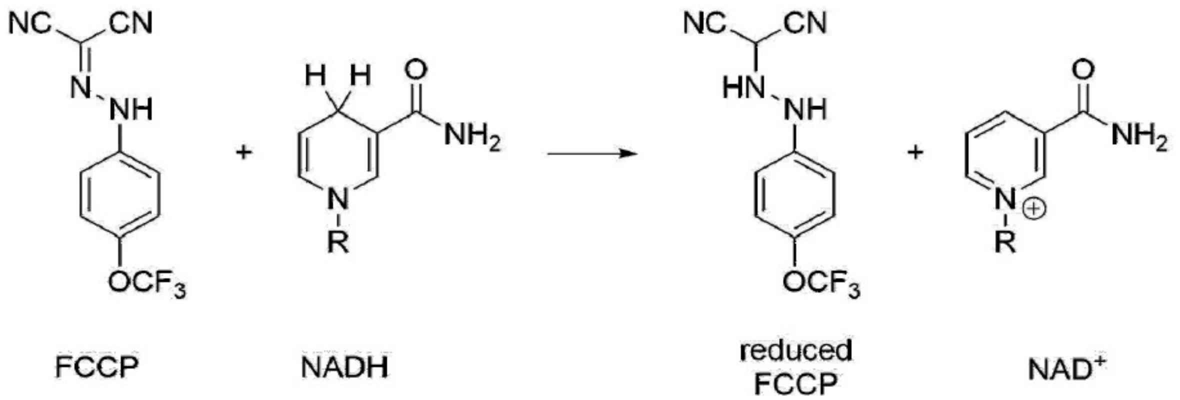

Figure 7.2: Oxidation of NADH

results for free and bound NADH/NADPH. The figure 7.3 (a) shows the emission spectrum of free-NADH after excitation at λ=340$\pm$1 nm [374]. In case of bound-NADH fluorescence peak intensity wavelength λ=465 nm with 560 counts and shifted to λ=445 nmwith $\Delta\lambda$=20 nm showing 310 counts as shown in figure 7.3 (a,c) and similarly a blue shift $\Delta\lambda$ at peak fluorescence intensities is observed for NADPH [375] and is shown in the figure 7.3 (b,d). Moreover a two-fold increase in the fluorescence intensity of NADPH was observed after a bond formation with L-Malate Dehydrogenase (L-MDH, Sigma Aldrich ♯ 10127248001 protein). The fluorescence intensity of aqueous solution of free-NADPH is less as compared to protein-bound NADPH . The binding inhibits the quenching of NADH by the adenine group at λ=340 nm, while same adenine group is the main cause of an increase in the fluorescence emission intensity of NADPH. So an increase in the fluorescence quantum yield is one tool for confirmation of NADPH binding to proteins [376]. In our case fluorescence QY is two-fold shown in figure 7.3 (b, d). If any compound blocks the NADH oxidation like rotenone there may be an increase in NADH fluorescence. The Stern-Volmer graph shows the effects of the quencher concentration on fluoresence quantitatively. If any compound blocks the NADH oxidation like rotenone there may be an increase in NADH fluorescence [377]. The figure 7.3 (e) the graphs explain the free and bound NADH/NADPH fluorescence spectra along with a Stern-Volmer plot. For static chemical quenching equation can be written as below

$$\frac{I_o}{I} = 1 + K_s[Q] \tag{7.1}$$

I_0 and I are the fluorescence intensities of NADH/NADPH before and after quenching and [Q] is the quencher FCCP concentration (0.010-5.000) mM and K_s bio-molecular static quenching constant which can be defined as

$$K_{sv} = \frac{[I - Q]}{[I][Q]} \tag{7.2}$$

In case of free NADH/NADPH, K_{sv} remains between 0.016 and $0.115\times10^{06}(M^{-1})$ while for bound NADH/NADPH it varies between (0.024 and $0.377\times10^{06}(M^{-1})$, where [I-Q] is the concentration of the complex, and [Q] is the FCCPconcentration [378]. The results may differ due to inner filter effect that is fluorescence quenching due to re-absorption of emitted light by FCCP. Two approaches have been used to explain the process of fluorescence quenching in NADH/NADPH solution . Firstly FCCP form a chemical bond with NADH/NADPH, resulting in static fluorescence quenching. Secondly, it results in the formation of a non-fluorescent ground-state complex between the NADH and FCCP. During complex formation [FCCP-NADH] NADH/NADPH are oxidized while reducing FCCP [379]. In Figure 7.3 (a-e) from the fluorescence emission spectrum of 0.050 mM free NADH/NADPH solution in which the FCCP concentration varied from (0.010-5.0) mM, it is clear that both the given fluoropheres NADH/NADPH reduce their fluorescence in the presence of FCCP till fluoresence vanishes.

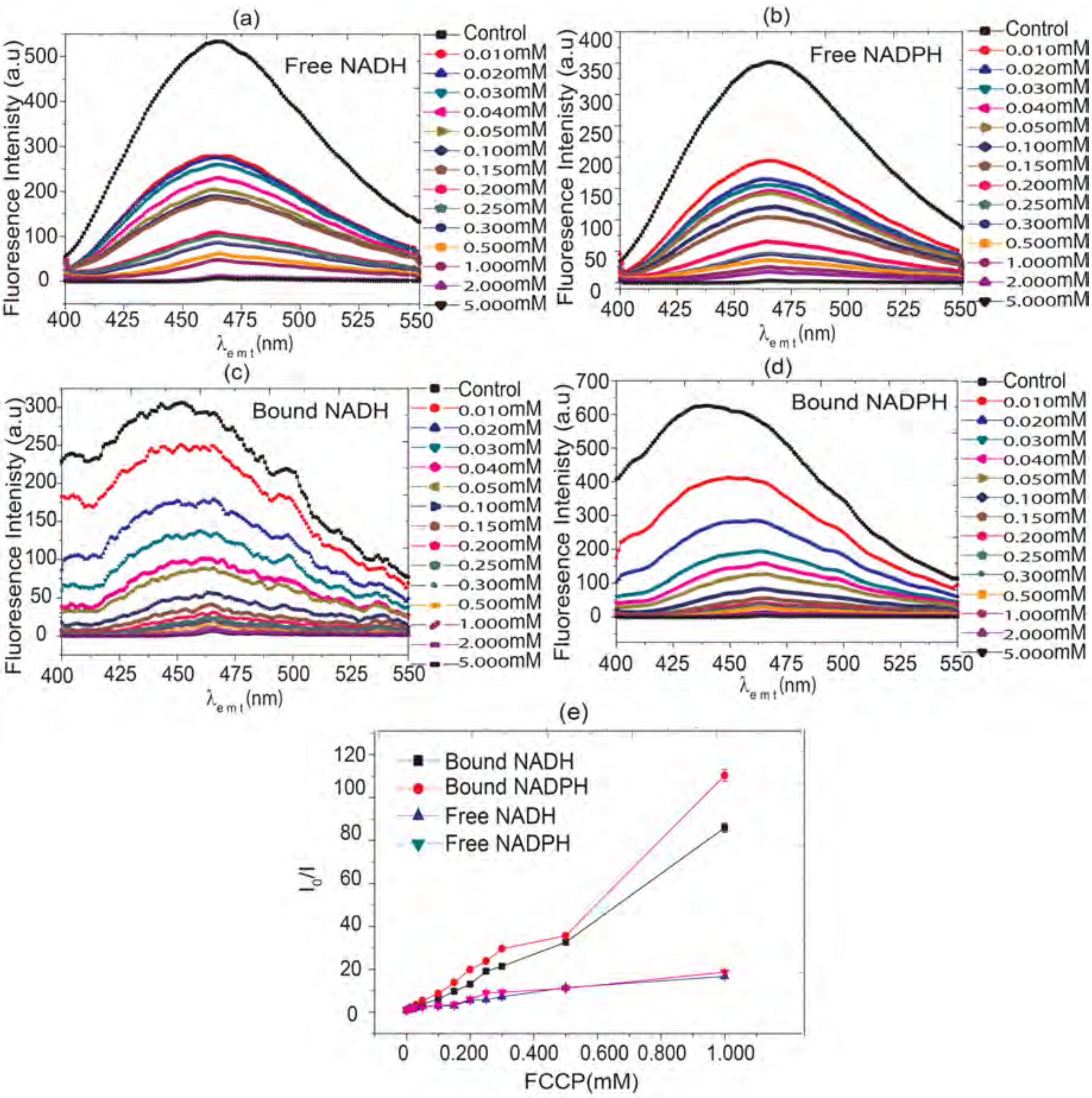

Figure 7.3: (a) Fluorescence emission spectra of the 0.050 mM NADH solution in which FCCP (0.010-5.0) mM solution added, and excited at λ=340±1 nm (b) Fluorescence emission spectra of the 0.050 mM free NADPH solution in which FCCP(0.010-5.0) mM solution added, and excited at λ=340±1 nm (c) Fluorescence emission spectra of the 0.050 mM bound-NADH solution in which FCCP(0.010-5.0) mM solution added, and excitation at λ=340±1 nm (d) Fluorescence emission spectra of the 0.050 mM bound NADPH solution in which FCCP(0.010-5.0 mM) solution added, and excited at λ=340±1 nm (e) Stern-Volmer plot of free and bound NADH and NADPH at maximum fluorescence intensity

EEM and Fluorescence Quenching Quantification

To explore the fluorescence quenching effects in broad range of FCCP concentration we have taken the excitation emission spectrum of NADH using the Cary Eclipse fluorescence spectrometer. To acquire 3-D data for every sample λ_{exc}=280-380 nm and λ_{emt}=400-550 nm used and constructed the Excitation Emission Matrix (EEM). The fluorescence emission data covers the absorption and emission range of NADH [380, 381]. Now to acquire the quantitative fluorescence quenching results FCCP concentration has been increased from 0.050-1.0 mM in small steps while keeping NADH concentration constant i.e., at 50 μM. The EEMs have plotted in MAT-LAB and their fluorescence intensities 3-D plots with color mapping providing an overall fingerprint of fluoropheres are shown in the figure 7.4 (a-f). Here a single profile elucidates full ranges of excitation-emission, so newly emerged fluorophores can be distinguished by carefully investigating the emission profile [382, 383]. The maximum fluorescence emission of 500 counts were found for NADH without FCCP figure 7.4(a) while minimum 30 counts observed for 01 mM FCCP concentration shown in figure 7.4 (f). For some of the graph we also observed secondary peaks at longer emission wavelength. Its origin based on the fact that the scattered light constitutes λ and its integral multiples values of λ with exponentially decreasing intensity [384, 385]. The FCCP concentration of 0.010 mM reduces the fluorescence approximately up to 50 % in case of free-NADH/NADPH solution, and the fluorescence emission intensity decreases in a linear fashion with the FCCP concentrations.

He-La Cells Suspension and Fluorescence Quenching Quantification

The figure 7.5 (a-b) shows the auto-fluorescence quenching quantification results of He-La cell suspension. The control He-La cells (without FCCP) show the highest auto-fluorescence signal. There is approximately 50% decrease in fluorescence intensity after treatment of He-La cells with 0.050 mM concentration of FCCP. The auto-fluorescence of He-La cells quenching occur across all the FCCP concentrations. The FCCP has a high affinity to make chemical bond with NADH molecules like other cyanide molecules such as carbonyl cyanide m-chloro phenylhydrazone (CCCP). As the FCCP makes a chemical bond it oxidises the NADH. The process of oxidation in NADH ultimately

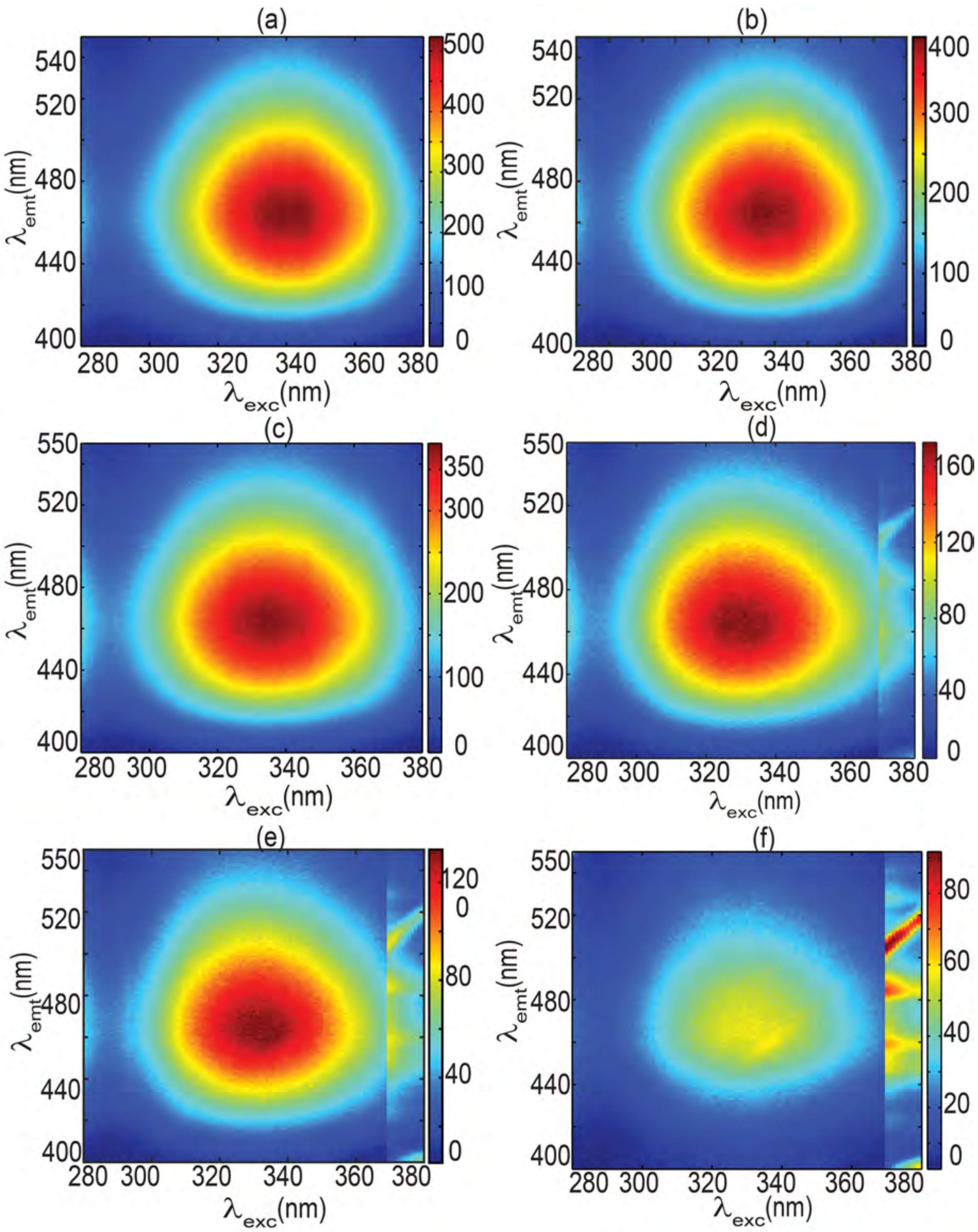

Figure 7.4: (a) Fluorescence EEM of 0.050mM free NADH solution (b) Fluorescence EEM of 0.050 mM free-NADH solution with 0.050 mM FCCP concentration (c) Fluorescence EEM of 0.050 mM free-NADH solution with 0.10 mM FCCP concentraion (d) Fluorescence EEM of 0.050 mM free-NADH solution with 0.30 mM FCCP concentration (e) Fluorescence EEM of 0.050 mM free-NADH solution with 0.500 mM FCCPconcentration (f) Fluorescence EEM of 0.050 mM free-NADH solution with 1.0 mM FCCPconcentraion

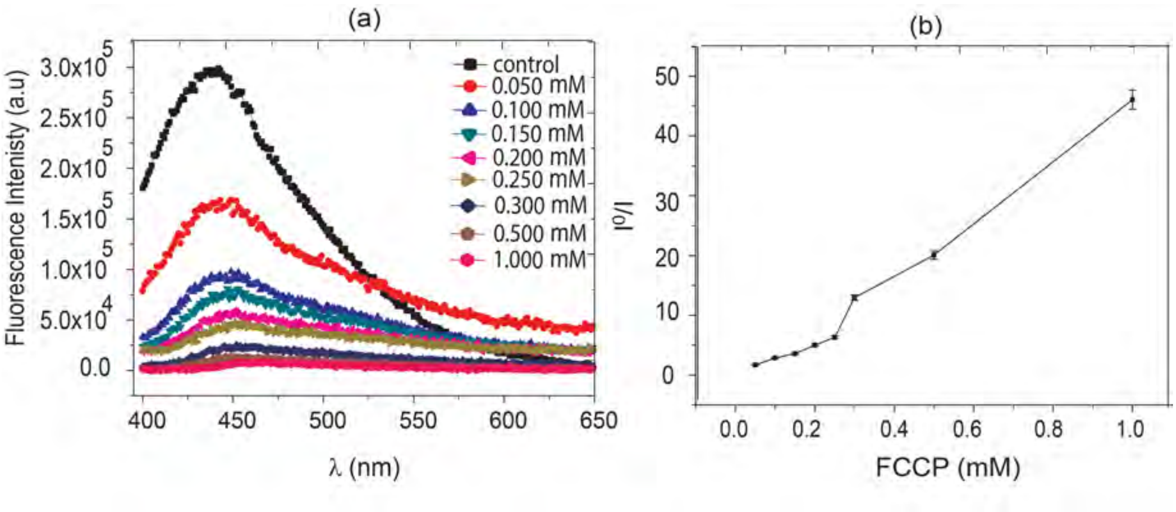

Figure 7.5: (a) Auto-fluorescence quenching of He-La cell suspension FCCP(0.050-1.0) mM concentrations added and excited at λ=340±1 nm (b) Stern-Volmer plot for the bound-NADH in He-La cell suspension, here I_0 and I are intensity without and with quenching

changes the redox-ratio and disturbs the glycolysis, Krebs cycle, and oxidative phosphorylation [347, 371]. So, the process of auto-fluorescence quenching disturbs the whole energy metabolism.

In-Vitro Fluorescence Quenching Comparison

A comparison of 0.050 mM NADH solution, plated and suspended He-La cells made is shown in Figure 7.6. This graph shows that the NADH solution quenching rate lies between plated and suspended cells. The higher values of the fluorescence intensity in case of Platedcells by the addition of FCCP may be explained by the tendencies of some cells to immediately respond to uncouplers with a reversing of the ATPase, hydrolyzing ATP in an effort to stabilize the mitochondrial membrane potential [386–388].

Depolarization of Mitochondria and Membrane Potential

The membrane potential probes are based on sensitivity of the electric potential in the cells. The carbo-cyanine dyes typically react to the potential by aggregation in the membranes, but overall the effects of the electric potential are quite small, so

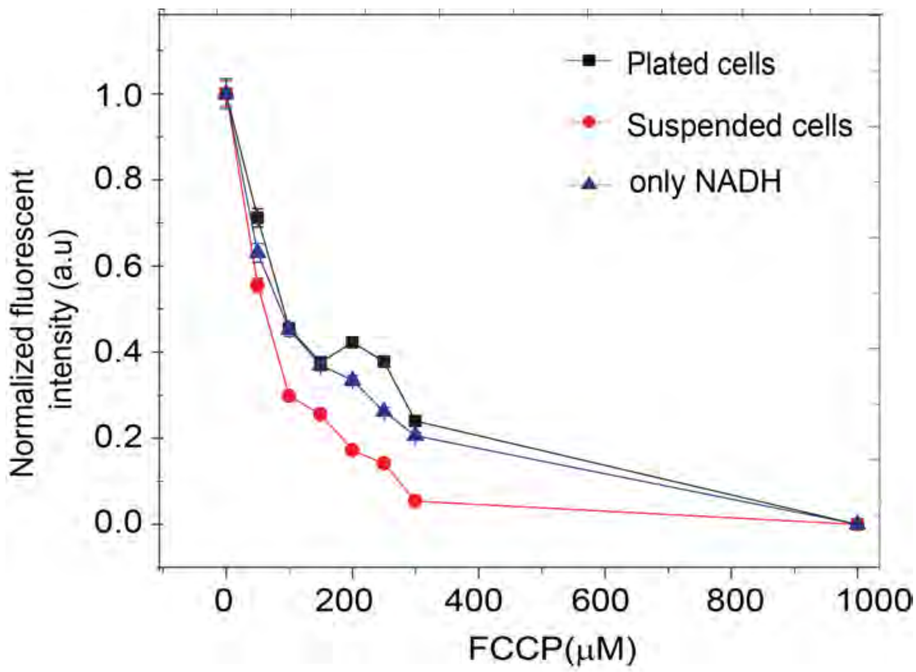

Figure 7.6: Fluorescence quenching comparison of NADH in solution, suspended and plated cells

intensity ratios are often used to provide more stable results [389, 390]. We investigated the variation of membrane potential with increasing concentration of FCCP (0.050-1.000) mM while He-La cells were stained with the JC-1 dye.The same pinhole aperture and detector voltage were used for both red and green JC-1 images. Mitochondrial depolarization is indicated by a decrease in the red to green fluorescence intensity ratio. The potential-sensitive wavelength shift is due to concentration-dependent formation of red fluorescent J-aggregates in the mitochondria. In control cells JC-1 forms aggregates with intense red fluorescence, while in cells with defective mitochondria it has a monomeric form which emits green fluorescence. As a result, the red /green intensity ratio decreases as cellular metabolic activity decreases [391]. Kaisa M. Heiskanen etal;. demonstrated that the treatment of pheochromocytoma-6 cells with staurosporine shows mitochondrial membrane depolarization which can be monitored by tetra-methyl rhodamine methyl ester along with laser-scanning confocal microscopy using the signal of green fluorescent protein-tagged cytochrome c [392]. So green fluorescent proteincan be used as an indicator for membrane potential monitoring. The mitochondrial membrane potential measured here using JC-1 demonstrates

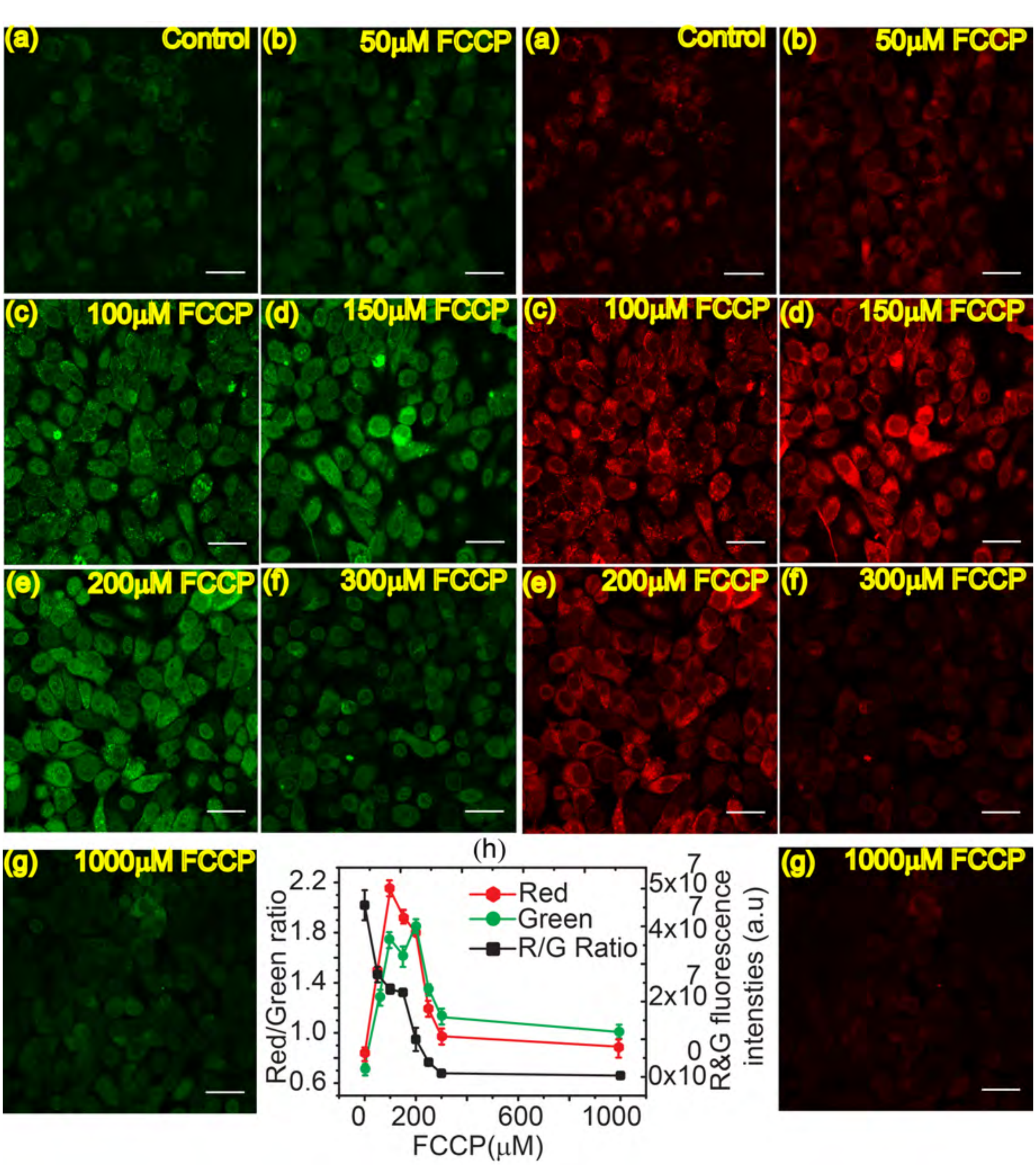

Figure 7.7: Confocal laser scanning microscopy images of He-La cells treated with FCCP (0.050-1.00) mM (a-g) show JC-1 fluorescence in two emission channels λ=532 nm (green image) and λ=590 nm (red images), (h) Red to green fluorescence ratio obtained from the analysed images in Image J software . The images are presented without any post-processing. Bar scale=200 μm and magnification= 200×

that the cellular mitochondria is affected directly by FCCP leading to decreased mitochondrial activity. The analysis is shown in figure 7.7 (h) [393]. We observed a shoulder in the red to green ratio of JC-1 staining (figure 7.7 (h)), a slight local increase in NADH /NADPH which is due to increased mitochondrial activity [394]. The increases in fluorescence of bound NADPH by the addition of FCCP may be explained by the tendencies of some cells to immediately respond to uncouplers with a reversing of the ATPase, hydrolyzing ATP in an effort to stabilize the mitochondrial membrane potential [387, 388]. The FCCP, after oxidizing the mitochondrial NADH stimulates cellular respiration in He-La cells. The red to green ratio fluorescence is related to the mitochondrial membrane potential [395]. As the FCCP oxidises NADH so NAD^{+} increases which may effect anti-oxidation and oxidative stress generation [396]. The NAD^{+} can be converted by NADKs to $NADP^{+}$ which is the precursor for NADPH formation [397]. We successfully demonstrated fluorescence quenching quantification the free and bound NADH/NADPH with FCCP in a broad range of FCCP (0.010-1.00) mM concentrations. The FCCP quenches the fluorescence quantity proportional to its concentration for NADH/NADPH fixed concentration. The auto-fluorescence quenching in He-La cell line suspension confirms that at the first instance cell respond maximum than settle down for other concentration. The free-NADH/NADPH shows higher quenching rate then bound-NADH/NADPH. The He-La cells in suspension show the highest, while plated cells show the lowest quenching rate. The anti-oxidants, oxidative stress and oxidative phosphorylation following FCCP exposure is the main cause of this effect. The red to green ratio decrease with increasing FCCP concentration, showing that there is depolarization of mitochondria during fluoresce quenching in He-La cell line.

7.5.4 Acknowledgement

This work was partially supported by the Australian Research Council (CE140100003), International Macquarie University Research Excellence Scholarship (iMQRES) -No. 2014030. I am extremely thankful to Dr Keith Imrie an Honorary Associate from Department of Electrical Engineering Faculty of Science and Engineering for proof reading of this Manuscript.

8

Auto-Fluorescence Quenching and Unmixing of Free and Bound NADH in He-La Cells (Publication VI)

8.1 Hyperspectral Imaging Introduction

A fluorescence hyperspectral imaging system consists of the following components

1. A combination lamp along with monochromator for λ selection.
2. A filter cube (exciter, dichroic and emitter).
3. A microscope with suitable objective to image tissues or cells.
4. A detector (CCD/EMCCD) array having suitable quantum efficiency.
5. A computer system to operate the whole imaging system.

RGB image has three colours: Red, Green and Blue while a hyper-spectral image consist of more than three channel. The image formed is called hypercube. A schematic diagram of hyperspectral imaging is shown in figure 6.1 of Chapter 6, section 6.3. A hyper spectral image of He-La cells taken by the author is shown in figure 8.1 a,b,c. Data noise and background is removed from the image and smoothing is done using a spectral Graphical user interface. The hyperspectral image become ready for unmixing. The hyperspectral unmixing techniques has discussed in detail in chapter 6. The hyperspectral data-sets use advanced image-classification methods for the extraction, unmixing, and classification of relevant spectral information from the data of the captured image [241, 243, 261].

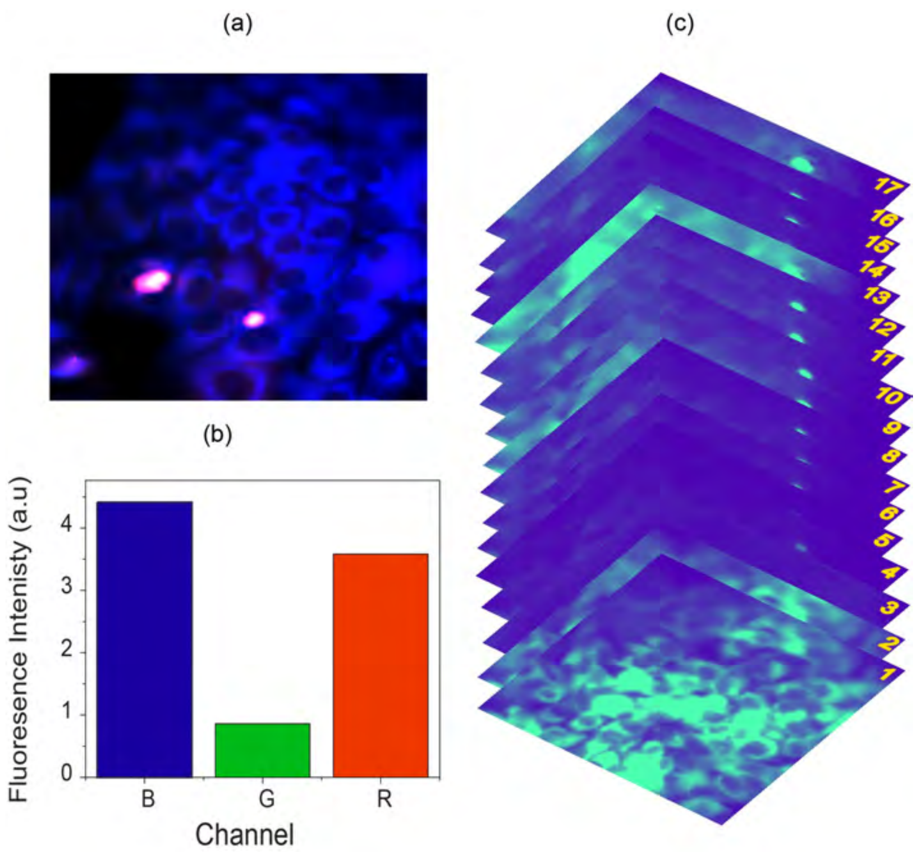

Figure 8.1: Difference between RGB image and hyperspectral image (a) RGB image of He-La cells (b) Blue,green and red fluoresce intensity (c) Hyperspectral Image with 17 channel starting from λ_{exc}=365-495 nm for He-La cells.

8.2 Motivation for Auto-Fluorescence Quenching and Unmixing

In chapter 7 we performed experiments for in-vitro and in-vivo fluorescence quenching quantification of free and bound NADH. In this part of the study, we aim to validate the hyper-spectral auto-fluorescence unmixing of natural cellular fluoropheres especially NADH and FAD through quenching work. First, we performed chemical quenching study of NADH and based on these results we acquired hyper-spectral auto-fluorescence images for FCCP treated and untreated He-La cells.

8.3 Author's Contribution to Publication VI

Being the principal author of the article having the title "Fluorescence quenching of free and bound NADH in He-La cells determined by hyperspectral imaging and unmixing of cell auto-fluorescence" I have discussed the idea with principal supervisor Ewa, M. Goldys. Mr Aziz ul Rehman and Dr Ayad, G. Anwer together performed the experiments which include; quenching quantification data of NAD^+/NADH, $NADP^+$/NADPH kit quantification data, plated cells quenching data, and hyperspectral auto-fluorescence data for FCCP treated and untreated cells. Dr Martin, E. Gosnell analysed the hyper-spectral data and plotted the box plots. Dr Saabah B. Mahbub has written unsupervised unmixing method section for hyper-spectral imaging, Dr Guozhen Liu contributed to the discussion for the chemical reaction of NADH and FCCP. Initially, the manuscript was written by the principal author than each author contributed related to their field. Finally Ewa, M. Goldys polished it and contributed to the discussion so that work can publish in a peer-review journal.

8.4 Publication VI

Aziz ul Rehman, Ayad, G. Anwer, Martin, E. Gosnell, Saabah, B. Mahbub, Guozhen, Liu, and Ewa, M. Goldys, Fluorescence quenching of free and bound NADH in He-La cells determined by hyperspectral imaging and unmixing of cell autofluorescence Biomedical Optics Express 8, 488-1498 (2017)

Pages 120-130 of this thesis have been removed as they contain published material. Please refer to the following citation for details of the article contained in these pages.

Rehman, A., Anwer, A. G., Gosnell, M. E., Mahbub, S. B., Liu, G., & Goldys, E. M. (2017). Fluorescence quenching of free and bound NADH in HeLa cells determined by hyperspectral imaging and unmixing of cell autofluorescence. *Biomedical Optics Express*, 8(3), p. 1488-1498.

DOI: 10.1364/BOE.8.001488

9

Conclusion and Future Work

9.1 Conclusions

Knowledge of optical parameters (absorption coefficients μ_a and reduced scattering coefficients $\mu_{\acute{s}}$) have crucial importance in understanding the light-tissue interaction. The solution of Photon Transport Equation (PTT by applying First-order scattering, K-M Theory, Monte-Carlo Simulation and Inverse Adding-Doubling (IAD) methods provide the values of the optical parameters μ_a, μ_s, and g.

The malignant tissues have significantly higher reduced scattering $\acute{\mu_s}$ and absorption coefficients μ_a, and effect the signal to noise ratio (SNR). Thin sample holder made of microscopic coverslips solved S/N ratio problem by measuring diffuse reflectance R_d and diffuse transmittance T_d of 1.0% Indian-ink and 20% intralipid tissue body phantoms while placing the sample holder in a Double Integrating Sphere System at λ=632.8 nm . The μ_a and μ_s for 20% Intralipid was found to be 0.112±0.046 cm^{-1} and 392.299±10.090 cm^{-1} at λ=632.8 nm by applying Inverse Adding-Doubling method. The μ_a and μ_s for 1.0% Indian-ink found to be μ_a =9.808±0.490 cm^{-1} and μ_s =1.258±0.063 cm^{-1} at λ=632.8 nm by applying Inverse Adding-Doubling method. The repeatability and reproducibility of the Double Integrating Sphere system found to be within 4.9% error. The optical parameters quantitative characterisation study of Indian-ink and Intralipid tissue mimic body phantoms shows linear relationship with the concentrations which has many biological diagnostics and therapeutic applications. The Raman, polarimetric and fluorescence spectroscopic optical diagnostic techniques successfully differentiated the normal and cancerous human breast tissues. Spectroscopic data collected from freshly excised surgical specimens of normal tissues with Raman bands at 800 cm^{-1}, 1171 cm^{-1} and 1530 cm^{-1} arising mainly by lipids, nucleic acids, proteins, carbohydrates and amino acids. For breast cancerous tissues, Raman bands observed to be at 1070 cm^{-1}, 1211 cm^{-1}, 1495 cm^{-1}, 1583 cm^{-1} and 1650 cm^{-1} wave-number.

The indigenous made Programable Integrating Sphere Light (PISL) source is tuneable in the range of λ=365-490 nm and has a uniform spatial profile and narrow spectral width. The retrofitted Programable Integrating Sphere Light (PISL) source into the fluorescence inverted microscope DM-IRB (Leica) together with a highly sensitive low-noise CMOS camera has carried out multi-spectral auto-fluorescence images of live BV_2 cells.

Hyperspectral auto-fluorescence Imaging (HSFI) and unmixing techniques literature review part II provided explanation of HSFI methods, feature selection and extraction techniques and analysis. The hyperspectral imaging systems can be coupled with Raman scattering, fundus cameras, confocal and conventional microscopes for application in medical field. In-vitro fluorescence quenching quantification of free and bound-NADH in a broad range of FCCP concentrations (0.010-5.0) mM can be used for tissue optical differentiation . The free-NADH has higher quenching rate as compared to bound-NADH for In-vitro studies . The free-NADH solution has lower auto-fluorescence quenching rate then suspended He-La cells in case of plated cells . The red to green auto-fluorescence ratio images indirectly show depolarization of mitochondria . The label-free method of hyperspectral imaging of cell auto-fluorescence combined with unsupervised unmixing separately isolated the emissions of free and bound-NADH . Hyperspectral image analysis of FCCP-treated He-La cells confirms that FCCP by selection quenches auto-fluorescence of free and bound-NAD(P)H up to high concentrations values. This is confirmed by the measurements of average NAD/NADH and NADP/NADPH content in cells. The selective auto-fluorescence quenching quantification of NADH/ NAD(P)H with FCCP has validated the results of unbiased unmixing of He-La cell auto-fluorescence.

9.2 Future Direction

We can extend the Programmable LEDs-Based Integrating Sphere Light (PISAL) source tunability range from λ=365 nm to λ=200 nm in an integrating sphere just by adding high power deep UV-LEDs. So PISAL source in the future can be used for Wide-Field Fluorescence Imaging of many chromophores Tryptophan, DNA, Proteins and many other fluoropheres in a cell using spatial uniform light source. The photodynamic therapy (PDT) can be monitored by quantifying the reactive oxygen species made through the photo-chemical reaction. There exist natural fluorophores NADH and FAD in each cell whose oxidation and reduction state indirectly tell us about the metabolic activity. The NADH and FAD are the cellular key fluorophores, and their auto-fluorescence quenching quantification provides an insight into the cellular metabolic activity. The NADH gives fluorescence in reduced form while NAD^+ does not . Similarly, FAD oxidized form gives fluorescence while reduced form does not. So, by measuring the auto-fluorescence of both NADH and FAD^+ simultaneously, we can predict the metabolic activity of the cell that is an important parameter in programmed cell death. The auto-fluorescence of NADH and FAD can be measured on each single spectral channel by performing hyper-spectral images on a system coupled with an Integrating-Sphere Light Source PISAL, and it can be used for monitoring the photodynamic therapy PDT .

References

[1] S. Firdous, M. Ahmed, A. Rehman, M. Nawaz, S. Anwar, and S. Murtaza. Transmission spectroscopy of dengue viral infection. Laser Physics Letters 9(4), 317 (2012).

[2] M. Mori, T. Chiba, A. Nakamizo, R. Kumashiro, M. Murata, T. Akahoshi, M. Tomikawa, Y. Kikkawa, K. Yoshimoto, and M. Mizoguchi. Intraoperative visualization of cerebral oxygenation using hyperspectral image data: a two-dimensional mapping method. International journal of computer assisted radiology and surgery 9(6), 1059 (2014).

[3] C. Elwell. A practical users guide to near infrared spectroscopy (1995).

[4] V. V. Tuchin. Tissue Optics and Photonics: Light-Tissue Interaction II. Journal of Biomedical Photonics & Engineering 2(3), 030201 (2016).

[5] S. L. Jacques, C. Alter, and S. A. Prahl. Angular dependence of hene laser light scattering by human dermis. Lasers Life Sci 1(4), 309 (1987).

[6] P. Parsa, S. L. Jacques, and N. S. Nishioka. Optical properties of rat liver between 350 and 2200 nm. Applied Optics 28(12), 2325 (1989).

[7] R. L. Siegel, K. D. Miller, and A. Jemal. Cancer statistics, 2016. CA a cancer journal for clinicians 66(1), 7 (2016).

[8] C. E. DeSantis, S. A. Fedewa, A. Goding Sauer, J. L. Kramer, R. A. Smith, and A. Jemal. Breast cancer statistics, 2015: Convergence of incidence rates between black and white women. CA a cancer journal for clinicians 66(1), 31 (2016).

[9] K. D. Miller, R. L. Siegel, C. C. Lin, A. B. Mariotto, J. L. Kramer, J. H. Rowland, K. D. Stein, R. Alteri, and A. Jemal. Cancer treatment and survivorship statistics, 2016. CA a cancer journal for clinicians 66(4), 271 (2016).

[10] J. M. Palmer and B. G. Grant. The art of radiometry (SPIE Press Bellingham, WA, USA, 2010).

[11] D. Heath, Z. Wei, W. Fowler, and V. Nelson. Comparison of spectral radiance calibrations of sbuv-2 satellite ozone monitoring instruments using integrating sphere and flat-plate diffuser techniques. Metrologia 30(4), 259 (1993).

[12] J.-C. Boyer and F. C. Van Veggel. Absolute quantum yield measurements of colloidal nayf 4: Er3+, yb3+ upconverting nanoparticles. Nanoscale 2(8), 1417 (2010).

[13] H. Huang, A. S. Susha, S. V. Kershaw, T. F. Hung, and A. L. Rogach. Control of emission color of high quantum yield ch3nh3pbbr3 perovskite quantum dots by precipitation temperature. Advanced Science 2(9) (2015).

[14] S.-Y. Kim, W.-I. Jeong, C. Mayr, Y.-S. Park, K.-H. Kim, J.-H. Lee, C.-K. Moon, W. B, and J.-J. Kim. Organic light-emitting diodes with 30% external quantum efficiency based on a horizontally oriented emitter. Advanced Functional Materials 23(31), 3896 (2013).

[15] S. A. Prahl, M. J. van Gemert, and A. J. Welch. Determining the optical properties of turbid media by using the adding–doubling method. Applied optics 32(4), 559 (1993).

[16] A. V. Arecchi, R. J. Koshel, and T. Messadi. Field guide to illumination (SPIE, 2007).

[17] K. Anderson, G. Archenhold, K. Baldwin, and A. Neal. Non-imaging light source for uniform illumination applications (2002). US Patent 6,422,718.

[18] A. Ducharme, A. Daniels, E. Grann, and G. Boreman. Design of an integrating sphere as a uniform illumination source. IEEE Transactions on education 40(2), 131 (1997).

[19] S. Suga. Integrating sphere type standard light source device (1980). US Patent 4,232,971.

[20] J. W. Pickering, S. A. Prahl, N. Van Wieringen, J. F. Beek, H. J. Sterenborg, and M. J. Van Gemert. Double-integrating-sphere system for measuring the optical properties of tissue. Applied optics 32(4), 399 (1993).

[21] D. Sardar and L. Levy. Optical properties of whole blood. Lasers in medical science 13(2), 106 (1998).

[22] W.-F. Cheong, S. A. Prahl, and A. J. Welch. A review of the optical properties of biological tissues. IEEE journal of quantum electronics 26(12), 2166 (1990).

[23] O. Hamdy, M. Fathy, T. A. Al-Saeed, J. El-Azab, and N. H. Solouma. Estimation of optical parameters and fluence rate distribution in biological tissues via a single integrating sphere optical setup. Optik-International Journal for Light and Electron Optics 140, 1004 (2017).

[24] A. Ishimaru. Diffusion of light in turbid material. Applied optics 28(12), 2210 (1989).

[25] R. Bonner, R. Nossal, S. Havlin, and G. Weiss. Model for photon migration in turbid biological media. JOSA A 4(3), 423 (1987).

[26] A. Ishimaru. Wave propagation and scattering in random media, vol. 2 (Academic press New York, 1978).

[27] A. Ishimaru. Wave propagation and scattering in random media and rough surfaces. Proceedings of the IEEE 79(10), 1359 (1991).

[28] P. Kubelka. The kubelka-munk theory of reflectance. Z Tech Phys 12, 539 (1931).

[29] N. Metropolis and S. Ulam. The monte carlo method. Journal of the American statistical association 44(247), 335 (1949).

[30] M. S. Patterson, B. Chance, and B. C. Wilson. Time resolved reflectance and transmittance for the noninvasive measurement of tissue optical properties. Applied optics 28(12), 2331 (1989).

[31] D. Boas, M. O'leary, B. Chance, and A. Yodh. Scattering of diffuse photon density waves by spherical inhomogeneities within turbid media: analytic solution and applications. Proceedings of the National Academy of Sciences 91(11), 4887 (1994).

[32] J. Li, G. Ku, and L. V. Wang. Ultrasound-modulated optical tomography of biological tissue by use of contrast of laser speckles. Applied optics 41(28), 6030 (2002).

[33] M. R. Ostermeyer and S. L. Jacques. Perturbation theory for optical diffusion theory: a general approach for absorbing and scattering objects in tissue. In Optical Tomography, Photon Migration, and Spectroscopy of Tissue and Model Media: Theory, Human Studies, and Instrumentation, vol. 2389, pp. 98–102 (Proc. SPIE, 1995).

[34] G.-W. Yoon. Absorption and scattering of laser light in biological media-mathematical modeling and methods for determining the optical properties. Tech. rep., Texas Univ., Austin, TX (USA) (1988).

[35] H.-J. Wei, D. Xing, G.-Y. Wu, Y. Jin, and H.-M. Gu. Optical properties of human normal small intestine tissue determined by kubelka-munk method in vitro. World journal of gastroenterology 9(9), 2068 (2003).

[36] S. S. Mikhail, S. S. Azer, and W. M. Johnston. Accuracy of KubelkaâĂŞMunk reflectance theory for dental resin composite material. Dental Materials 28(7), 729 (2012).

[37] L. Simonot, M. Thoury, and J. Delaney. Extension of the kubelka–munk theory for fluorescent turbid media to a nonopaque layer on a background. JOSA A 28(7), 1349 (2011).

[38] C. Sandoval and A. D. Kim. Extending generalized kubelka–munk to three-dimensional radiative transfer. Applied optics 54(23), 7045 (2015).

[39] M. H. Brill. Calibrating low-scattering samples using kubelka-munk model. Color Research & Application 42(1), 123 (2017).

[40] H. A. Gaonkar, D. Kumar, R. Ramasubramaniam, and A. Roy. Decoupling scattering and absorption of turbid samples using a simple empirical relation between coefficients of the kubelka–munk and radiative transfer theories. Applied optics 53(13), 2892 (2014).

[41] W. E. Vargas. Diffusion and absorption of the non-homogenous material by kubella munk modle. Optica Pura Aplicada 44, 163 (2011).

[42] L. Yang, B. Kruse, and S. J. Miklavcic. Revised kubelka–munk theory. ii. unified framework for homogeneous and inhomogeneous optical media. JOSA A 21(10), 1942 (2004).

[43] A. Roy, R. Ramasubramaniam, and H. A. Gaonkar. Empirical relationship between kubelka–munk and radiative transfer coefficients for extracting optical parameters of tissues in diffusive and nondiffusive regimes. Journal of Biomedical Optics 17(11), 115006 (2012).

[44] A. Rehman, S. Firdous, M. Nawaz, and M. Ahmad. Optical parameters measurement for diagnostic and photodynamic therapy of human cervical adenocarcinoma (hela) cell line. Laser Physics 22(1), 322 (2012).

[45] B. G. Yust, D. K. Sardar, and A. Tsin. A comparison of methods for determining optical properties of thin samples. In Proceedings of SPIE, vol. 7562 (NIH Public Access, 2010).

[46] I. Fine and A. Kaminsky. Speckle-based measurement of the light scattering by red blood cells in vivo. In Proc. SPIE, vol. 7898, p. 78980A (2011).

[47] P. Sun, R. Q. Yang, F. H. Xie, J. Q. Ding, F. Q. Zhang, and X. P. Cao. A method for determining optical properties of human tissues by measuring diffuse reflectance with ccd. In Proc. of SPIE Vol, vol. 7845, pp. 784522–1 (2010).

[48] P. Ruan, R. Li, F. Gao, F. Yang, H. Zhao, and Y. Liu. Two-dimensional shape-based diffuse optical tomography: methodology, silumation and pilot experiment. In BiOS, pp. 75570R–75570R (International Society for Optics and Photonics, 2010).

[49] A. X. Cong, H. Shen, W. Cong, and G. Wang. Improving the accuracy of the diffusion model in highly absorbing media. International journal of biomedical imaging 2007 (2007).

[50] M. Xu, M. Alrubaiee, and R. Alfano. Fractal mechanism of light scattering for tissue optical biopsy. In Optical Biopsy VI, vol. 6091, p. 60910E (International Society for Optics and Photonics, 2006).

[51] S. Bhattacharjee and I. Jose. Early detection of breast cancer: A molecular optical imaging approach using novel estrogen conjugate fluorescent dye. In Proc. of SPIE Vol, vol. 7896, pp. 78961F–1 (2011).

[52] N. Hyvonen. Analysis of optical tomography with non-scattering regions. Proceedings of the Edinburgh Mathematical Society 45(2), 257 (2002).

[53] K. D. Paulsen and H. Jiang. Spatially varying optical property reconstruction using a finite element diffusion equation approximation. Medical Physics 22(6), 691 (1995).

[54] D. Contini, F. Martelli, and G. Zaccanti. Photon migration through a turbid slab described by a model based on diffusion approximation. i. theory. Applied optics 36(19), 4587 (1997).

[55] J. L. Karagiannes, Z. Zhang, B. Grossweiner, and L. I. Grossweiner. Applications of the 1-d diffusion approximation to the optics of tissues and tissue phantoms. Applied optics 28(12), 2311 (1989).

[56] S. Grabtchak, L. G. Montgomery, and W. M. Whelan. Optical absorption and scattering properties of bulk porcine muscle phantoms from interstitial radiance measurements in 650–900 nm range. Physics in medicine and biology 59(10), 2431 (2014).

[57] R. Groenhuis, H. A. Ferwerda, and J. Ten Bosch. Scattering and absorption of turbid materials determined from reflection measurements. 1: Theory. Applied optics 22(16), 2456 (1983).

[58] R. Meier, J.-S. Lee, and D. Anderson. Atmospheric scattering of middle uv radiation from an internal source. Applied optics 17(20), 3216 (1978).

[59] P. Marquet, F. Bevilacqua, and C. Depeursinge. Computing the light distribution in turbid media for different scattering and absorption coefficients from a single monte carlo simulation. Photon Propagation in Tissues 2626, 17 (1995).

[60] L. Oliveira and A. Lage. Monte carlo simulation for the optical transmittance in biological tissues during the action of osmotic agents. In Viscoelastic anisotropy in porcine skin: acousto-optical and mechanical measurements (Invited Paper), vol. 5771, pp. 225–236 (2005).

[61] S. Chu, C. Wu, S. Hua, C. Liu, H. Chiang, J. Lin, and J. Yuan. Monte carlo simulation of the fluorescence spectra of colon and cervical tissues at different dysplasia grades. In Proc. SPIE, vol. 5705, pp. 283–292 (2005).

[62] G. Jagajothi and S. Raghavan. Estimation of optical properties in biological tissues using monte carlo simulation. Journal of Mechanics in Medicine and Biology 7(04), 449 (2007).

[63] A. Kienle and M. S. Patterson. Determination of the optical properties of turbid media from a single monte carlo simulation. Physics in medicine and biology 41(10), 2221 (1996).

[64] S. Chatigny, M. Morin, D. Asselin, Y. Painchaud, and P. Beaudry. Hybrid monte carlo for photon transport through optically thick scattering media. Applied optics 38(28), 6075 (1999).

[65] L. Lin, M. Zhang, and S. Li. A modified condensed monte carlo simulation of reflectance with focus light beam from scattering medium. Optik-International Journal for Light and Electron Optics 126(24), 4876 (2015).

[66] N. Ren, J. Liang, X. Qu, J. Li, B. Lu, and J. Tian. Gpu-based monte carlo simulation for light propagation in complex heterogeneous tissues. Optics express 18(7), 6811 (2010).

[67] H. C. Hulst. A new look at multiple scattering (NASA Institute for Space Studies, Goddard Space Flight Center, 1963).

[68] G. N. Plass, G. W. Kattawar, and F. E. Catchings. Matrix operator theory of radiative transfer. 1: Rayleigh scattering. Applied Optics 12(2), 314 (1973).

[69] S. L. Jacques and S. A. Prahl. Modeling optical and thermal distributions in tissue during laser irradiation. Lasers in surgery and medicine 6(6), 494 (1987).

[70] S. A. Prahl. Optical property measurements using the inverse adding-doubling program. Oregon Medical Laser Center, St. Vincent Hospital 9205 (1999).

[71] B. M. Cruzado, S. A. Prahl, J. D. Atencio, and S. V. Montiel. Validation of a new algorithm for the recovery of optical properties from turbid samples: GA-MCML against IAD program. In Proc. SPIE, vol. 8011, p. 80118O (2011).

[72] X. Ma, J. Q. Lu, H. Ding, and X.-H. Hu. Bulk optical parameters of porcine skin dermis at eight wavelengths from 325 to 1557 nm. Optics letters 30(4), 412 (2005).

[73] D. K. Sardar, R. M. Yow, G.-Y. Swanland, R. J. Thomas, and A. T. Tsin. Optical properties of ocular tissues in the near infrared region. Tech. rep., AIR FORCE RESEARCH LAB BROOKS CITY-BASE TX (2006).

[74] D. K. Sardar, B. G. Yust, F. J. Barrera, L. C. Mimun, and A. T. Tsin. Optical absorption and scattering of bovine cornea, lens and retina in the visible region. Lasers in medical science 24(6), 839 (2009).

[75] D. K. Sardar, R. M. Yow, A. T. Tsin, and R. Sardar. Optical scattering, absorption, and polarization of healthy and neovascularized human retinal tissues. Journal of biomedical optics 10(5), 051501 (2005).

[76] A. Roggan, M. Friebel, K. Dorschel, A. Hahn, and G. J. Mueller. Optical properties of circulating human blood in the wavelength range 400-2500 nm. Journal of biomedical optics 4(1), 36 (1999).

[77] K. Ishii, A. Kimura, and K. Awazu. Optical properties of tissues after laser treatments in the wavelength range of 350-1000 nm. In Proc. SPIE, vol. 6991, p. 69912F (2008).

[78] N. Honda, K. Ishii, A. Kimura, M. Sakai, and K. Awazu. Determination of optical property changes by laser treatments using inverse adding-doubling method. In Proc. SPIE, vol. 7175, p. 71750Q (2009).

[79] A. N. Bashkatov, E. A. Genina, V. I. Kochubey, and V. V. Tuchin. Optical properties of human skin, subcutaneous and mucous tissues in the wavelength range from 400 to 2000 nm. Journal of Physics D: Applied Physics 38(15), 2543 (2005).

[80] M. Allegood and J. Baba. Extension of the inverse adding-doubling method to the measurement of wavelength-dependent absorption and scattering coefficients of biological samples. Journal of Undergraduate Research 8 (2008).

[81] H. Wei, D. Xing, G. Wu, H. Gu, J. Lu, and Y. Jin. Optical properties of human pulmonary artery tissue at Ti: Sapphire laser using inverse Adding-Doubling method in vitro. In PROCEEDINGS-SPIE THE INTERNATIONAL SOCIETY FOR OPTICAL ENGINEERING, vol. 6047, p. 60471X (International Society for Optical Engineering; 1999, 2006).

[82] A. M. Nilsson, R. Berg, and S. Andersson-Engels. Measurements of the optical properties of tissue in conjunction with photodynamic therapy. Applied optics 34(21), 4609 (1995).

[83] C. Chen, J. Q. Lu, H. Ding, K. M. Jacobs, Y. Du, and X.-H. Hu. A primary method for determination of optical parameters of turbid samples and application to intralipid between 550 and 1630 nm. Optics express 14(16), 7420 (2006).

[84] N. Yavari, S. Andersson-Engels, J. S. Dam, J. Antonsson, and K. Wardell. Measurements of optical properties of pig brain tissue in vitro using a novel compact device. In European Conference on Biomedical Optics, p. MG4 (Optical Society of America, 2005).

[85] A. D. Krainov, A. M. Mokeeva, E. A. Sergeeva, P. D. Agrba, and M. Y. Kirillin. Optical properties of mouse biotissues and their optical phantoms. Optics and Spectroscopy 115(2), 193 (2013).

[86] I. Driver, J. W. Feather, P. R. King, and J. B. Dawson. The optical properties of aqueous suspensions of Intralipid, a fat emulsion. Physics in medicine and biology 34(12), 1927 (1989).

[87] A. Mazzoli, R. Munaretto, and L. Scalise. Preliminary results on the use of a noninvasive instrument for the evaluation of the depth of pigmented skin lesions: numerical simulations and experimental measurements. Lasers in medical science 25(3), 403 (2010).

[88] A. Kharine, S. Manohar, R. Seeton, R. G. Kolkman, R. A. Bolt, W. Steenbergen, and F. F. de Mul. Poly (vinyl alcohol) gels for use as tissue phantoms in photoacoustic mammography. Physics in medicine and biology 48(3), 357 (2003).

[89] R. Long, T. King, T. Akl, M. N. Ericson, M. Wilson, G. L. Cote, and M. J. McShane. Optofluidic phantom mimicking optical properties of porcine livers. Biomedical optics express 2(7), 1877 (2011).

[90] I. Feder, M. S. WrÃşbel, H. Duadi, D. Fixler, and M. Jedrzejewska-Szczerska. Full scattering profile of circular optical phantoms mimicking biological tissue. In Proc. of SPIE Vol, vol. 10077, pp. 1007718–1 (2017).

[91] G. Zaccanti, S. Del Bianco, and F. Martelli. Measurements of optical properties of high-density media. Applied optics 42(19), 4023 (2003).

[92] F. Martelli, M. Bassani, L. Alianelli, L. Zangheri, and G. Zaccanti. Accuracy of the diffusion equation to describe photon migration through an infinite medium: numerical and experimental investigation. Physics in medicine and biology 45(5), 1359 (2000).

[93] L. Spinelli, M. Botwicz, N. Zolek, M. Kacprzak, D. Milej, P. Sawosz, A. Liebert, U. Weigel, T. Durduran, and F. Foschum. Determination of reference values for optical properties of liquid phantoms based on Intralipid and India ink. Biomedical optics express 5(7), 2037 (2014).

[94] B. Aernouts, E. Zamora-Rojas, R. Van Beers, R. Watte, L. Wang, M. Tsuta, J. Lammertyn, and W. Saeys. Supercontinuum laser based optical characterization of intralipid phantoms in the 500-2250 nm range. Optics express 21(26), 32450 (2013).

[95] J. S. Dam, C. B. Pedersen, T. Dalgaard, P. E. Fabricius, P. Aruna, and S. Andersson-Engels. Fiber-optic probe for noninvasive real-time determination

of tissue optical properties at multiple wavelengths. Applied optics 40(7), 1155 (2001).

[96] S. Ley, M. Stadthalter, D. Link, D. Laqua, and P. Husar. Phantom materials mimicking the optical properties in the near infrared range for non-invasive fetal pulse oximetry. In Engineering in Medicine and Biology Society (EMBC), 2014 36th Annual International Conference of the IEEE, pp. 1432–1435 (IEEE, 2014).

[97] P. Lemaillet, J.-P. Bouchard, and D. W. Allen. Development of traceable measurement of the diffuse optical properties of solid reference standards for biomedical optics at National Institute of Standards and Technology. Applied optics 54(19), 6118 (2015).

[98] L. Wang, S. L. Jacques, and L. Zheng. ConvâĂŤconvolution for responses to a finite diameter photon beam incident on multi-layered tissues. Computer methods and programs in biomedicine 54(3), 141 (1997).

[99] L. Wang, S. L. Jacques, and L. Zheng. MCMLâĂŤMonte Carlo modeling of light transport in multi-layered tissues. Computer methods and programs in biomedicine 47(2), 131 (1995).

[100] P. Lemaillet, J.-P. Bouchard, J. Hwang, and D. W. Allen. Double-integrating-sphere system at the National Institute of Standards and Technology in support of measurement standards for the determination of optical properties of tissue-mimicking phantoms. Journal of biomedical optics 20(12), 121310 (2015).

[101] P. Lemaillet, C. C. Cooksey, Z. H. Levine, A. L. Pintar, J. Hwang, and D. W. Allen. National Institute of Standards and Technology measurement service of the optical properties of biomedical phantoms: Current status. In Proceedings of SPIE the International Society for Optical Engineering, vol. 9700 (NIH Public Access, 2016).

[102] S. T. Flock, M. S. Patterson, B. C. Wilson, and D. R. Wyman. Monte Carlo modeling of light propagation in highly scattering tissues. I. Model predictions and comparison with diffusion theory. IEEE Transactions on Biomedical Engineering 36(12), 1162 (1989).

[103] S. T. Flock, S. L. Jacques, B. C. Wilson, W. M. Star, and M. J. van Gemert. Optical properties of Intralipid: a phantom medium for light propagation studies. Lasers in surgery and medicine 12(5), 510 (1992).

[104] Z. Song, K. Dong, X. H. Hu, and J. Q. Lu. Monte Carlo simulation of converging laser beams propagating in biological materials. Applied optics 38(13), 2944 (1999).

[105] Y. Du, X. H. Hu, M. Cariveau, X. Ma, G. W. Kalmus, and J. Q. Lu. Optical properties of porcine skin dermis between 900 nm and 1500 nm. Physics in Medicine and biology 46(1), 167 (2001).

[106] D. D. Royston, R. S. Poston, and S. A. Prahl. Optical properties of scattering and absorbing materials used in the development of optical phantoms at 1064 nm. Journal of biomedical optics 1(1), 110 (1996).

[107] V. G. Peters, D. Wyman, M. Patterson, and G. Frank. Optical properties of normal and diseased human breast tissues in the visible and near infrared. Physics in Medicine and Biology 35(9), 1317 (1990).

[108] T. L. Troy, D. L. Page, and E. M. Sevick-Muraca. Optical properties of normal and diseased breast tissues: prognosis for optical mammography. Journal of Biomedical Optics 1(3), 342 (1996).

[109] Y. and El-Sharkawy. Breast cancer detection by determination of optical properties of non-malignant and malignant breast tissues. J Cancer Sci Clin Oncol 3(1), 106 (2016).

[110] R. C. Haskell, L. O. Svaasand, T.-T. Tsay, T.-C. Feng, B. J. Tromberg, and M. S. McAdams. Boundary conditions for the diffusion equation in radiative transfer. JOSA A 11(10), 2727 (1994).

[111] D. K. Sardar, R. M. Yow, G.-Y. Swanland, R. J. Thomas, and A. T. Tsin. Optical properties of ocular tissues in the near infrared region. Tech. rep., AIR FORCE RESEARCH LAB BROOKS CITY-BASE TX (2006).

[112] B. J. Tromberg, O. Coquoz, J. B. Fishkin, T. Pham, E. R. Anderson, J. Butler, M. Cahn, J. D. Gross, V. Venugopalan, and D. Pham. NonâĂŞinvasive measurements of breast tissue optical properties using frequencyâĂŞdomain photon migration. Philosophical Transactions of the Royal Society of London B: Biological Sciences 352(1354), 661 (1997).

[113] T. Durduran, J. P. Culver, L. Zubkov, R. Choe, M. J. Holboke, B. Chance, and A. G. Yodh. Bulk optical properties of normal female breasts measured with a frequency domain clinical imager. Photonics West 2001, SPIE 4250, 65 (2001).

[114] T. Durduran, R. Choe, J. P. Culver, L. Zubkov, M. J. Holboke, J. Giammarco, B. Chance, and A. G. Yodh. Bulk optical properties of healthy female breast tissue. Physics in medicine and biology 47(16), 2847 (2002).

[115] J. L. Sandell and T. C. Zhu. A review of in-vivo optical properties of human tissues and its impact on PDT. Journal of biophotonics 4(11-12), 773 (2011).

[116] R. J. Epstein. Does the breast cancer dollar make sense? European Journal of Cancer 28(2-3), 486 (1992).

[117] B. B. Das, K. M. Yoo, and R. R. Alfano. Ultrafast time-gated imaging in thick tissues: a step toward optical mammography. Optics letters 18(13), 1092 (1993).

[118] J. C. Hebden, R. A. Kruger, and K. S. Wong. Time resolved imaging through a highly scattering medium. Applied optics 30(7), 788 (1991).

[119] H. Jiang, B. W. Pogue, M. S. Patterson, K. D. Paulsen, and U. L. Osterberg. Simultaneous reconstruction of optical absorption and scattering maps in turbid media from near-infrared frequency-domain data. Optics letters 20(20), 2128 (1995).

[120] E. M. Sevick, J. K. Frisoli, C. L. Burch, and J. R. Lakowicz. Localization of absorbers in scattering media by use of frequency-domain measurements of time-dependent photon migration. Applied optics 33(16), 3562 (1994).

[121] F. W. Rost. Fluorescence microscopy, vol. 2 (Cambridge University Press, 1992).

[122] G. ElMasry, M. Kamruzzaman, D.-W. Sun, and P. Allen. Principles and applications of hyperspectral imaging in quality evaluation of agro-food products: a review. Critical reviews in food science and nutrition 52(11), 999 (2012).

[123] A. Bray, R. Chapman, and T. Plakhotnik. Accurate measurements of the raman scattering coefficient and the depolarization ratio in liquid water. Applied optics 52(11), 2503 (2013).

[124] Y.-C. Tseng, Y.-C. Cheng, Y.-C. Lee, D.-L. Ma, B.-Y. Yu, B.-C. Lin, and H.-L. Chen. Using visible laser-based raman spectroscopy to identify the surface polarity of silicon carbide. The Journal of Physical Chemistry C 120(32), 18228 (2016).

[125] Y. Xu. Optical Soliton Propagation in Metamaterials; Evolutionary Pattern Formation for Competing Populations Under Seasonal Forcing. Ph.D. thesis, Delaware State University (2017).

[126] A. Rehman, S. Anwar, S. Firdous, M. Ahmed, R. Rasheed, and M. Nawaz. Dengue blood analysis by raman spectroscopy. Laser Physics 22(6), 1085 (2012).

[127] V. V. Tuchin. Tissue Optics and Photonics: Light-Tissue Interaction II. Journal of Biomedical Photonics & Engineering 2(3), 030201 (2016).

[128] D. H. and Goldstein. Mueller matrix dual-rotating retarder polarimeter. Applied optics 31(31), 6676 (1992).

[129] J. L. and Pezzaniti. Mueller matrix imaging polarimetry an overview .

[130] R. A. Chipman, E. A. Sornsin, and J. L. Pezzaniti. Mueller matrix imaging polarimetry an overview. In International Symposium on Polarization Analysis and Applications to Device Technology, pp. 5–12 (International Society for Optics and Photonics, 1996).

[131] M.-R. Antonelli, A. Pierangelo, T. Novikova, P. Validire, A. Benali, B. Gayet, and A. De Martino. Mueller matrix imaging of human colon tissue for cancer diagnostics: how monte carlo modeling can help in the interpretation of experimental data. Optics express 18(10), 10200 (2010).

[132] W. Wang, L. G. Lim, S. Srivastava, J. BokYan So, A. Shabbir, and Q. Liu. Investigation on the potential of mueller matrix imaging for digital staining. Journal of biophotonics 9(4), 364 (2016).

[133] N. F. Boyd, L. J. Martin, M. J. Yaffe, and S. Minkin. Mammographic density and breast cancer risk current understanding and future prospects. Breast Cancer Research 13(6), 223 (2011).

[134] P. A. Carney, C. J. Kasales, A. N. Tosteson, J. E. Weiss, M. E. Goodrich, S. P. Poplack, W. S. Wells, and L. Titus-Ernstoff. Likelihood of additional work-up among women undergoing routine screening mammography the impact of age, breast density, and hormone therapy use. Preventive medicine 39(1), 48 (2004).

[135] H. T. Le Petross and M. K. Shetty. Magnetic resonance imaging and breast ultrasonography as an adjunct to mammographic screening in high-risk patients. In Seminars in Ultrasound, CT and MRI, vol. 32, pp. 266–272 (Elsevier, 2011).

[136] V. V. Tuchin. Tissue optics and photonics: biological tissue structures. Journal of Biomedical Photonics & Engineering 1(1) (2015).

[137] N. P. O. P. line. Uniform source integrating spheres models 70481 & 70439 (2018). URL https://www.newport.com/f/flange-mount-integrating-spheres.

[138] V. V. Tuchin. Tissue optics and photonics: light-tissue interaction. Journal of Biomedical Photonics & Engineering 1(2) (2015).

[139] V. V. Tuchin. Tissue optics and photonics: light-tissue interaction. Journal of Biomedical Photonics & Engineering 1(2) (2015).

[140] G. Lu, X. Qin, D. Wang, Z. G. Chen, and B. Fei. Estimation of tissue optical parameters with hyperspectral imaging and spectral unmixing. In Proceedings of SPIE the International Society for Optical Engineering, vol. 9417 (NIH Public Access, 2015).

[141] P. S. Thenkabail and J. G. Lyon. Hyperspectral remote sensing of vegetation (CRC Press, 2016).

[142] D. Bannon. Hyperspectral imaging: Cubes and slices. Nature photonics 3(11), 627 (2009).

[143] A. K. Tilling, G. O Leary, J. G. Ferwerda, S. D. Jones, G. Fitzgerald, and R. Belford. Remote sensing to detect nitrogen and water stress in wheat. The Australian Society of Agronomy 17 (2006).

[144] F. M. Lacar, M. M. Lewis, and I. T. Grierson. Use of hyperspectral imagery for mapping grape varieties in the Barossa Valley, South Australia. In Geoscience and Remote Sensing Symposium, 2001. IGARSS'01. IEEE 2001 International, vol. 6, pp. 2875–2877 (IEEE, 2001).

[145] J. F. Shanahan, J. S. Schepers, D. D. Francis, G. E. Varvel, W. W. Wilhelm, J. M. Tringe, M. R. Schlemmer, and D. J. Major. Use of remote-sensing imagery to estimate corn grain yield. Agronomy Journal 93(3), 583 (2001).

[146] H. Li, W. Liu, B. Dong, J. V. Kaluzny, A. A. Fawzi, and H. F. Zhang. Snapshot hyperspectral retinal imaging using compact spectral resolving detector array. Journal of biophotonics 10(6-7), 830 (2017).

[147] A. M. Shahidi, S. R. Patel, J. G. Flanagan, and C. Hudson. Regional variation in human retinal vessel oxygen saturation. Experimental eye research 113, 143 (2013).

[148] A. Dacal-Nieto, A. Formella, P. Carrion, E. Vazquez-Fernandez, and M. Fernandez-Delgado. Common scab detection on potatoes using an infrared hyperspectral imaging system. Image Analysis and Processing ICIAP 2011 pp. 303–312 (2011).

[149] G. ElMasry, D.-W. Sun, and P. Allen. Non-destructive determination of water-holding capacity in fresh beef by using NIR hyperspectral imaging. Food Research International 44(9), 2624 (2011).

[150] H. M. A. van der Werff. Knowledge-based remote sensing of complex objects: recognition of spectral and spatial patterns resulting from natural hydrocarbon seepages (Universiteit Utrecht, 2006).

[151] H. Holma. Thermische Hyperspektralbildgebung im langwelligen Infrarot (Photonik, 2011).

[152] L. J. Rickard, R. W. Basedow, E. F. Zalewski, P. R. Silverglate, and M. Landers. HYDICE: An airborne system for hyperspectral imaging. In Imaging Spectrometry of the Terrestrial Environment, vol. 1937, pp. 173–180 (International Society for Optics and Photonics, 1993).

[153] E. K. Hege, D. O'Connell, W. Johnson, S. Basty, and E. L. Dereniak. Hyperspectral imaging for astronomy and space surviellance. In Optical Science and Technology, SPIE's 48th Annual Meeting, pp. 380–391 (International Society for Optics and Photonics, 2004).

[154] B. Rafert, R. G. Sellar, E. Holbert, J. H. Blatt, D. W. Tyler, S. E. Durham, and H. D. Newby. Hyperspectral imaging Fourier transform spectrometers for astronomical and remote sensing observations. In Instrumentation in Astronomy VIII, vol. 2198, pp. 338–350 (International Society for Optics and Photonics, 1994).

[155] C. Fischer and I. Kakoulli. Multispectral and hyperspectral imaging technologies in conservation: current research and potential applications. Studies in Conservation 51(sup1), 3 (2006).

[156] G. Zonios, L. T. Perelman, V. Backman, R. Manoharan, M. Fitzmaurice, J. Van Dam, and M. S. Feld. Diffuse reflectance spectroscopy of human adenomatous colon polyps in vivo. Applied Optics 38(31), 6628 (1999).

[157] M. A. Calin, S. V. Parasca, D. Savastru, and D. Manea. Hyperspectral imaging in the medical field: present and future. Applied Spectroscopy Reviews 49(6), 435 (2014).

[158] S. and Grusche. Basic slit spectroscope reveals three-dimensional scenes through diagonal slices of hyperspectral cubes. Applied optics 53(20), 4594 (2014).

[159] N. Hagen and M. W. Kudenov. Review of snapshot spectral imaging technologies. Optical Engineering 52(9), 090901 (2013).

[160] M. H. Kim. The Three-Dimensional Evolution of Hyperspectral Imaging. In Smart Sensors and Systems, pp. 63–84 (Springer, 2015).

[161] A. Rady, D. Guyer, and R. Lu. Evaluation of sugar content of potatoes using hyperspectral imaging. Food and Bioprocess Technology 8(5), 995 (2015).

[162] X. Zou and J. Zhao. Nondestructive measurement in food and agro-products (Springer, 2015).

[163] G. Di Caprio, D. Schaak, and E. Schonbrun. Hyperspectral fluorescence microfluidic (hfm) microscopy. Biomedical optics express 4(8), 1486 (2013).

[164] A. S. Luthman, S. Dumitru, I. Quiros Gonzalez, J. Joseph, and S. E. Bohndiek. Fluorescence hyperspectral imaging (fhsi) using a spectrally resolved detector array. Journal of Biophotonics (2017).

[165] J. Jia, K. J. Barnard, and K. Hirakawa. Fourier spectral filter array for optimal multispectral imaging. Image Processing, IEEE Transactions on 25(4), 1530 (2016).

[166] R. Lansford, G. Bearman, and S. Fraser. Resolution of multiple green fluorescent protein color variants and dyes using two-photon microscopy and imaging spectroscopy. Journal of Biomedical Optics 6(3), 311 (2001).

[167] C. Yang, J. H. Everitt, M. R. Davis, and C. Mao. A ccd camera-based hyperspectral imaging system for stationary and airborne applications. Geocarto International 18(2), 71 (2003).

[168] R. L. Schuler, P. E. Kish, and C. A. Plese. Preliminary observations on the ability of hyperspectral imaging to provide detection and visualization of bloodstain patterns on black fabrics. Journal of Forensic Sciences 57(6), 1562 (2012).

[169] N. Gupta. Hyperspectral imager development at army research laboratory. In Infrared Technology and Applications XXXIV, vol. 6940, pp. 69401P–69401P–10 (2008).

[170] J. Vila-Frances, J. Calpe-Maravilla, L. Gomez-Chova, and J. Amoros-Lopez. Analysis of acousto-optic tunable filter performance for imaging applications. Optical Engineering 49(11), 113203 (2010).

[171] C. J. Robison, C. Kolanko, T. Bourlai, and J. M. Dawson. Imaging white blood cells using a snapshot hyperspectral imaging system. In Algorithms and Technologies for Multispectral, Hyperspectral, and Ultraspectral Imagery XXI, vol. 9472, p. 44 (International Society for Optics and Photonics, 2015).

[172] B. Corporation. Acousto-optic tunable filter technology (aotf) (1980). URL https://www.brimrose.com/acousto-optic-components.

[173] A. A. Fawzi, N. Lee, J. H. Acton, A. F. Laine, and R. T. Smith. Recovery of macular pigment spectrum in vivo using hyperspectral image analysis. Journal of biomedical optics 16(10) (2011).

[174] J. Hartke and E. L. Dereniak. Snapshot dual-band visible hyperspectral imaging spectrometer. Optical Engineering 46(1) (2007).

[175] I. S. Bowen. The image-slicer, a device for reducing loss of light at slit of stellar spectrograph (Astrophysical Journal 1938). Selected Papers on Instrumentation in Astronomy p. 136 (1993).

[176] R. Sharples, R. Bender, A. Berbel, R. Bennett, N. Bezawada, N. Bouche, D. Bramall, M. Casali, M. Cirasuolo, P. Clark, M. Cliffe, R. Davies, R. Davies, N. Drory, M. Dubbeldam, A. Fairley, G. Finger, R. Genzel, R. Haefner, A. Hess, P. Jeffers, I. Lewis, D. Montgomery, J. Murray, B. Muschielok, N. Schreiber, J. Pirard, S. Ramsay-Howat, P. Rees, J. Richter, D. Robertson, I. Robson, S. Rolt, R. Saglia, J. Schlichter, M. Tecza, S. Todd, M. Wegner, and E. Wiezorrek. Recent progress on the kmos multi-object integral-field spectrograph for eso vlt. vol. 7735 (2010). URL http://search.proquest.com/docview/849466244/.

[177] B. Lantz, G. Aldering, P. Antilogus, C. Bonnaud, L. Capoani, A. Castera, Y. Copin, D. Dubet, E. Gangler, and F. Henault. SNIFS: a wideband integral field spectrograph with microlens arrays. In SPIE Proceedings Series, vol. 5249, pp. 146–155 (2003).

[178] T. Okamoto and I. Yamaguchi. Simultaneous acquisition of spectral image information. Optics Letters 16(16), 1277 (1991).

[179] M. E. Gehm, R. John, D. J. Brady, R. M. Willett, and T. J. Schulz. Single-shot compressive spectral imaging with a dual-disperser architecture. Optics express 15(21), 14013 (2007).

[180] L. Gao, R. T. Kester, N. Hagen, and T. S. Tkaczyk. Snapshot image mapping spectrometer (ims) with high sampling density for hyperspectral microscopy. Optics express 18(14), 14330 (2010).

[181] L. Gao, R. T. Kester, and T. S. Tkaczyk. Compact Image Slicing Spectrometer (ISS) for hyperspectral fluorescence microscopy. Optics express 17(15), 12293 (2009).

[182] M. W. Kudenov, B. Banerjee, V. C. Chan, and E. L. Dereniak. Compact snapshot birefringent imaging fourier transform spectrometer for remote sensing and endoscopy. In Electro-Optical Remote Sensing, Photonic Technologies, and Applications VI, vol. 8542, p. 854224 (International Society for Optics and Photonics, 2012).

[183] M. W. Kudenov and E. L. Dereniak. Compact snapshot birefringent imaging Fourier transform spectrometer. In Proc. SPIE, vol. 7812, pp. 781206–11 (2010).

[184] J. Vervandier and S. Gioux. Single snapshot imaging of optical properties. Biomedical optics express 4(12), 2938 (2013).

[185] J. A. Greenberg, K. Krishnamurthy, and D. Brady. Snapshot molecular imaging using coded energy-sensitive detection. Optics express 21(21), 25480 (2013).

[186] A. M. Locke, D. S. Sabatke, E. L. Dereniak, M. R. Descour, J. P. Garcia, D. Sass, S. Hoffman, J. White, and R. Sampson. A snapshot imaging spectropolarimeter. Tech. rep., Army Tank-Automotive Command Warren Mi (2001).

[187] B. S. Paskalva, M. M. Hayat, W.-Y. Jang, and S. Krishna. A New Approach for Spatio-Spectral Feature Selection for Sensors with Noisy and Overlapping Spectral Bands. In Geoscience and Remote Sensing Symposium, 2008. IGARSS 2008. IEEE International, vol. 5, pp. V–385 (IEEE, 2008).

[188] N. Akhtar, F. Shafait, and A. Mian. Sparse spatio-spectral representation for hyperspectral image super-resolution. In European Conference on Computer Vision, pp. 63–78 (Springer, 2014).

[189] S. Livens, K. Pauly, P. Baeck, J. Blommaert, D. Nuyts, J. Zender, and B. Delaure. A Spatio-Spectral Camera For High Resolution Hyperspectral Imaging. International Archives of the Photogrammetry, Remote Sensing & Spatial Information Sciences 42 (2017).

[190] F. Masia, P. Borri, and W. Langbein. Sparse sampling for fast hyperspectral coherent anti-Stokes Raman scattering imaging. Optics express 22(4), 4021 (2014).

[191] P. F. Favreau, C. Hernandez, T. Heaster, D. F. Alvarez, T. C. Rich, P. Prabhat, and S. J. Leavesley. Excitation-scanning hyperspectral imaging microscope. Journal of biomedical optics 19(4), 046010 (2014).

[192] D. M. Haaland, H. D. Jones, M. H. Van Benthem, M. B. Sinclair, D. K. Melgaard, C. L. Stork, M. C. Pedroso, P. Liu, A. R. Brasier, and N. L. Andrews. Hyperspectral confocal fluorescence imaging: exploring alternative multivariate curve resolution approaches. Applied spectroscopy 63(3), 271 (2009).

[193] M. B. Sinclair, D. M. Haaland, J. A. Timlin, and H. D. Jones. Hyperspectral confocal microscope. Applied optics 45(24), 6283 (2006).

[194] K. A. Christensen and M. D. Morris. Hyperspectral Raman microscopic imaging using Powell lens line illumination. Applied spectroscopy 52(9), 1145 (1998).

[195] W. F. Vermaas, J. A. Timlin, H. D. Jones, M. B. Sinclair, L. T. Nieman, S. W. Hamad, D. K. Melgaard, and D. M. Haaland. In vivo hyperspectral confocal fluorescence imaging to determine pigment localization and distribution in cyanobacterial cells. Proceedings of the National Academy of Sciences 105(10), 4050 (2008).

[196] C. Zhang, H. Wu, and J. Li. Fourier transform hyperspectral imaging polarimeter for remote sensing. Optical Engineering 50(6), 066201 (2011).

[197] A. El-Saba, M. S. Alam, and W. A. Sakla. Pattern recognition via multispectral, hyperspectral, and polarization-based imaging. In SPIE Defense, Security, and

Sensing, pp. 76961M–76961M (International Society for Optics and Photonics, 2010).

[198] E. Laux, C. Genet, T. Skauli, and T. W. Ebbesen. Plasmonic photon sorters for spectral and polarimetric imaging. Nature Photonics 2(3), 161 (2008).

[199] F. J. Iannarilli, S. H. Jones, H. E. Scott, and P. L. Kebabian. Polarimetric-spectral intensity modulation (P-SIM): enabling simultaneous hyperspectral and polarimetric imaging. In Infrared technology and applications XXV, vol. 3698, pp. 474–482 (International Society for Optics and Photonics, 1999).

[200] T. Mu, C. Zhang, C. Jia, and W. Ren. Static hyperspectral imaging polarimeter for full linear Stokes parameters. Optics express 20(16), 18194 (2012).

[201] Y. Hirohara, Y. OKawa, T. Mihashi, T. Yamaguchi, N. Nakazawa, Y. Tsuruga, H. Aoki, N. Maeda, I. Uchida, and T. Fujikado. Validity of retinal oxygen saturation analysis: Hyperspectral imaging in visible wavelength with fundus camera and liquid crystal wavelength tunable filter. Optical review 14(3), 151 (2007).

[202] D. Cohen, M. Arnoldussen, G. Bearman, and W. S. Grundfest. The use of spectral imaging for the diagnosis of retinal disease. In LEOS 99 IEEE Lasers and Electro-Optics Society 1999 12th Annual Meeting, vol. 1, pp. 220–221 (IEEE, 1999).

[203] B. Khoobehi, J. M. Beach, and H. Kawano. Hyperspectral imaging for measurement of oxygen saturation in the optic nerve head. Investigative ophthalmology & visual science 45(5), 1464 (2004).

[204] V. Nourrit, J. Denniss, M. M. K. Muqit, I. Schiessl, C. Fenerty, P. E. Stanga, and D. B. Henson. High-resolution hyperspectral imaging of the retina with a modified fundus camera. Journal francais dophtalmologie 33(10), 686 (2010).

[205] Y. Ozeki, W. Umemura, Y. Otsuka, S. Satoh, H. Hashimoto, K. Sumimura, N. Nishizawa, K. Fukui, and K. Itoh. High-speed molecular spectral imaging of tissue with stimulated Raman scattering. Nature photonics 6(12), 845 (2012).

[206] D. Fu, J. Zhou, W. S. Zhu, P. W. Manley, Y. K. Wang, T. Hood, A. Wylie, and X. S. Xie. Imaging the intracellular distribution of tyrosine kinase inhibitors in

living cells with quantitative hyperspectral stimulated Raman scattering. Nature chemistry 6(7), 614 (2014).

[207] J. Qin, M. S. Kim, W. F. Schmidt, B.-K. Cho, Y. Peng, and K. Chao. A line-scan hyperspectral Raman system for spatially offset Raman spectroscopy. Journal of Raman Spectroscopy 47(4), 437 (2016).

[208] D. Zhang, P. Wang, M. N. Slipchenko, D. Ben-Amotz, A. M. Weiner, and J.-X. Cheng. Quantitative vibrational imaging by hyperspectral stimulated Raman scattering microscopy and multivariate curve resolution analysis. Analytical chemistry 85(1), 98 (2013).

[209] S. Begin, B. Burgoyne, V. Mercier, A. Villeneuve, R. Vallee, and D. Cote. Coherent anti-Stokes Raman scattering hyperspectral tissue imaging with a wavelength-swept system. Biomedical optics express 2(5), 1296 (2011).

[210] S. L. Best, A. Thapa, M. J. Holzer, N. Jackson, S. A. Mir, J. A. Cadeddu, and K. J. Zuzak. Minimal arterial in-flow protects renal oxygenation and function during porcine partial nephrectomy: confirmation by hyperspectral imaging. Urology 78(4), 961 (2011).

[211] K. J. Zuzak, S. C. Naik, G. Alexandrakis, D. Hawkins, K. Behbehani, and E. Livingston. Intraoperative bile duct visualization using near-infrared hyperspectral video imaging. The American Journal of Surgery 195(4), 491 (2008).

[212] K. J. Zuzak, S. C. Naik, G. Alexandrakis, D. Hawkins, K. Behbehani, and E. H. Livingston. Characterization of a near-infrared laparoscopic hyperspectral imaging system for minimally invasive surgery. Analytical chemistry 79(12), 4709 (2007).

[213] D. Fu, G. Holtom, C. Freudiger, X. Zhang, and X. S. Xie. Fast hyperspectral imaging with stimulated raman scattering by chirped femtosecond lasers. The journal of physical chemistry. B 117(16), 4634 (2013).

[214] G. Mooradian, M. Weiderhold, A. E. Dabiri, and C. Coyle. Hyperspectral imaging methods and apparatus for non-invasive diagnosis of tissue for cancer (1998).

[215] A. U. Velten, J. G. White, T. R. Mackie, and K. W. Eliceiri. Hyperspectral multi-point confocal microscope. In CLEO: Applications and Technology, pp. AW1I–2 (Optical Society of America, 2013).

[216] M. B. Sinclair, J. A. Timlin, D. M. Haaland, and M. Werner-Washburne. Design, construction, characterization, and application of a hyperspectral microarray scanner. Applied optics 43(10), 2079 (2004).

[217] E. S. Oh, C. Heo, J. S. Kim, M. Suh, Y. H. Lee, and J.-M. Kim. Hyperspectral fluorescence imaging for cellular iron mapping in the in vitro model of ParkinsonâĂŹs disease. Journal of biomedical optics 19(5), 051207 (2014).

[218] G. S. Verebes, M. Melchiorre, A. Garcia-Leis, C. Ferreri, C. Marzetti, and A. Torreggiani. Hyperspectral enhanced dark field microscopy for imaging blood cells. Journal of biophotonics 6(11-12), 960 (2013).

[219] S. Kiyotoki, J. Nishikawa, T. Okamoto, K. Hamabe, M. Saito, A. Goto, Y. Fujita, Y. Hamamoto, Y. Takeuchi, and S. Satori. New method for detection of gastric cancer by hyperspectral imaging: a pilot study. Journal of biomedical optics 18(2), 026010 (2013).

[220] Y. G. Patel, M. Rajadhyaksha, and C. A. DiMarzio. Optimization of pupil design for point-scanning and line-scanning confocal microscopy. Biomedical optics express 2(8), 2231 (2011).

[221] N. Billecke, G. Rago, M. Bosma, G. Eijkel, A. Gemmink, P. Leproux, G. Huss, P. Schrauwen, M. K. Hesselink, and M. Bonn. Chemical imaging of lipid droplets in muscle tissues using hyperspectral coherent Raman microscopy. Histochemistry and cell biology 141(3), 263 (2014).

[222] M. Miljkovic, T. Chernenko, M. J. Romeo, B. Bird, C. Matthaus, and M. Diem. Label-free imaging of human cells: algorithms for image reconstruction of Raman hyperspectral datasets. Analyst 135(8), 2002 (2010).

[223] J. Xu, B. Guo, K. K. Wong, and K. K. M. Tsia. Broadband hyperspectral coherent anti-Stokes Raman scattering microscopy for stain-free histological imaging with principal component analysis. In Proceedings of SPIE-International Society

for Optical Engineering (SPIE-International Society for Optical Engineering. The Journal's web site is located at http://spie. org/x1848. xml? WT. svl= mddp2, 2014).

[224] F. Vasefi, N. MacKinnon, R. B. Saager, A. J. Durkin, R. Chave, E. H. Lindsley, and D. L. Farkas. Polarization-sensitive hyperspectral imaging in vivo: a multimode dermoscope for skin analysis. Scientific reports 4 (2014).

[225] T. Vo-Dinh. A hyperspectral imaging system for in vivo optical diagnostics. IEEE Engineering in Medicine and Biology Magazine 23(5), 40 (2004).

[226] G. Lu and B. Fei. Medical hyperspectral imaging: a review. Journal of biomedical optics 19(1), 010901 (2014).

[227] R. A. Schultz, T. Nielsen, J. R. Zavaleta, R. Ruch, R. Wyatt, and H. R. Garner. Hyperspectral imaging: a novel approach for microscopic analysis. Cytometry Part A 43(4), 239 (2001).

[228] V. Studer, J. Bobin, M. Chahid, H. S. Mousavi, E. Candes, and M. Dahan. Compressive fluorescence microscopy for biological and hyperspectral imaging. Proceedings of the National Academy of Sciences 109(26), E1679 (2012).

[229] P. Constantinou, R. S. Dacosta, and B. C. Wilson. Extending immunofluorescence detection limits in whole paraffin-embedded formalin fixed tissues using hyperspectral confocal fluorescence imaging. Journal of microscopy 234(2), 137 (2009).

[230] M. E. Martin, M. Wabuyele, M. Panjehpour, B. Overholt, R. DeNovo, S. Kennel, G. Cunningham, and T. Vo-Dinh. An aotf-based dual-modality hyperspectral imaging system (dmhsi) capable of simultaneous fluorescence and reflectance imaging. Medical Engineering and Physics 28(2), 149 (2006).

[231] P. A. Bautista and Y. Yagi. Digital simulation of staining in histopathology multispectral images: enhancement and linear transformation of spectral transmittance. Journal of Biomedical Optics 17(5), 056013 (2012).

[232] D. G. Ferris, R. A. Lawhead, E. D. Dickman, N. Holtzapple, J. A. Miller, S. Grogan, S. Bambot, A. Agrawal, and M. L. Faupel. Multimodal hyperspectral imaging for the noninvasive diagnosis of cervical neoplasia. Journal of Lower Genital Tract Disease 5(2), 65 (2001).

[233] J. M. Benavides, S. Chang, S. Y. Park, R. Richards-Kortum, N. Mackinnon, C. MacAulay, A. Milbourne, A. Malpica, and M. Follen. Multispectral digital colposcopy for in vivo detection of cervical cancer. Optics express 11(10), 1223 (2003).

[234] G. Zavattini, S. Vecchi, G. Mitchell, U. Weisser, R. M. Leahy, B. J. Pichler, D. J. Smith, and S. R. Cherry. A hyperspectral fluorescence system for 3d in vivo optical imaging. Physics in Medicine & Biology 51(8), 2029 (2006).

[235] A. Rehman, A. Anwer, M. Gosnell, S. Mahbub, G. Liu, and E. Goldys. Fluorescence quenching of free and bound nadh in hela cells determined by hyperspectral imaging and unmixing of cell autofluorescence. Biomedical Optics Express 8(3), 1488 (2017).

[236] M. E. Gosnell, A. G. Anwer, J. C. Cassano, C. M. Sue, and E. M. Goldys. Functional hyperspectral imaging captures subtle details of cell metabolism in olfactory neurosphere cells, disease-specific models of neurodegenerative disorders. Biochimica et Biophysica Acta (BBA)-Molecular Cell Research 1863(1), 56 (2016).

[237] M. E. Gosnell, A. G. Anwer, J. C. Cassano, C. M. Sue, S. B. Mahbub, S. M. Pernichery, D. W. Inglis, A. Nadort, P. P. Adhikary, J. A. Jazayeri, et al. Noninvasive detection and monitoring of biochemistry in cells and tissues by decomposing autofluorescence. In Asia Communications and Photonics Conference, pp. AS3I–1 (Optical Society of America, 2016).

[238] S. G. Kong, M. E. Martin, and T. Vo-Dinh. Hyperspectral fluorescence imaging for mouse skin tumor detection. Etri Journal 28(6), 770 (2006).

[239] Z. Liu, S. Ma, Y. Ji, L. Liu, J. Guo, and Y. He. Parallel scan hyperspectral fluorescence imaging system and biomedical application for microarrays. In Journal of Physics: Conference Series, vol. 277, p. 012023 (IOP Publishing, 2011).

[240] A. S. Luthman, S. Dumitru, I. Quiros-Gonzalez, J. Joseph, and S. E. Bohndiek. Fluorescence hyperspectral imaging (fhsi) using a spectrally resolved detector array. Journal of biophotonics 10(6-7), 840 (2017).

[241] C.-I. Chang. Hyperspectral imaging: techniques for spectral detection and classification, vol. 1 (Springer Science & Business Media, 2003).

[242] B. Park and R. Lu. Hyperspectral imaging technology in food and agriculture (Springer, 2015).

[243] C.-I. Chang. Hyperspectral data processing: algorithm design and analysis (John Wiley & Sons, 2013).

[244] J. B. Adams, M. O. Smith, and P. E. Johnson. Spectral mixture modeling: A new analysis of rock and soil types at the Viking Lander 1 site. Journal of Geophysical Research: Solid Earth 91(B8), 8098 (1986).

[245] N. Keshava and J. F. Mustard. Spectral unmixing. IEEE signal processing magazine 19(1), 44 (2002).

[246] A. Plaza, Q. Du, J. M. Bioucas-Dias, X. Jia, and F. A. Kruse. Foreword to the special issue on spectral unmixing of remotely sensed data. IEEE Transactions on Geoscience and Remote Sensing 49(11), 4103 (2011).

[247] R. L. King, C. Ruffin, F. E. LaMastus, and D. R. Shaw. The analysis of hyperspectral data using Savitzky-Golay filtering-practical issues. 2. In Geoscience and Remote Sensing Symposium, 1999. IGARSS'99 Proceedings. IEEE 1999 International, vol. 1, pp. 398–400 (IEEE, 1999).

[248] W. H. Press, S. A. Teukolsky, W. T. Vetterling, and B. P. Flannery. Numerical recipes. Cambridge University, Cambridge (1988).

[249] Y. Ozaki, W. F. McClure, and A. A. Christy. Near-infrared spectroscopy in food science and technology (John Wiley & Sons, 2006).

[250] G. P. Abousleman, E. Gifford, and B. R. Hunt. Enhancement and compression techniques for hyperspectral data. Optical Engineering 33(8), 2562 (1994).

[251] S. Yoon, K. Lawrence, G. Siragusa, J. Line, B. Park, and P. Feldner. Hyperspectral reflectance imaging for detecting a foodborne pathogen: Campylobacter. Transactions of the ASABE 52(2), 651 (2009).

[252] S.-C. Yoon, W. R. Windham, S. R. Ladely, J. W. Heitschmidt, K. C. Lawrence, B. Park, N. Narang, and W. C. Cray. Hyperspectral imaging for differentiating colonies of non-0157 shiga-toxin producing escherichia coli (stec) serogroups on spread plates of pure cultures. Journal of Near Infrared Spectroscopy 21(2), 81 (2013).

[253] Y. Guan, Q. Li, Y. Wang, H. Liu, and Z. Zhu. Pathological leucocyte segmentation algorithm based on hyperspectral imaging technique. Optical Engineering 51(5), 053202 (2012).

[254] F. Tsai and W. Philpot. Derivative analysis of hyperspectral data for detecting spectral features. In Geoscience and Remote Sensing, 1997. IGARSS'97. Remote Sensing-A Scientific Vision for Sustainable Development., 1997 IEEE International, vol. 3, pp. 1243–1245 (IEEE, 1997).

[255] C. Ruffin and R. L. King. The analysis of hyperspectral data using Savitzky-Golay filtering-theoretical basis. 1. In Geoscience and Remote Sensing Symposium, 1999. IGARSS'99 Proceedings. IEEE 1999 International, vol. 2, pp. 756–758 (IEEE, 1999).

[256] B. Somers and G. P. Asner. Hyperspectral time series analysis of native and invasive species in Hawaiian rainforests. Remote Sensing 4(9), 2510 (2012).

[257] M. Vidal and J. M. Amigo. Pre-processing of hyperspectral images. Essential steps before image analysis. Chemometrics and Intelligent Laboratory Systems 117, 138 (2012).

[258] R. Koprowski. Hyperspectral imaging in medicine: image pre-processing problems and solutions in Matlab. Journal of biophotonics 8(11-12), 935 (2015).

[259] R. Koprowski, S. Wilczynski, Z. Wrobel, and B. Bnlonska-Fajfrowska. Calibration and segmentation of skin areas in hyperspectral imaging for the needs of dermatology. Biomedical engineering online 13(1), 113 (2014).

[260] R. Koprowski, S. Wilczynski, Z. Wrobel, S. Kasperczyk, and B. Blonska-Fajfrowska. Automatic method for the dermatological diagnosis of selected hand skin features in hyperspectral imaging. Biomedical engineering online 13(1), 47 (2014).

[261] A. Plaza, J. A. Benediktsson, J. W. Boardman, J. Brazile, L. Bruzzone, G. Camps-Valls, J. Chanussot, M. Fauvel, P. Gamba, and A. Gualtieri. Recent advances in techniques for hyperspectral image processing. Remote sensing of environment 113, S110 (2009).

[262] F. Mendoza, R. Lu, D. Ariana, H. Cen, and B. Bailey. Integrated spectral and image analysis of hyperspectral scattering data for prediction of apple fruit firmness and soluble solids content. Postharvest Biology and Technology 62(2), 149 (2011).

[263] Z. Tu and S.-C. Zhu. Image segmentation by data-driven Markov chain Monte Carlo. IEEE Transactions on pattern analysis and machine intelligence 24(5), 657 (2002).

[264] D. Fu and X. S. Xie. Reliable cell segmentation based on spectral phasor analysis of hyperspectral stimulated Raman scattering imaging data. Analytical chemistry 86(9), 4115 (2014).

[265] M. Fauvel, Y. Tarabalka, J. A. Benediktsson, J. Chanussot, and J. C. Tilton. Advances in spectral-spatial classification of hyperspectral images. Proceedings of the IEEE 101(3), 652 (2013).

[266] K. Pearson. LIII. On lines and planes of closest fit to systems of points in space. The London, Edinburgh, and Dublin Philosophical Magazine and Journal of Science 2(11), 559 (1901).

[267] S. Wold, M. Sjostrom, and L. Eriksson. PLS-regression: a basic tool of chemometrics. Chemometrics and intelligent laboratory systems 58(2), 109 (2001).

[268] B. Scholkopf, A. Smola, and K.-R. Muller. Nonlinear component analysis as a kernel eigenvalue problem. Neural computation 10(5), 1299 (1998).

[269] P. Comon. Independent component analysis, a new concept? Signal processing 36(3), 287 (1994).

[270] A. A. Nielsen. Kernel maximum autocorrelation factor and minimum noise fraction transformations. IEEE Transactions on Image Processing 20(3), 612 (2011).

[271] P. M. Narendra and K. Fukunaga. A branch and bound algorithm for feature subset selection. IEEE Transactions on Computers 9(C-26), 917 (1977).

[272] I. Tsamardinos, L. E. Brown, and C. F. Aliferis. The max-min hill-climbing Bayesian network structure learning algorithm. Machine learning 65(1), 31 (2006).

[273] M. Z. Coban and R. M. Mersereau. A fast exhaustive search algorithm for rate-constrained motion estimation. IEEE Transactions on Image Processing 7(5), 769 (1998).

[274] D. Ververidis and C. Kotropoulos. Emotional speech classification using Gaussian mixture models and the sequential floating forward selection algorithm. In Multimedia and Expo, 2005. ICME 2005. IEEE International Conference on, pp. 1500–1503 (IEEE, 2005).

[275] J. Kittler. Feature selection and extraction. Handbook of pattern recognition and image processing pp. 59–83 (1986).

[276] P. Pudil, J. Novovicova, and J. Kittler. Floating search methods in feature selection. Pattern recognition letters 15(11), 1119 (1994).

[277] L. Sint and D. de Champeaux. An improved bidirectional heuristic search algorithm. Journal of the ACM (JACM) 24(2), 177 (1977).

[278] J. H. Friedman and J. W. Tukey. A projection pursuit algorithm for exploratory data analysis. IEEE Transactions on computers 100(9), 881 (19741).

[279] Y. Saeys, I. Inza, and P. Larranaga. A review of feature selection techniques in bioinformatics. bioinformatics 23(19), 2507 (2007).

[280] L. C. Molina, L. Belanche, and A. Nebot. Feature selection algorithms a survey and experimental evaluation. In Data Mining, 2002. ICDM 2003 Proceedings 2002 IEEE International Conference on, pp. 306–313 (IEEE, 2002).

[281] M. F. Akay. Support vector machines combined with feature selection for breast cancer diagnosis. Expert systems with applications 36(2), 3240 (2009).

[282] M. A. Hearst, S. T. Dumais, E. Osuna, J. Platt, and B. Scholkopf. Support vector machines. IEEE Intelligent Systems and their applications 13(4), 18 (1998).

[283] S.-C. Wang. Artificial neural network. In Interdisciplinary computing in java programming, pp. 81–100 (Springer, 2003).

[284] C.-I. Chang. Spectral information divergence for hyperspectral image analysis. In Geoscience and Remote Sensing Symposium, 1999. IGARSS'99 Proceedings. IEEE 1999 International, vol. 1, pp. 509–511 (IEEE, 1999).

[285] B. Park, W. R. Windham, K. C. Lawrence, and D. P. Smith. Contaminant classification of poultry hyperspectral imagery using a spectral angle mapper algorithm. Biosystems Engineering 96(3), 323 (2007).

[286] Z. Q. John Lu. The elements of statistical learning: data mining, inference, and prediction. Journal of the Royal Statistical Society: Series A (Statistics in Society) 173(3), 693 (2010).

[287] S. Mika, G. Ratsch, J. Weston, B. Scholkopf, and K.-R. Mullers. Fisher discriminant analysis with kernels. In Neural Networks for Signal Processing IX, 1999. Proceedings of the 1999 IEEE Signal Processing Society Workshop., pp. 41–48 (IEEE, 1999).

[288] J. Peng, D. R. Heisterkamp, and H. K. Dai. LDA/SVM driven nearest neighbor classification. In Computer Vision and Pattern Recognition, 2001. CVPR 2001. Proceedings of the 2001 IEEE Computer Society Conference on, vol. 1, pp. I–I (IEEE, 2001).

[289] K. Masood, N. M. Rajpoot, H. A. Qureshi, and K. Rajpoot. Hyperspectral texture analysis for colon tissue biopsy classification (2007).

[290] S. G. Kong, Z. Du, M. Martin, and T. Vo-Dinh. Hyperspectral fluorescence image analysis for use in medical diagnostics. In Proc. SPIE, vol. 5692, pp. 21–28 (2005).

[291] U. R. Acharya, E. Y.-K. Ng, J.-H. Tan, and S. V. Sree. Thermography based breast cancer detection using texture features and support vector machine. Journal of medical systems 36(3), 1503 (2012).

[292] H.-L. Chen, B. Yang, J. Liu, and D.-Y. Liu. A support vector machine classifier with rough set-based feature selection for breast cancer diagnosis. Expert Systems with Applications 38(7), 9014 (2011).

[293] T. S. Furey, N. Cristianini, N. Duffy, D. W. Bednarski, M. Schummer, and D. Haussler. Support vector machine classification and validation of cancer tissue samples using microarray expression data. Bioinformatics 16(10), 906 (2000).

[294] I. Guyon, J. Weston, S. Barnhill, and V. Vapnik. Gene selection for cancer classification using support vector machines. Machine learning 46(1), 389 (2002).

[295] Y. Mao, X. Zhao, S. Wang, and Y. Cheng. Urinary nucleosides based potential biomarker selection by support vector machine for bladder cancer recognition. Analytica chimica acta 598(1), 34 (2007).

[296] S. Li, Y. Zhang, J. Xu, L. Li, Q. Zeng, L. Lin, Z. Guo, Z. Liu, H. Xiong, and S. Liu. Noninvasive prostate cancer screening based on serum surface-enhanced Raman spectroscopy and support vector machine. Applied Physics Letters 105(9), 091104 (2014).

[297] D. Lu and Q. Weng. A survey of image classification methods and techniques for improving classification performance. International journal of Remote sensing 28(5), 823 (2007).

[298] S. S. Nath, G. Mishra, J. Kar, S. Chakraborty, and N. Dey. A survey of image classification methods and techniques. In Control, Instrumentation, Communication and Computational Technologies (ICCICCT), 2014 International Conference on, pp. 554–557 (IEEE, 2014).

[299] V. Slavkovikj, S. Verstockt, W. De Neve, S. Van Hoecke, and R. Van de Walle. Hyperspectral image classification with convolutional neural networks. In Proceedings of the 23rd ACM international conference on Multimedia, pp. 1159–1162 (ACM, 2015).

[300] Q. Wang, J. Wang, M. Zhou, Q. Li, and Y. Wang. Spectral-spatial feature-based neural network method for acute lymphoblastic leukemia cell identification via microscopic hyperspectral imaging technology. Biomedical Optics Express 8(6), 3017 (2017).

[301] R. Jolivot, P. Vabres, and F. Marzani. Reconstruction of hyperspectral cutaneous data from an artificial neural network-based multispectral imaging system. Computerized medical imaging and graphics 35(2), 85 (2011).

[302] F. Ratle, G. Camps-Valls, and J. Weston. Semisupervised neural networks for efficient hyperspectral image classification. IEEE Transactions on Geoscience and Remote Sensing 48(5), 2271 (2010).

[303] A. T. Harris. Spectral mapping tools from the earth sciences applied to spectral microscopy data. Cytometry Part A 69(8), 872 (2006).

[304] P. Gong and A. Zhang. Noise effect on linear spectral unmixing. Geographic information sciences 5(1), 52 (1999).

[305] C. M. Morshead, B. A. Reynolds, C. G. Craig, M. W. McBurney, W. A. Staines, D. Morassutti, S. Weiss, and D. van der Kooy. Neural stem cells in the adult mammalian forebrain: a relatively quiescent subpopulation of subependymal cells. Neuron 13(5), 1071 (1994).

[306] G. Winter. xia2: an expert system for macromolecular crystallography data reduction. Journal of applied crystallography 43(1), 186 (2010).

[307] L. Gao and R. T. Smith. Optical hyperspectral imaging in microscopy and spectroscopyâĂŞa review of data acquisition. Journal of biophotonics 8(6), 441 (2015).

[308] H. Akbari, L. V. Halig, D. M. Schuster, A. Osunkoya, V. Master, P. T. Nieh, G. Z. Chen, and B. Fei. Hyperspectral imaging and quantitative analysis for prostate cancer detection. Journal of biomedical optics 17(7), 0760051 (2012).

[309] C.-I. Chang. Hyperspectral data exploitation: theory and applications (John Wiley and Sons, 2007).

[310] M. M. Mehdy, P. Y. Ng, E. F. Shair, N. I. Saleh, and C. Gomes. Artificial Neural Networks in Image Processing for Early Detection of Breast Cancer. Computational and Mathematical Methods in Medicine 2017 (2017).

[311] B. Fei, G. Lu, X. Wang, H. Zhang, J. V. Little, M. R. Patel, C. C. Griffith, M. W. El-Diery, and A. Y. Chen. Label-free reflectance hyperspectral imaging for tumor margin assessment: a pilot study on surgical specimens of cancer patients. Journal of Biomedical Optics 22(8), 086009 (2017).

[312] H. Akbari, K. Uto, Y. Kosugi, K. Kojima, and N. Tanaka. Cancer detection using infrared hyperspectral imaging. Cancer science 102(4), 852 (2011).

[313] D. Hattery, M. Hassan, S. Demos, and A. Gandjbakhche. Hyperspectral imaging of Kaposi's Sarcoma for disease assessment and treatment monitoring. In Applied Imagery Pattern Recognition Workshop, 2002. Proceedings. 31st, pp. 124–130 (IEEE, 2002).

[314] G. Edelman, T. G. v. Leeuwen, and M. C. Aalders. Hyperspectral Imaging for the Age Estimation of Blood Stains at the Crime Scene. Indian Internet Journal of Forensic Medicine & Toxicology 12(1), 22 (2014).

[315] M. Hohmann, A. Douplik, J. Varadhachari, A. Nasution, J. Mudter, M. Neurath, and M. Schmidt. Preliminary results for hyperspectral videoendoscopy diagnostics on the phantoms of normal and abnormal tissues: towards gastrointestinal diagnostics. In European Conference on Biomedical Optics, p. 80872N (Optical Society of America, 2011).

[316] A. Goto, J. Nishikawa, S. Kiyotoki, M. Nakamura, J. Nishimura, T. Okamoto, H. Ogihara, Y. Fujita, Y. Hamamoto, and I. Sakaida. Use of hyperspectral

imaging technology to develop a diagnostic support system for gastric cancer. Journal of biomedical optics 20(1), 016017 (2015).

[317] F.-K. Lu, S. Basu, V. Igras, M. P. Hoang, M. Ji, D. Fu, G. R. Holtom, V. A. Neel, C. W. Freudiger, D. E. Fisher, et al. Label-free dna imaging in vivo with stimulated raman scattering microscopy. Proceedings of the National Academy of Sciences 112(37), 11624 (2015).

[318] D. G. Ferris, R. A. Lawhead, E. D. Dickman, N. Holtzapple, J. A. Miller, S. Grogan, S. Bambot, A. Agrawal, and M. L. Faupel. Multimodal hyperspectral imaging for the noninvasive diagnosis of cervical neoplasia. Journal of Lower Genital Tract Disease 5(2), 65 (2001).

[319] J. M. Benavides, S. Chang, S. Y. Park, R. Richards-Kortum, N. Mackinnon, C. MacAulay, A. Milbourne, A. Malpica, and M. Follen. Multispectral digital colposcopy for in vivo detection of cervical cancer. Optics express 11(10), 1223 (2003).

[320] T. E. Renkoski, K. D. Hatch, and U. Utzinger. Wide-field spectral imaging of human ovary autofluorescence and oncologic diagnosis via previously collected probe data. Journal of biomedical optics 17(3), 0360031 (2012).

[321] B. Prats Mateu, E. Harreither, M. Schosserer, V. Puxbaum, E. Gludovacz, N. Borth, N. Gierlinger, and J. Grillari. Label-free live cell imaging by confocal raman microscopy identifies cho host and producer cell lines. Biotechnology journal 12(1) (2017).

[322] C. H. Camp Jr, Y. J. Lee, J. M. Heddleston, C. M. Hartshorn, A. R. H. Walker, J. N. Rich, J. D. Lathia, and M. T. Cicerone. High-speed coherent raman fingerprint imaging of biological tissues. Nature photonics 8(8), 627 (2014).

[323] K. A. Veselkov, R. Mirnezami, N. Strittmatter, R. D. Goldin, J. Kinross, A. V. Speller, T. Abramov, E. A. Jones, A. Darzi, E. Holmes, et al. Chemo-informatic strategy for imaging mass spectrometry-based hyperspectral profiling of lipid signatures in colorectal cancer. Proceedings of the National Academy of Sciences 111(3), 1216 (2014).

[324] H. Akbari, L. V. Halig, H. Zhang, D. Wang, Z. G. Chen, and B. Fei. Detection of cancer metastasis using a novel macroscopic hyperspectral method. In Proceedings of SPIE, vol. 8317, p. 831711 (NIH Public Access, 2012).

[325] P. D. Beule, D. M. Owen, H. B. Manning, C. B. Talbot, J. Requejo-Isidro, C. Dunsby, J. Mcginty, R. K. Benninger, D. S. Elson, I. Munro, et al. Rapid hyperspectral fluorescence lifetime imaging. Microscopy research and technique 70(5), 481 (2007).

[326] A. Bjorgan, M. Milanic, and L. L. Randeberg. Estimation of skin optical parameters for real-time hyperspectral imaging applications. Journal of biomedical optics 19(6), 066003 (2014).

[327] L. C. Cancio, A. I. Batchinsky, J. R. Mansfield, S. Panasyuk, K. Hetz, D. Martini, B. S. Jordan, B. Tracey, and J. E. Freeman. Hyperspectral imaging: a new approach to the diagnosis of hemorrhagic shock. Journal of Trauma and Acute Care Surgery 60(5), 1087 (2006).

[328] R. J. Cassidy, J. Berger, K. Lee, M. Maggioni, and R. R. Coifman. Analysis of hyperspectral colon tissue images using vocal synthesis models. In Signals, Systems and Computers, 2004. Conference Record of the Thirty-Eighth Asilomar Conference on, vol. 2, pp. 1611–1615 (IEEE, 2004).

[329] C. Wang, W. Zheng, Y. Bu, S. Chang, Q. Tong, S. Zhang, and R. X. Xu. In vivo and in vitro hyperspectral imaging of cervical neoplasia. In Proc. SPIE, vol. 8951, p. 89510M (2014).

[330] A. Lashkari. Full automatic micro calcification detection in mammogram images using artificial neural network and gabor wavelets. In Machine Vision and Image Processing (MVIP), 2010 6th Iranian, pp. 1–7 (IEEE, 2010).

[331] E. A. Mohammed, C. T. Naugler, and B. H. Far. Breast tumor classification using a new owa operator. Expert Systems with Applications 61, 302 (2016).

[332] A. M. Siddiqi, H. Li, F. Faruque, W. Williams, K. Lai, M. Hughson, S. Bigler, J. Beach, and W. Johnson. Use of hyperspectral imaging to distinguish normal, precancerous, and cancerous cells. Cancer Cytopathology 114(1), 13 (2008).

[333] S. Gaudi, R. Meyer, J. Ranka, J. C. Granahan, S. A. Israel, T. R. Yachik, and D. M. Jukic. Hyperspectral imaging of melanocytic lesions. The American Journal of Dermatopathology 36(2), 131 (2014).

[334] G. Lu, L. Halig, D. Wang, Z. G. Chen, and B. Fei. Hyperspectral imaging for cancer surgical margin delineation: registration of hyperspectral and histological images. In Proceedings of SPIE, vol. 9036, p. 90360S (NIH Public Access, 2014).

[335] S. Demos, D. Hattery, M. Hassan, K. Aleman, R. Little, R. Yarchoan, and A. Gandjbakhche. Hyperspectral imaging of functional patterns for disease assessment and treatment monitoring. Tech. rep., Lawrence Livermore National Laboratory (LLNL), Livermore, CA (2003).

[336] A. D. Elliott, L. Gao, A. Ustione, N. Bedard, R. Kester, D. W. Piston, and T. S. Tkaczyk. Real-time hyperspectral fluorescence imaging of pancreatic β-cell dynamics with the image mapping spectrometer. J Cell Sci 125(20), 4833 (2012).

[337] R. T. Kester, N. Bedard, and T. S. Tkaczyk. Image mapping spectrometry: a novel hyperspectral platform for rapid snapshot imaging. In Algorithms and Technologies for Multispectral, Hyperspectral, and Ultraspectral Imagery XVII, vol. 8048, p. 80480J (International Society for Optics and Photonics, 2011).

[338] L. Gao, R. T. Smith, and T. S. Tkaczyk. Snapshot hyperspectral retinal camera with the image mapping spectrometer (ims). Biomedical optics express 3(1), 48 (2012).

[339] D. C. Gray, W. Merigan, J. I. Wolfing, B. P. Gee, J. Porter, A. Dubra, T. H. Twietmeyer, K. Ahmad, R. Tumbar, F. Reinholz, et al. In vivo fluorescence imaging of primate retinal ganglion cells and retinal pigment epithelial cells. Optics Express 14(16), 7144 (2006).

[340] S. R. Patel, J. G. Flanagan, A. M. Shahidi, J.-P. Sylvestre, and C. Hudson. A prototype hyperspectral system with a tunable laser source for retinal vessel imaginga prototype hyperspectral system. Investigative ophthalmology & visual science 54(8), 5163 (2013).

[341] J. Schweizer, J. Hollmach, G. Steiner, L. Knels, R. H. Funk, and E. Koch. Hyperspectral imaging-a new modality for eye diagnostics. Biomedical Engineering/Biomedizinische Technik 57(SI-1 Track-P), 293 (2012).

[342] G. Zamora, P. W. Truitt, S. C. Nemeth, B. Raman, and P. Soliz. Hyperspectral image analysis for ophthalmic applications. In Proc. of SPIE Vol, vol. 5314, p. 139 (2004).

[343] W. R. Johnson, D. W. Wilson, W. Fink, M. Humayun, and G. Bearman. Snapshot hyperspectral imaging in ophthalmology. Journal of biomedical optics 12(1), 014036 (2007).

[344] S. M. Hsu and H.-h. K. Burke. Multisensor fusion with hyperspectral imaging data: detection and classification. Lincoln laboratory journal 14(1), 145 (2003).

[345] Neittaanmaki-Perttu, M. Noora Gronroos, T. Tani, I. Polonen, A. Ranki, O. Saksela, and E. Snellman. Detecting field cancerization using a hyperspectral imaging system. Lasers in surgery and medicine 45(7), 410 (2013).

[346] J. Freeman, F. Downs, L. Marcucci, E. N. Lewis, B. Blume, and J. Rish. Multispectral and hyperspectral imaging: applications for medical and surgical diagnostics. In Engineering in Medicine and Biology Society, 1997. Proceedings of the 19th Annual International Conference of the IEEE, vol. 2, pp. 700–701 (IEEE, 1997).

[347] I. Georgakoudi and K. P. Quinn. Optical imaging using endogenous contrast to assess metabolic state.(report). Annual Review of Biomedical Engineering 14 (2012).

[348] S. Lehrer. The selective quenching of tryptophan fluorescence in proteins by iodide ion: Lysozyme in the presence and absence of substrate. Biochemical and Biophysical Research Communications 29(5), 767 (1967).

[349] S. Lehrer. Corrections - solute perturbation of protein fluorescence. the quenching of the tryptophyl fluorescence of model compounds and lysozyme by iodide ion. Biochemistry 10(26), 4995 (1971).

[350] F. Teale and R. Badley. Depolarization of the intrinsic and extrinsic fluorescence of pepsinogen and pepsin. Biochemical Journal 116(3), 341 (1970).

[351] Y. Kubota, H. Nakamura, M. Morishita, and Y. Fujisaki. Interaction of 9-aminoacridine with 7-methylguanosine and 1, n6-ethenoadenosine monophosphate. Photochemistry and photobiology 27(4), 479 (1978).

[352] C. A. Seidel, A. Schulz, and M. H. Sauer. Nucleobase-specific quenching of fluorescent dyes-1 nucleobase one-electron redox potentials and their correlation with static and dynamic quenching efficiencies. The Journal of Physical Chemistry 100(13), 5541 (1996).

[353] Y. Kubota, Y. Motosa, Y. Shigemune, and Y. Fujisaki. Fluorescence quenching of 10-methylacrjdinium chloride by nucleotides. Photochemistry and Photobiology 29(6), 1099 (1979).

[354] J. R. Lakowicz and G. Weber. Quenching of fluorescence by oxygen. probe for structural fluctuations in macromolecules. Biochemistry 12(21), 4161 (1973).

[355] B. P. Joshi, J. Park, W. I. Lee, and K.-H. Lee. Ratiometric and turn-on monitoring for heavy and transition metal ions in aqueous solution with a fluorescent peptide sensor. Talanta 78(3), 903 (2009).

[356] A. Denicola, J. M. Souza, R. Radi, and E. Lissi. Nitric oxide diffusion in membranes determined by fluorescence quenching. Archives of biochemistry and biophysics 328(1), 208 (1996).

[357] S. Fischkoff and J. Vanderkooi. Oxygen diffusion in biological and artificial membranes determined by the fluorochrome pyrene. The Journal of general physiology 65(5), 663 (1975).

[358] R. Paul and H. Schneckenburger. Oxygen concentration and the oxidation-reduction state of yeast: Determination of free/bound nadh and flavins by time-resolved spectroscopy. Naturwissenschaften 83(1), 32 (1996).

[359] Andersson, Baechi, Hoechl, and Richter. Autofluorescence of living cells. Journal of Microscopy 191(1), 1 (1998).

[360] C. Fjeld, W. Birdsong, and R. Goodman. Differential binding of nad(+) and nadh allows the transcriptional corepressor carboxyl-terminal binding protein to serve as a metabolic sensor. Proceedings Of The National Academy Of Sciences Of The United States Of Ame 100(16), 9202 (2003).

[361] S. VERLICK. Fluorescence spectra and polarization of glyceraldehyde-3-phosphate and lactic dehydrogenase coenzyme complexes. The Journal of biological chemistry 233(6), 1455 (1958).

[362] M. R. Eftink. Fluorescence quenching: theory and applications. In Topics in fluorescence spectroscopy, pp. 53–126 (Springer, 2002).

[363] M. R. Eftink and C. A. Ghiron. Fluorescence quenching studies with proteins. Analytical biochemistry 114(2), 199 (1981).

[364] P. Belenky, K. L. Bogan, and C. Brenner. Nad+ metabolism in health and disease. Trends in biochemical sciences 32(1), 12 (2007).

[365] F. Berger, M. H. Ramirez-Hernandez, and M. Ziegler. The new life of a centenarian: signalling functions of NAD (P). Trends in biochemical sciences 29(3), 111 (2004).

[366] N. Pollak, C. Dolle, and M. Ziegler. The power to reduce: pyridine nucleotides-small molecules with a multitude of functions. Biochemical Journal 402(2), 205 (2007).

[367] J. Liang, W.-L. Wu, Z.-H. Liu, Y.-J. Mei, R.-X. Cai, and P. Shen. Study the oxidative injury of yeast cells by NADH autofluorescence. Spectrochimica Acta Part A: Molecular and Biomolecular Spectroscopy 67(2), 355 (2007).

[368] F. Bartolome and A. Y. Abramov. Measurement of mitochondrial NADH and FAD autofluorescence in live cells. Mitochondrial Medicine: Volume I, Probing Mitochondrial Function pp. 263–270 (2015).

[369] T. S. Blacker, Z. F. Mann, J. E. Gale, M. Ziegler, A. J. Bain, G. Szabadkai, and M. R. Duchen. Separating NADH and NADPH fluorescence in live cells and tissues using FLIM. Nature communications 5 (2014).

[370] P. Held. Determination of NADH concentrations with the Synergy 2 Multi-Detection Microplate Reader using fluorescence or absorbance: Do you know what your redox state is? Application Note pp. 1–6 (2007).

[371] J. Eng, R. M. Lynch, and R. S. Balaban. Nicotinamide adenine dinucleotide fluorescence spectroscopy and imaging of isolated cardiac myocytes. Biophysical Journal 55(4), 621 (1989).

[372] J. R. Lakowicz, H. Szmacinski, K. Nowaczyk, and M. L. Johnson. Fluorescence lifetime imaging of free and protein-bound NADH. Proceedings of the National Academy of Sciences 89(4), 1271 (1992).

[373] S. R. Piersma, A. J. Visser, S. de Vries, and J. A. Duine. Optical spectroscopy of nicotinoprotein alcohol dehydrogenase from Amycolatopsis methanolica: a comparison with horse liver alcohol dehydrogenase and UDP-galactose epimerase. Biochemistry 37(9), 3068 (1998).

[374] R. Chen. Quenching of the fluorescence of proteins by silver nitrate. Archives of Biochemistry and Biophysics 158(2), 605 (1973).

[375] S. Madhuri, N. Vengadesan, P. Aruna, D. Koteeswaran, P. Venkatesan, and S. Ganesan. Native fluorescence spectroscopy of blood plasma in the characterization of oral malignancy. Photochemistry and Photobiology 78(2), 197 (2003).

[376] G. M. Palmer, P. J. Keely, T. M. Breslin, and N. Ramanujam. Autofluorescence spectroscopy of normal and malignant human breast cell lines. Photochemistry and Photobiology 78(5), 462 (2003).

[377] B.-H. Li and S.-S. Xie. Autofluorescence excitation-emission matrices for diagnosis of colonic cancer. World journal of gastroenterology: WJG 11(25), 3931 (2005).

[378] M. Van de Weert and L. Stella. Fluorescence quenching and ligand binding: a critical discussion of a popular methodology. Journal of Molecular Structure 998(1), 144 (2011).

[379] A. S. Galkin, V. G. Grivennikova, and A. D. Vinogradov. → H+/2e stoichiometry in NADH-quinone reductase reactions catalyzed by bovine heart submitochondrial particles. FEBS letters 451(2), 157 (1999).

[380] P. G. Cordeiro, R. E. Kirschner, Q.-Y. Hu, J. J. Chiao, H. Savage, R. R. Alfano, L. A. Hoffman, and D. A. Hidalgo. Ultraviolet excitation fluorescence spectroscopy: a noninvasive method for the measurement of redox changes in ischemic myocutaneous flaps. Plastic and reconstructive surgery 96(3), 673 (1995).

[381] A. Mayevsky and G. G. Rogatsky. Mitochondrial function in vivo evaluated by NADH fluorescence: from animal models to human studies. American journal of physiology-Cell physiology 292(2), C615 (2007).

[382] S. D. Campbell, D. P. Tremblay, F. Daver, and D. Cousins. Wavelength comparison study for bioaerosol detection. In Proc. of SPIE Vol, vol. 5778, p. 131 (2005).

[383] W. Chen, P. Westerhoff, J. A. Leenheer, and K. Booksh. Fluorescence excitation-emission matrix regional integration to quantify spectra for dissolved organic matter. Environmental science & technology 37(24), 5701 (2003).

[384] R. S. DaCosta, H. Andersson, and B. C. Wilson. Molecular fluorescence excitationâĂŞemission matrices relevant to tissue spectroscopy. Photochemistry and photobiology 78(4), 384 (2003).

[385] P. Datta and D. Bhattacharyya. Analysis of fluorescence excitation-emission matrix of multicomponent drugs: A case study with human placental extract used as wound healer. Journal of pharmaceutical and biomedical analysis 36(1), 211 (2004).

[386] M. R. Duchen. Contributions of mitochondria to animal physiology: from homeostatic sensor to calcium signalling and cell death. The Journal of physiology 516(1), 1 (1999).

[387] M. E. Gosnell. Unlocking the Potential of Spectral Imaging for the Characterisation of Cell and Stem Cell Populations. Ph.D. thesis, Macquarie University, Faculty of Science, Department of Physics and Astronomy (2014).

[388] D. G. Nicholls and S. L. Budd. Mitochondria and neuronal survival. Physiological reviews 80(1), 315 (2000).

[389] W. Y. Kao, C. E. Davis, Y. I. Kim, and J. M. Beach. Fluorescence emission spectral shift measurements of membrane potential in single cells. Biophysical journal 81(2), 1163 (2001).

[390] K. K. Millis, K. H. Weaver, and D. L. Rabenstein. Oxidation/reduction potential of glutathione. The Journal of Organic Chemistry 58(15), 4144 (1993).

[391] G. T. Hanson, R. Aggeler, D. Oglesbee, M. Cannon, R. A. Capaldi, R. Y. Tsien, and S. J. Remington. Investigating mitochondrial redox potential with redox-sensitive green fluorescent protein indicators. Journal of Biological Chemistry 279(13), 13044 (2004).

[392] K. M. Heiskanen, M. B. Bhat, H.-W. Wang, J. Ma, and A.-L. Nieminen. Mitochondrial depolarization accompanies cytochrome crelease during apoptosis in pc6 cells. Journal of Biological Chemistry 274(9), 5654 (1999).

[393] V. L. Shapovalov, E. A. Kotova, T. I. Rokitskaya, and Y. N. Antonenko. Effect of gramicidin A on the dipole potential of phospholipid membranes. Biophysical journal 77(1), 299 (1999).

[394] K. Drozdowicz-Tomsia, A. G. Anwer, M. A. Cahill, K. N. Madlum, A. M. Maki, M. S. Baker, and E. M. Goldys. Multiphoton fluorescence lifetime imaging microscopy reveals free-to-bound NADH ratio changes associated with metabolic inhibition. Journal of biomedical optics 19(8), 086016 (2014).

[395] W. Pendergrass, N. Wolf, and M. Poot. Efficacy of mitotracker green and cmxrosamine to measure changes in mitochondrial membrane potentials in living cells and tissues. Cytometry Part A 61(2), 162 (2004).

[396] E. A. Mazzio and K. F. Soliman. Cytoprotection of pyruvic acid and reduced β-nicotinamide adenine dinucleotide against hydrogen peroxide toxicity in neuroblastoma cells. Neurochemical research 28(5), 733 (2003).

[397] E. McGuinness and J. Butler. Nad+ kinase-a review. International Journal of Biochemistry 17(1), 1 (1985).

Appendix of this thesis has been removed as it may contain sensitive/confidential content